Kebali Farida
M'sila University,
Algeria

ICCPMS2019

International Conference on Chemical Physics and Materials Science

8-10 July 2019
Istanbul, Turkey

E-mail : iccpms2019@europenanoscience.org
Web : www.materials-conference.com

ABSTRACT ID: 046

Certificate of Participation

This is to certify that **Kebaili Farida** of the M'sila University, Algeria attended and presented a poster entitled "Modelling and Simulation of the Carbon Nanotubes FETs" in the **International Conference on Chemical Physics and Materials Science (ICCPMS2019),** held at Ramada Encore Airport Hotel, Istanbul, Turkey during 8-10 July 2019.

We would like to thank you for your participation and for contributing to the success of ICCPMS2019.

Saim Emin, Ph.D.
President
EUROPEAN NANOSCIENCE AND NANOTECHNOLOGY ASSOCIATION (ENNA)

ORGANIZER:
European Nanoscience and Nanotechnology Association in cooperation with the Ankara Yıldırım Beyazıt University, Turkey.

ENNA

ICCPMS2019

INTERNATIONAL CONFERENCE ON CHEMICAL PHYSICS AND MATERIALS SCIENCE

Conference Proceedings

8-10 July 2019, Istanbul, Turkey

INTERNATIONAL CONFERENCE ON CHEMICAL PHYSICS AND MATERIALS SCIENCE

8-10 July 2019, Istanbul, Turkey

Conference Proceedings

Conference Venue:

Ramada Encore Istanbul Airport Hotel ****
Beşyol Mahallesi, Birlik Cd. No:10, 34295 Küçükçekmece/İstanbul, Turkey

Editors: Saim Emin
Abdullah Yildiz
Polina Mladenova

Publisher: European Nanoscience and Nanotechnology Association
Sofia, 2019
ISSN 2682-9789

Program Committee

Executive Chairs

Saim Emin
European Nanoscience and Nanotechnology Association, Bulgaria; Assistant Professor, University of Nova Gorica, Slovenia

Abdullah Yildiz
Ankara Yıldırım Beyazıt University, Turkey

Organizing/Scientific Committee

Turan Ozturk, Istanbul Technical University, Istanbul, Turkey

Saim Emin, University of Nova Gorica, Slovenia

Yasemin Ciftci, Gazi University, Ankara, Turkey

Abdullah Yildiz, Ankara Yıldırım Beyazıt University, Turkey

Scientific Advisory Board Members

Amitava Patra, Indian Association for the Cultivation of Science, Kolkata, India

Antonella Parisini, University of Parma, Italy

Azzedine Bendounan, Synchroton SOLEIL, L'Orme des Marisiers, France

Bilge Baytekin, Bilkent University, Turkey

Ding Jun, National University of Singapore, Singapore

Ganesh Datt Sharma, The LNM Institute of Information Technology (Deemed University), Jaipur, India

Go Yamamoto, Tohoku University, Japan

Hideo Miura, Tohoku University, Japan

Hongwei Zhu, Tsinghua University, Beijing, China

Issa M. El Nahhal, Al-Azhar University, Palestine

Keon Jae Lee, Korea Advanced Institute of Science & Technology, South Korea

Lorenzo Malavasi, University of Pavia, Italy

Matjaz Valant, University of Nova Gorica, Slovenia

Mohd Hafiz Dzarfan Othman, Advanced Membrane Technology Research Centre (AMTEC), Malaysia

Mukhlis A. Rahman, Universiti Teknologi Malaysia, Malaysia

Sahrim Ahmad, Universiti Kebangsaan Malaysia, Malaysia

Prakash A. Mahanwar, Institute of Chemical Technology, India

Said Rechak, Ecole Nationale Polytechnique, Algiers

Sebahattin Tuzemen, Ataturk University, Turkey

Selcuk Yerci, Middle East Technical University, Turkey

Tolou Shokuhfar, University of Illinois at Chicago, USA

Turan Öztürk, Istanbul Technical University, Turkey

Reza Shahbazian-Yassar, University of Illinois at Chicago, USA

Waltraud Kriven, University of Illinois at Urbana -Champaign, Urbana, USA

Xiaosheng Fang, Fudan University, China

Yasemin Ciftci, Gazi University, Turkey

Zeki Candan, Istanbul University, Turkey

Junqian Zhang, Shanghai University, China

CONTENTS

Prediction of tensile strength of unidirectional carbon fiber-reinforced plastic composites

Authors: G. Yamamoto[1*], K. Koizumi[1], T. Okabe[1,2]

Affiliations:
[1]*Department of Aerospace Engineering, Tohoku University, 6-6-01 Aramaki-Aza-Aoba, Aoba-ku, Sendai 980-8579, Japan.*
[2]*Department of Materials Science and Engineering, University of Washington, Seattle, WA 98195, U.S.A.*

*Corresponding author: yamamoto@plum.mech.tohoku.ac.jp

One Sentence Summary: A result obtained from multi-fiber fragmentation tests in combination with a spring element model simulation demonstrate that, even if the mechanical properties of matrix polymer materials vary, the proposed method can yield a reasonable prediction of the tensile strength of unidirectional carbon fiber-reinforced plastic composites.

Abstract: The tensile strengths of unidirectional carbon fiber-reinforced plastics (CFRPs) were predicted by using a spring element model that considers the surface stress concentration on fibers caused by a fracture site in an adjacent fiber. The surface stress concentration on the fibers was experimentally evaluated by implementing multi-fiber fragmentation tests in conjunction with a spring element model (SEM) simulation. Four types of epoxy materials were utilized to explore the effects of matrix polymer properties on the surface stress concentration of the fibers. The size scaling results, coupled with the results of the SEM simulation, designed to take into account the surface stress concentration, were reasonably consistent with the experimental data on the tensile strengths of the unidirectional CFRP composites, regardless of the differences in the matrix mechanical properties. Possible mechanisms by which additional stress concentration is generated on an intact fiber surface were analyzed numerically using the finite element method.

Introduction

Engineering composite materials are attracting the attention of people within engineering sectors because of the unique mechanical properties and ease of property customization, thereby making them highly competitive with conventional materials. Carbon fiber reinforced plastic (CFRP), which is a typical class of composite materials, are increasingly being used as lightweight and high-stiffness materials in various applications. The process of determining the potential amount of weight that can be saved requires that the fracture properties of the CFRP in the direction of the fiber axis be a major consideration in the design of composite structures. Thus, improving the accuracy of tensile strength prediction methods continues to be central to CFRP composite research [1,2].

In this study, we considered the surface stress concentration on fibers caused by a fracture site in an adjacent fiber into our prediction of the ultimate tensile strengths of unidirectional CFRP composites. The stress concentrated on the fiber surface was determined by performing multi-fiber fragmentation tests in combination with a spring element model (SEM) simulation. We defined the coordinated fracture to quantitatively evaluate the stress concentration factors (SCFs). The acquired SCF was subsequently applied to obtain the tensile strength prediction of the unidirectional CFRP composite. The composites were fabricated with T1100G carbon fiber and four types of epoxy materials with different mechanical characteristics. We tested these composite materials to validate the proposed prediction method. The size scaling results obtained in conjunction with the results from the SEM simulation were reasonably consistent with the experimental data on the strengths of the four types of unidirectional CFRP composites used herein. A scenario on the origin of stress concentrations generated on an intact fiber surface is investigated through a numerical analysis based on the finite element method.

Results

Mechanical evaluation of unidirectional CFRP composites

Unidirectional CFRP composites consisting of the four types of matrix polymers were prepared, and subsequently employed tensile loading tests to investigate their mechanical properties along the direction of the fiber axis. Fig. 1 and Table 1 summarize the representative stress-strain behavior and summary of the measured mechanical properties, respectively. Note that no significant difference was observed between the Young's modulus values, whereas for example the composite fabricated with the D-epoxy demonstrated strength enhanced by a factor of approximately 1.2 compared to the composite made with the A-epoxy.

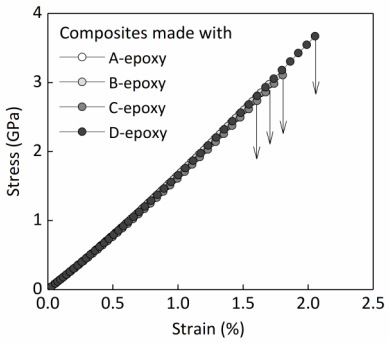

Fig. 1. Representative stress-strain curves for the four types of unidirectional CFRP composites.

Tensile strength prediction of B-epoxy matrix composites

Next, we investigated the influence of interfiber spacing on the failure phenomena of the fibers by performing a double -fiber fragmentation test. For this test, the B-epoxy material was used in the specimen preparation. A quantitative determination of the SCFs on the surface of an intact fiber near a fiber break point was achieved by implementing the SEM to investigate the

Table 1: Measured properties for the four types of unidirectional CFRP composites.

	Young's modulus (GPa)	Tensile strength (GPa)	Failure strain (%)
A-epoxy matrix composite	179 (178–180)	3.12 (2.95–3.22)	1.60 (1.51–1.65)
B-epoxy matrix composite	175 (169–179)	3.17 (3.05–3.32)	1.65 (1.59–1.74)
C-epoxy matrix composite	171 (166–175)	3.26 (3.08–3.35)	1.73 (1.67–1.83)
D-epoxy matrix composite	174 (172–177)	3.85 (3.74–3.97)	1.98 (1.93–2.01)

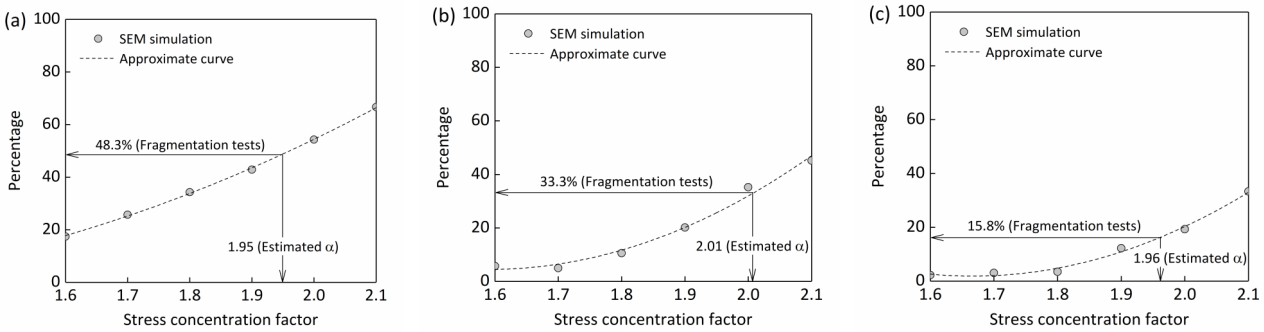

Fig. 2. Relationship between the SCFs and the percentage of coordinated fractures for the (a) double-, (b) triple-, and (c) quadruple-fiber fragmentation composites.

value of SCF. Fig. 2 illustrates the relationship between the SCF and the percentage of coordinated fractures for each fragmentation composite, which was determined by systematically sweeping SCF in the SEM simulation. The simulation results showed that the percentage of coordinated fractures increased in response to an increased SCF, but decreased with an increase in the number of fibers. Upon comparing the simulated percentages of coordinated fractures to the corresponding experimental observations, the SCF on the surface of an intact fiber was determined to be approximately 2.0. Moreover, the number of fibers did not significantly affect the surface SCF, indicating that for the composites fabricated with B-epoxy, the concentrated stress acting on the fiber surface was twice as much as the fiber stress with no additional surface stress concentration. Fig. 3 illustrates a comparison of the experimental and simulated results for the unidirectional T1100G carbon fiber/B-epoxy composites. In this figure, the circles represent the size scaled strength results calculated according to reference [3], whereas the cross symbols denote the experimentally obtained tensile strengths of these composites, which ranged from 3.05 to 3.32 GPa (mean: 3.17 GPa). The simulated data obtained without consideration of added concentrated stress were incongruent with the experimental data, whereas the predictions incorporating an SCF of 2.0 were reasonably consistent with the experimental data. Furthermore, although the prediction with SCF = 2.1 seemed to yield a better tensile strength prediction than with SCF = 2.0, we conclude that the prediction method proposed herein yields a reasonably accurate tensile strength prediction when the matrix crack-induced surface stress concentration of fibers is appropriately considered.

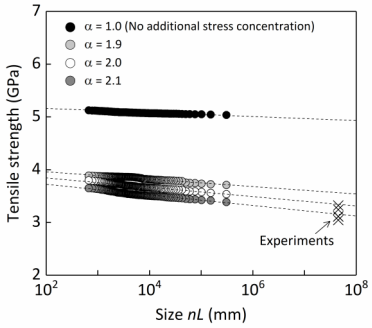

Fig. 3. Experimental and simulated results for the unidirectional T1100G/B-epoxy composites.

Application to different types of composites

We applied the above-mentioned strength prediction method to the unidirectional CFRP composites made with the "A-epoxy," "C-epoxy," and "D-epoxy." The SCF on the surface of intact fibers was acquired via double-fiber fragmentation testing considering the fact that for the B-epoxy matrix composites, the number of fibers did not influence the SCFs (Fig. 2). The SCFs were calculated as approximately 2.15 for the A-epoxy, 1.93 for the C-epoxy, and 1.75 for the D-epoxy. A comparison of the results presented in Fig. 2 revealed clear differences among them. Thus, surface SCFs were implemented to predict the tensile strength of the three types of the unidirectional CFRP composites. Fig. 4 presents a comparison of the experimental and simulated results. In one example, the experimentally obtained tensile strengths of the D-epoxy matrix composites ranged from 3.74 to 3.97 GPa (mean: 3.85 GPa), and are denoted by a cross symbol in the figure. The estimated tensile strength simulated under the condition of α=1.75 was approximately 3.9 GPa. This value is reasonably consistent with the experimentally obtained tensile strength. Consequently, the results demonstrate that, even if the mechanical properties of the matrix materials vary, the proposed method can yield a reasonable prediction of the tensile strength of the unidirectional CFRP composites.

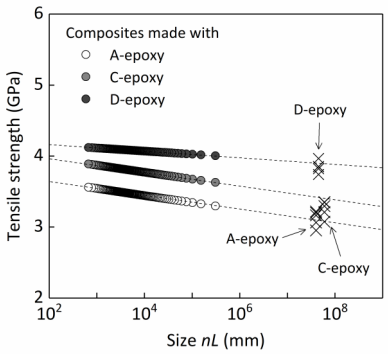

Fig. 4. Experimental and simulated results for the three types of unidirectional CFRP composites. The cross symbols indicate the experimentally obtained tensile strengths of these composites.

Discussion

The possible mechanism by which the additional stress concentration occurs is not clear; moreover is it unclear why the SCF varies depending on the matrix characteristics. A numerical analysis using the finite element method was conducted to access possible mechanisms by which higher stress is generated on the intact fiber surface adjacent to the fiber break point. In this analysis, a hexagonal fiber arrangement was used, and only one-twelfth of the structure was modeled and analyzed owing to reasons of structural symmetry. The fiber and matrix were assumed to be elasto-plastic and elastic materials, respectively. The matrix was assumed to have rehardening characteristics with a modulus of 0.38 GPa, which is 1/10 of the initial slope in the elastic region of the D-epoxy material. Moreover, the plasticity-free layer model of Suo, Shih, and Varias [4], referred to as the SSV model, an elastic layer with a thickness of 50 nm, was imposed around the matrix crack using the same elastic properties as the D-epoxy material. The matrix crack was assumed not to reach the intact fiber surface and there was a 30 nm-thick elastic layer between the crack tip and the intact fiber surface. Due to the elastic region surrounding the matrix crack, the stress singularity is retained. Displacement control is considered in the model, and the maximum applied composite strain is 2.0%. It was revealed that an SCF =~1.7, as observed for the D-epoxy matrix composite, was indeed generated on the intact fiber surface by defining the SCF as the ratio of the stress of an outermost surface element of the intact fiber to the stress in an element sufficiently away from the fiber break point. We consider that the above-mentioned mechanism is one of the scenarios in which a higher stress is generated on the intact fiber surface. It remains unclear why the SCF varies with the matrix characteristics, and further research is needed to clarify this reason; however, because the degree of SCF depends on the gap between the crack tip and the intact fiber surface, we speculate that the difference in the gap distance was caused by the difference in the mode-I stress intensity factor of the epoxy matrix.

In summary, four types of unidirectional CFRP composites with different mechanical characteristics were prepared in this study. The tensile strengths of the fabricated composites were predicted via a numerical simulation based on the results obtained from multi-fiber fragmentation experiments. Furthermore, the primary aim of this study was to explore the effects of matrix polymer properties on the stress concentrated on the fiber surface. Consequently, the multi-

fiber fragmentation test results demonstrated that for an interfiber spacing of one-half to four fiber diameters, the failure process of the fiber was predominantly governed by fiber-fiber interactions, irrespective of the matrix polymer properties. We also demonstrated that the degree of stress concentrated on the surface of fibers can be changed by modifying the mechanical properties of the matrix polymer. Additionally, utilizing an epoxy matrix with a higher Young's modulus and increased tensile strength in the composite preparation reduced the SCF from approximately 2.15 to 1.75. We have also shown a numerical scenario on the origin of the stress concentrations that are generated on the intact fiber surface by implementing the SSV model and employing the rehardening characteristics of epoxy materials. Finally, we confirmed that employing the measured SCFs and bimodal Weibull distribution to determine how strength is statistically distributed throughout the fiber yields the predicted strengths of the four types of unidirectional CFRP composites that are reasonably consistent with the experimental data, thereby demonstrating the validity of the proposed prediction method.

Materials and Methods

Sample preparation and mechanical characterization

High-strength, polyacrylonitrile (PAN)-based carbon fiber (TORAYCA^{TM} T1100G) and four types of bisphenol-A epoxy resin materials were used to prepare multi-fiber and UD composites. Table 1 presents a summary of the physical and mechanical properties of the fiber and the matrix. Note that the tensile-loading experiments performed herein revealed that the four types of epoxy materials exhibited different mechanical characteristics. Thus, the epoxy materials are hereafter referred to as "A-epoxy," "B-epoxy," "C-epoxy," and "D-epoxy," with the order of the names indicating the magnitude of the elastic modulus (lowest to highest).

Multi-fiber fragmentation tests were performed to facilitate the derivation of a quantitative description of fiber failure processes by using a polarized-light microscope equipped with a custom-made four-point bending machine. Further details of the composite preparation and testing procedures are described elsewhere [2]. The strain was increased in 0.1% steps until a maximum of 5.0% tensile strain was achieved and held constant during the observation of both the number and positions of the broken fibers. The number of broken fibers observed under the pure bending conditions, was counted using the polarized-light microscope.

The tensile strengths of the prepared unidirectional CFRP composites were measured to validate the accuracy of the tensile strength predicted by a spring element model derived based on the multi-fiber fragmentation test results. The composites were prepared via conventional vacuum bagging and autoclave laminating technique to produce the laminate structure of $[0_6]$. The details of composite preparation procedures and mechanical evaluation can be found in the reference [2].Five samples for the four types of unidirectional CFRP composites were measured.

Model preparation and determination of stress concentration factor

Monte-Carlo methods were implemented in the SEM simulation to determine the stress concentrated on the surface of the intact fibers surrounding the fiber break points. The spring element model comprises longitudinal and transverse spring elements in a three dimensional hexagonal arrangement [1,5]. Further details of the model preparation and determination of stress concentration factor are described elsewhere [2]. The SCFs on the surface of an intact fiber were determined by employing the SEM model to investigate the SCF value, with the aim of ensuring that it was equivalent to the percentage of the coordinated fracture, which is defined as a failure occurring at the elements neighboring a broken element in the horizontal plane of the broken fiber element, that was determined via multi-fiber fiber fragmentation testing. Thus, the two to four longitudinal spring elements in the center of the SEM were assigned to the fibers, and the remaining elements were assigned to the matrix.

References and Notes:

J. Watanabe, F. Tanaka, R. Higuchi, H. Matsutani, H. Okuda, T. Okabe, A study of stress concentrations around fiber breaks in unidirectional CF/epoxy composites using double-fiber fragmentation tests. *Adv. Compos. Mater.* **27**, 575–587 (2018).

G. Yamamoto, M. Onodera, K. Koizumi, J. Watanabe, H. Okuda, F. Tanaka, T. Okabe, Considering the stress concentration of fiber surfaces in the prediction of the tensile strength of unidirectional carbon fiber-reinforced plastic composites. *Compos. Pt. A Appl. Sci. Manuf.* **121**, 499–509 (2019).

T. Okabe, N. Takeda, Size effect on tensile strength of unidirectional CFRP composites experiment and simulation. *Compos. Sci. Technol.* **62**, 2053–2064 (2002).

Z. Suo, C.F. Shih, A.G. Varias, A theory for cleavage cracking in the presence of plastic flow. *Acta. Mater.* **41**, 1551–1557 (1993).

T. Okabe, H. Sekine, K. Ishii, M. Nishikawa, N. Takeda, Numerical method for failure simulation of unidirectional fiber-reinforced composites with spring element model. *Compos. Sci. Technol.* **65**, 921–933 (2005).

Acknowledgments: The authors thank Mr. W. Shoichiro of the Department of Aerospace Engineering, Tohoku University, and Dr. R. Higuchi of the Department of Aeronautics and Astronautics, The University of Tokyo, for technical assistance in the FEM analysis. This work was partly supported by Toray Industries, Inc., Japan, the Council for Science, Technology and Innovation (CSTI), Japan, the Cross-ministerial Strategic Innovation Promotion Program (SIP), Japan, and JSPS KAKENHI grant number 18K04721. The authors would like to thank the reviewers for their useful comments and recommendations. The authors would like to acknowledge the vitally important encouragement and support made through the University of Washington-Tohoku University: Academic Open Space (UW-TU: AOS).

Synthesis and Electronic Properties of Thienothiophene and Dithienothiophene Based Organic Materials

Autor: T. Ozturk[1,2*]

Affiliations:
[1]*Istanbul Technical University, Science Faculty, Chemistry Department, 34469 Maslak Istanbul Turkey,*
[2]*Tubitak UME, Chemistry Laboratories, Gebze Kocaeli, Turkey*

*Corresponding author: ozturktur@itu.edu.tr; www.turanozturk.com

Syntheses of various thienothiophene and dithienothiophene based organic materials and their electronic and optoelectronic properties are reported.

Abstract: Thienothiophenes (TT) dithienothiophenes (DTT) are important building blocks of various organic materials, including solar cells, OLEDs, transistors, energy storage, electrochromic devices and sensors. This is mainly due to their electron rich character. In this study, TTs and DTTs, having alkyl and aryl substituents were synthesized and their electronic and opto-electronic properties were investigated.

Introduction

Thienothiophenes (TT) **1**[1-3] are the simplest fused two thiophenes, and dithienothiophenes (DTT) **2**[2-4] are the molecules with three fused thiophenes. While TTs have four isomers, DTTs have six isomers depending upon the orientation of sulfur atoms. TTs and DTTs, particularly the analogues thieno[3,2-*b*]thiophene **1** and dithieno[3,2-*b*;2′,3′-*d*]thiophene **2**, are the interest of organic material chemists. This is due to their better conjugation compare with their analogues.

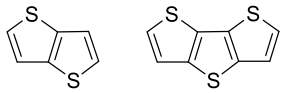

1 **2**

Various synthetic methods have been developed and their applications in organic electronic and opto-electronic have been investigated.[1] The present synthetic methodologies available in the literature include four steps. On the other hand, the TTs **3** and DTTs **4** presented in this study were synthesized in two steps developed by our group. It includes synthesis of mono and diketones and then ring closure reactions to obtain the corresponding TTs **3** and DTTs **4**, respectively.

As those DTTs and TTs are useful compounds in organic material chemistry, various organic materials, including small molecules and polymers, were prepared for solar cell, OLED, capacitor and electrochemical devices as well as sensitizer for ATRP polymerization.

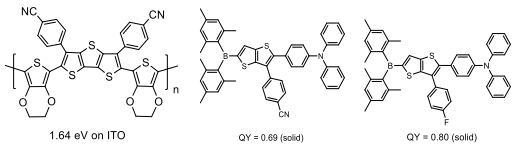

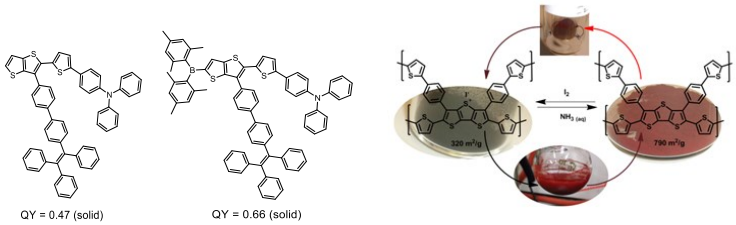

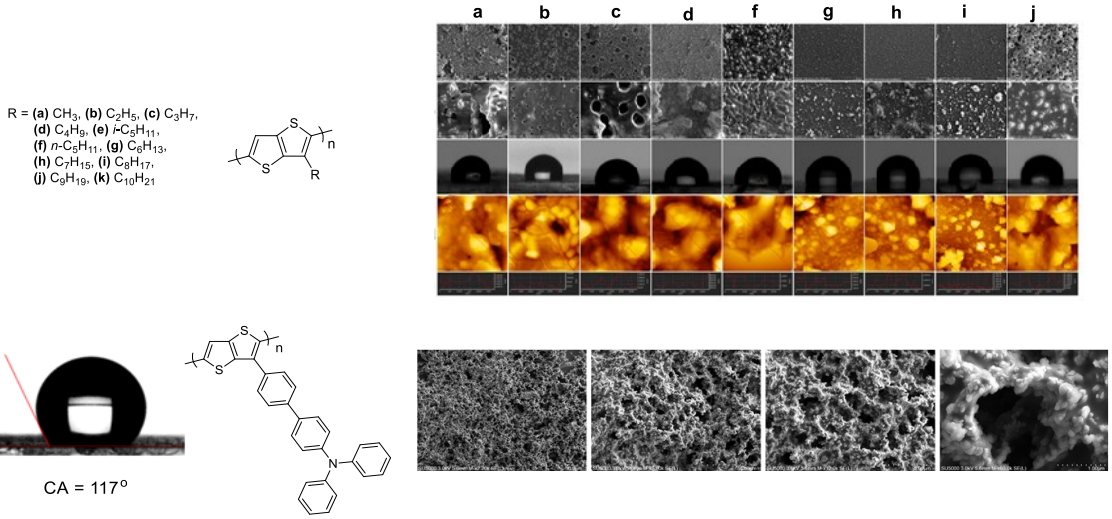

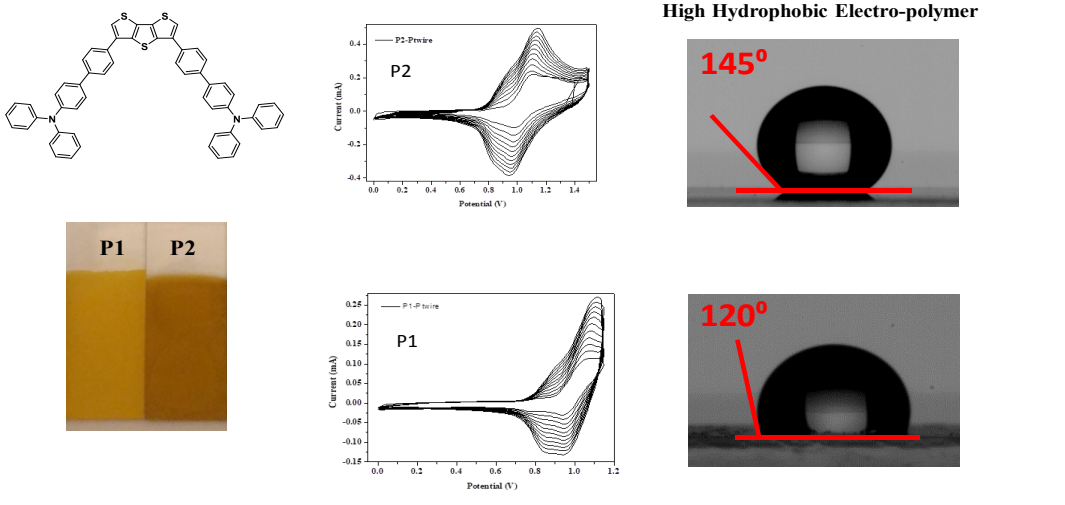

References

1) (a) M. E. Cinar, T. Ozturk, Thienothiophenes, dithienothiophenes, and thienoacenes: syntheses, oligomers, polymers, and properties. *Chem. Rev.,* **115**, 3036-3140 (2015), (b) Z. Xiao, J. Subbiah, K. Sun, D. J. Jones, A. B. Holmes, W. W. H. Wong, Synthesis and photovoltaic properties of thieno[3,2-*b*]thiophenyl substituted benzo[1,2-*b*:4,5-*b*′]dithiophene copolymers. *Polym. Chem*., **5**, 6710-6717 (2014). (c) X. Wang, Z. -G. Zhang, H. Luo, S. Chen, S. Yu, H. Wang, X. Li, G. Yu, Y. Li, Effects of fluorination on the properties of thieno[3,2-*b*]thiophene-bridged donor–π–acceptor polymer semiconductors. *Polym. Chem*. **5**, 502-511 (2014). (d) L. Y. Lı. Chen, Y. Chen, C. Li, P. Zhang, L. Gao, X. Yang, Y. Tu, X. Zhu, Conjugated moiety effect on blend film phase separation and photovoltaic properties of benzo[1,2-*b*:4,5-*b*′]dithiophene-containing coplanar donor–acceptor copolymers. *Sol. Energ. Mat. Sol. C.* **108**, 136-145 (2013). (e) X. Guo, M. Zhang, L. Huo, F. Xu, Y. Wu, J. Hou, Design, synthesis and photovoltaic properties of a new D–π–A polymer with extended π-bridge units. *J. Mater. Chem*. **22**, 21024-21031 (2012). (f) W. Tang, L. Ke, L. Tan, T. Lin, T. Kietzke, Z. Chen, Conjugated Copolymers Based on Fluorene−Thieno[3,2-*b*]thiophene for Light-Emitting Diodes and Photovoltaic Cells. *Macromolecules*, **40**, 6164-6171 (2007). (g) M. He, F. Zhang, *J. Org. Chem*. **72**, 442 (2007). (h) X. Zhang, M. Köhler, A. Matzger, Alkyl-Substituted Thieno[3,2 -*b*]thiophene Polymers and Their Dimeric Subunits. *Macromolecules*, **37**, 6306-6315 (2004).
2) F. Dikcal, T. Ozturk, M. E. Cinar, Fused thiophenes: an overview of the computational investigations. *Org. Commun.* **10**, 56-71 (2017).
3) M. E. Cinar, T. Ozturk, Ed. John Joule, Thiophenes, Springer, "*Top. Heterocycl. Chem*." **39**, 161 (2015).
4) T. Ozturk, E. Ertas, O. Mert, Dithienothiophenes. *Tetrahedron*, **61**, 11055-11077 (2005)

Surface Physics of Thin Film Oxide Semiconductors on the bases of Gas Sensing Properties

Autors: S. Tüzemen[a*], Ö. Çoban[b]

Affiliations:
[a]*Department of Physics, Faculty of Science, Atatürk University, 25240 Yakutiye-Erzurum, Turkey*
[b]*Department of Electricity, Ispir Hamza Polat Vocational High School, Ispir-Erzurum,Turkey*

**Corresponding author: stuzemen@atauni.edu.tr*

One Sentence Summary: Surface properties of some thin film oxide semiconductors have been investigated in terms of the gas sensing mechanisms under hydrogen exposition.

Abstract: Surface properties of the thin film oxide semiconductors are of great importance in terms of the gas sensing mechanisms in the devices consisted of these materials. Optical gas sensors based on the thin films of the NiO and WO_3 oxide semiconductors exhibit rather advantageous properties in comparison to the previously used fiber optic coating. It has been shown that the adsorption and desorption under hydrogen exposure depend on the type of the material. We have introduced possible models for the physical mechanisms that exhibit an increase in n-type and a decrease in p-type materials for the absorbance. A nano-layer metal sensitizing of Pd and Pt up to 340% on the thin film surfaces of the various oxide samples of NiO and WO_3 have also been observed in the range of 450 nm-850 nm wavelengths, covering the VIS-IR range. Present applications of the obtained devices on the hydrogen sensing up to low concentrations of 200 ppm, with relatively low response times around 70 s and that of recovery around 200 s.

Introduction

A gasochromic effect in semiconductor thin films or coatings is a phenomenon that construct an increase or decrease in absorbance of the material under a gas exposure taking place in a certain wavelength range especially in visible-IR region. This particular event happens especially in oxides where oxidation and anti-oxidation can manipulate the surface properties, resulting in a change in the optical absorbance of the surfaces. The phenomena can be used in devices such as gas sensors and solar harvesters that especially involve oxide layers facing the incident radiation. Here, we focus on the gas sensing features of the event since we detect very high optical responses of the materials NiO and WO_3.

Wide range of gas sensing applications from environmental to medical sciences have led to the development of sensing materials (*1*) and appropriate sensing techniques (*2*) and have caused a lot of study to be done recently. Among the detection materials, the most popular are metal oxides and have been extensively studied to determine more than 150 types of gases (*3*). Accordingly, various gas sensors are based on different operating principles, such as conductometric gas sensors (*4*), optical gas sensors (*5*), micro-cantilever sensors (*6*), surface plasmon resonance sensors (*7*), catalytic combustion sensors (*8*), surface acoustic sensors (*9*), microwave sensors (*10*) have been reported and the most common ones are conductometric gas sensors.

However the optical gas sensors have various advantages in terms of high resistance, being unaffected by electrical or magnetic noise, safety and less danger against ignition and explosion without current pass or electrical contact. Conventional and commercially available optical sensors are Fiber Optic Sensors while it is also possible to come across thin-film optical sensors based on oxide semiconductor with different designs and higher sensitivity.

Hydrogen sensing has gained much importance especially after the development of the engines combusting hydrogen fuel in the automotive industry, since it especially becomes highly explosive if reached certain level of limit which is about 4% in volume. In this study, we demonstrate that gasochromic effects in some commonly used metal oxides can be used in hydrogen gas detection. We investigate the surface physics of materials before, during and after oxygen adsorption and desorption under H_2 gas exposure, depending on the conductivity type of the semiconducting oxides.

Results

The optical responses under the hydrogen gas exposure result in different responses in n and p-type materials. We basically share the two kinds of typical results that show that the absorbance decrease in p-type and increase in n-type materials as shown in Fig. 1.

These situations are very much related to the predictions invoked in the following surface physics and discussion section. In n-type material O adsorption occur in air and therefore H_2 exposure renders an increase in absorbance, while in p-type there would not be any O adsorption beforehand and H_2 exposure renders a decrease in absorbance.

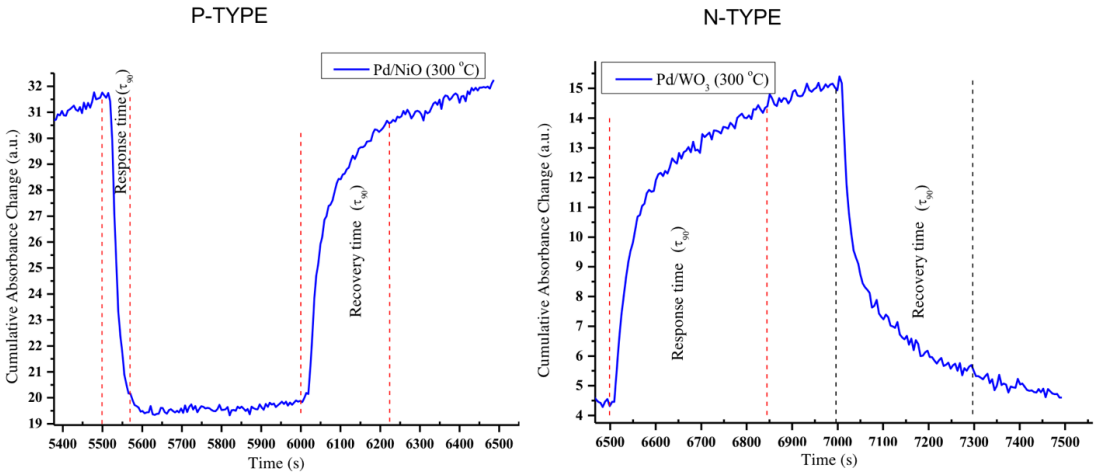

Fig. 1. The absorbance responses in p-type and n-type under H_2 gas ambient.

Discussion

In order to produce a reliable gas sensing material, we should discuss and understand the surface physics of oxides (*11*) and the reactions between the solid surface and the gas molecules. Developing a very sensitive gas detection technique is also associated with these reactions. The following conditions affect the interaction between the oxide surface and the gas ambient.

Adsorption or desorption of an incident gas depend on the type of the oxide material.

Surface energy of a certain material meaning that the surface atoms and molecules have more energy than in bulk define the chemical potentials of the certain gases exposed to the surface.

Surface energy is basically defined by the cutting work per unit area as follows;

$\gamma = W/2A$

Therefore the cleaved edges have low surface energy since the work is very low to produce these surfaces.

However the oxides have high surface energies due to the volatile oxygen component.

Therefore the surface energy of oxides depends on the surface morphology and orientation, which is defined by the final finish of the surface whether it has the O-component, or not.

In general, the oxides are crystallized in two different forms: First is the cubic structured as octahedral with six nearest neighbors and the latter is the hexagonal structured as tetrahedral with four nearest neighbors as described in Ref. (*11*). Therefore the final finish of the surface morphology will be very much dependent on the orientation defining the stoichiometry of the surface. Consequently the final formation of the surface defines the followings:

Surface defects (especially O-vacancies)

Surface charge state (neutral, positive or negative)

Surface dipole moment (zero or not)

Surface defects can also affect the interaction between sensing material and gas molecules. High concentrations of the O-vacancies mean high surface energy per unit area A. This will result in high O chemical potential (*2*). This is especially true for the surfaces having high concentrations of O-vacancies. Therefore the followings can be discussed;

Missing atoms (Oxygen Vacancies) emerge higher surface energy.

Surfaces dominated with Volatile Oxygen component have higher surface energy

Having high numbers of O-Vacancies results in high oxygen chemical potential and therefore O-adsorption.

Following this argument, in n-type material there would be band bending in air due to O-adsorption as shown in Fig.2 (a). As can be seen, before and after H_2 adsorption there would be an overall increase in the absorbance. On the other hand, in p-type material, there is no band bending in air due to O-desorption. This would cause a decrease in the absorbance as shown in Fig.2 (b).

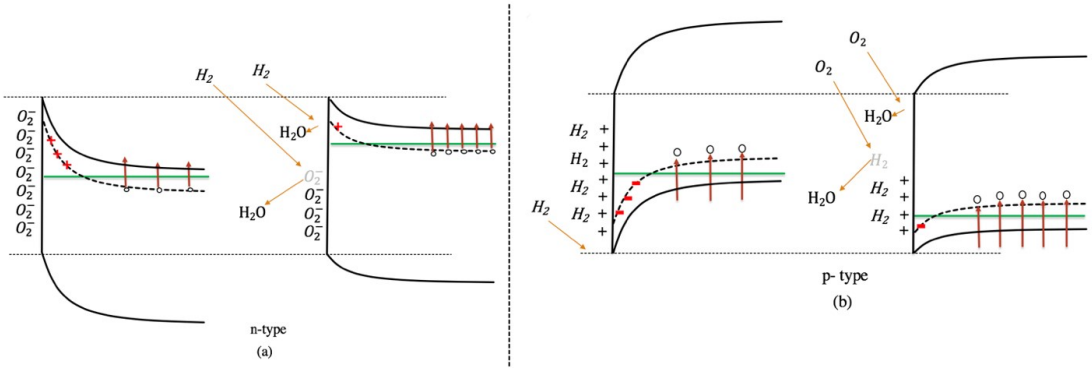

Fig. 2. Energy band diagrams under H_2 ambient (a) n-type, (b) p-type

Materials and Methods

NiO and WO_3 thin film sensing materials were grown onto the glass substrates by RF magnetron sputtering method. For the growth of NiO material, the background pressures (10^{-7} Torr), the growth pressure, the substrate temperature, the argon and oxygen flow rates and the power were respectively kept at $9.6x10^{-7}$ Torr, 27.8 mTorr, 250 ^oC, 300 sccm, 50 sccm and 100 W. For the growth of WO_3 material the background pressures, the growth pressure, the substrate temperature, the argon and oxygen flow rates and power were respectively set to $9.3x10^{-7}$ Torr, 26.5 mTorr, 300 ^oC, 250 sccm, 75 sccm and 100 W. Ni and W targets were used, having 99.995% purity, 2 inches diameters and thicknesses of 0.125 inch. Before deposition, Ni and W targets were pre-sputtered for 5 min in pure argon, then 5 min in the argon-oxygen mixture to clean the surfaces of the target for each sensing material. The distance between the target and the substrate was approximately 5 cm. The quartz thickness monitor was used to measure the thickness of the samples, which were 100 nm. After sensing material fabrication, sensors were coated with 5 nm Pd by the same technique.

H_2 sensing tests were performed in a home-built setup using the sensing devices made of NiO and WO_3 materials. Linkam HFS600E-PB4 heating/freezing (tuneable−195◦C and 600◦C) stage with four electrical characterization probe and the optical window used as a gas sensor test system. The stage can be set to different temperatures for hydrogen sensing application. To obtain different H_2 concentration level in air, the two Alicat Mass Flow Controllers were used, which were running in different flow levels of 0–0.5 sccm and 0–500 sccm,. The whole optical absorbance characterizations of the sensors under different hydrogen level were measured with the Sm242 Spectralproducts spectrometer and all devices controlled by the lab-view program. A schematic diagram of the sensor test system is shown in Fig. 3.

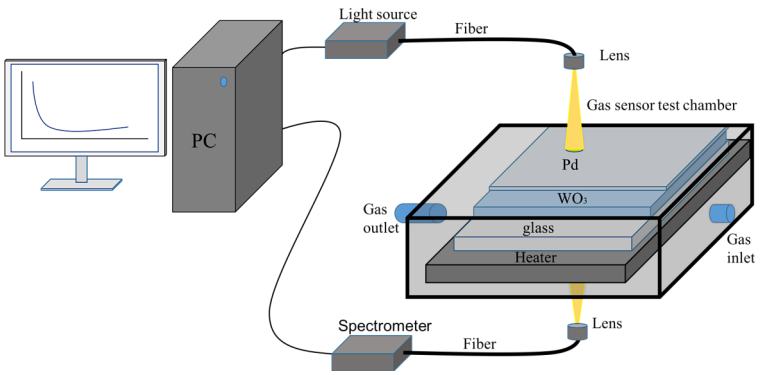

Fig. 3. Block diagram of the gas sensor test system block diagram

References:

1. A. Dey, Semiconductor metal oxide gas sensors: A review, Materials Science & Engineering B 229 (2018) 206–217
2. A. Mirzaei, S. Sub Kim, H. Woo Kim, Resistance-based H2S gas sensors using metal oxide nanostructures: A review of recent advances Journal of Hazardous Materials 357 (2018) 314–331
3. A. Mirzaei, S. Park, G.J. Sun, H. Kheel, C. Lee, CO gas sensing properties of In4Sn3O12 and TeO2 composite nanoparticle sensors, J. Hazard. Mater. 305 (2016) 130–138.
4. A. Mirzaei, G. Neri, Microwave-assisted synthesis of metal oxide nanostructures for gas sensing application: a review, Sens. Actuators B Chem. 237 (2016) 749–775.
5. J. Hodgkinson, R.P. Tatam, Optical gas sensing: a review, Meas. Sci. Technol. 24 (2012) 012004.
6. M. Sepaniak, P. Datskos, N. Lavrik, C. Tipple, Peer reviewed: microcantilever transducers: a new approach in sensor technology, Anal. Chem. A 74 (2002) 568.
7. J. Homola, S.S. Yee, G. Gauglitz, Surface plasmon resonance sensors: review, Sens. Actuators B Chem. 54 (1999) 3 –15.
8. A.M. Azad, S.A. Akbar, S.G. Mhaisalkar, L.D. Birkefeld, K.S. Goto, Solid-state gas sensors: a review, J. Electrochem. Soc. 139 (1992) 3690–3704.
9. K. Länge, B.E. Rapp, M. Rapp, Surface acoustic wave biosensors: a review, Anal. Bioanal. Chem. 391 (2008) 1509 –1519.
10. G. Barochi, J. Rossignol, M. Bouvet, Development of microwave gas sensors, Sens. Actuators B Chem. 157 (2) (2011) 374–379.
11. Tasker P. W. J. Phys. C: Solid State Phys. 12 4977 (1979)

Synthesis, Characterization and Catalytic Activity of 3-methyl-*N*-((3,3,5-trimethyl-5-((3-(3-methylbenzoyl)thioureido)methyl)cyclohexyl)carbamothioyl)benzamide (3-MBTU)

Autors: M. S. M. Yusof[1*], S. M. T. Mansor[1], M. A. Kadir[1], S. K. C. Soh[2]

Affiliations:

[1]*School of Fundamental Science, Universiti Malaysia Terengganu, 21030 Kuala Nerus, Terengganu, Malaysia*
[2]*School of Marine and Enviromental Sciences, Universiti Malaysia Terengganu, 21030 Kuala Nerus, Terengganu, Malaysia*

[*]Corresponding author: mohdsukeri@umt.edu.my

One Sentence Summary: A new thiourea derivatives 3-MBTU was successfully synthesized and characterized. 3-MBTU can act as an ideal catalyst in Michael addition reaction of *N*-phenylmaleimide and Isobutyraldehyde.

Abstract: The present work deals with the synthesis of new carbonylthiourea derivatives namely 3-methyl-*N*-((3,3,5-trimethyl-5-((3-(3-methylbenzoyl)thioureido)methyl)cyclohexyl) carbamothioyl)benzamide (3-MBTU). The compounds were synthesized using condensation reaction between *m*-methylbenzoyl isothiocyanate and isophoronediamine. The synthesized compounds was characterized by IR, (^{1}H and ^{13}C) NMR and MS spectroscopy. The IR spectrum of the compound showed four significant stretching vibrations; N-H, C=O, C-N and C=S at 3235.07 cm^{-1}, 1667.95 cm^{-1}, 1152.28 cm^{-1} and 743.60 cm^{-1}, respectively. Proton NMR spectrum displayed all of the expected resonances of (C=S-N*H*) and (C=O-N*H*). Resonance of (C=S-N*H*) appeared at δ_H 11.27 and 11.30 ppm and resonance of (C=O-N*H*) appeared at δ_H 10.83 and 11.19 ppm. In the carbon-13 NMR spectrum, signals for carbon carbonyl (C=O) was observed at δ_C 168.38 and 168.62 ppm. Meanwhile, the carbon resonances for C=S appeared at δ_C 179.01 and 180.89 ppm. The synthesized compounds were tested as the organocatalyst in Michael addition reaction. The performances of the compounds as catalyst was monitored by Gas Chromatography-Flame Ionization Detector (GC-FID). The optimum condition reaction such as solvent effect, catalyst loading and different reaction time had been observed. Under the optimum condition, the percentage conversion obtained was 72%. Therefore, 3-MBTU can acts as an ideal potential catalyst in Michael addition reaction.

Introduction

Over the past decade, hydrogen-based organocatalysis has been well-recognized as a promising strategy in asymmetric synthesis [4]. Organocatalyst is small organic molecules such as thiourea and squaramide that increase the rate of reaction in various asymmetric reaction [10]. Organocatalyst became attractive because the absence of the transition metals that brings the advantage considering the principle of green chemistry. Green chemistry is chemistry that able to promote innovative technologies that reduce or eliminate the use or hazardous substances [9].

Most of the researchers were interested with thiourea as organocatalyst due to its ability to form an extensive of hydrogen bond and its unique characteristic of dual hydrogen bonding donor that work synergistically to achieve the activation of both nucleophile and electrophile in catalytic asymmetric reaction [3,7]

Recently, design and application of bifunctional organocatalysts have received much attention due to asymmetric organocatalysis emerging as a powerful and environmentally friendly methodology for the catalytic production of the valuable synthethic building blocks. Bifunctional organocatalyst is an activation both of the acceptor and donors simultaneously.In organic synthesis, organocatalyst widely applied in Michael addition of maleimide and isobutyraldehyde to produce substituted succinimide. Succinimides are an important class of heterocyclic compounds with various pharmacological applications in different fields [11]. In this study, with an interest in developing new bifunctional thiourea-based catalyst to achieve high levels of yields in Michael addition reaction of maleimide and isobutyraldehyde, we have designed a new organic catalyst that possesses two part of thiourea moiety.

Results

Synthesis and Characterization of 3-MBTU

IR spectrum of 3-MBTU showed all the expected bands of interest namely ν(N-H),ν(C=O),ν(C-N) and ν(C=S). The first absorption band was assigned as secondary amine which could be observed at 3235.07 cm^{-1} as medium intensity absorption band. The assignment of N-H at 3235.07 cm^{-1} due to the existence of C=O.....H-N intramolecular hydrogen bond which led to the formation of broad and weak absorption band of N-H stretching [5]. The strong absorption of ν (C=O) stretching band was observed at 1667.95 cm^{-1} which deviated from ordinary ν(C=O) stretching band which is commonly observed at around 1700 cm^{-1} due to the presence of intramolecular hydrogen bond, C=O…..H-N and resonance effect of nitrogen and carbonyl group [6]. Strong absorption of ν(C-N) absorption band that clearly been observed at 1152.28 cm^{-1}. The ν(C=S) can be observed at 743.60 cm^{-1}, apparently decrease in frequency compared to common vibration due to the formation of intramolecular hydrogen bond between C=O and N-H that caused the electronegativity property of NH group became stronger and increased the strength of double bond character of the C=S group and restricted the thioamides resonance [2]. Figure 1 show the IR spectrum of 3-MBTU.

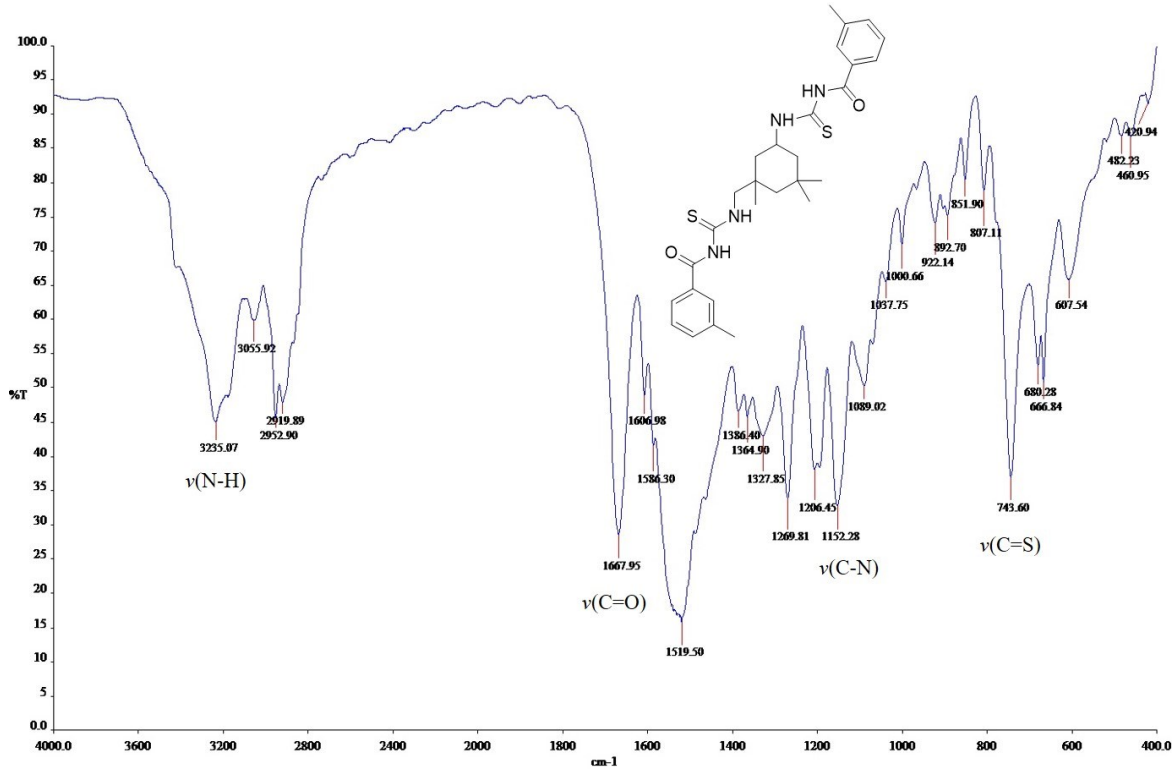

Figure 1 IR spectrum of 3-MBTU

In the proton NMR spectrum, the most upfield and shielded region was belongs to aliphatic proton that can be observed in the range of δ_H 0.93-1.26 ppm. Singlet proton resonances were observed in the range of δ_H 2.35-2.38 ppm which attributes to the methyl moieties at the phenyl ring. The unresolved resonance for aromatic protons was observed in the range of δ_H 7.37-7.80 ppm due to the overlapping between proton signals in the aromatic rings [13]. Resonance for C=S -NH proton appeared at δ_H 11.27 and 11.30 ppm meanwhile C=O-NH proton was detected at δ_H 10.83 and 11.19 ppm. Both of these resonances were observed at the most deshielded region in the spectrum due to the electron-withdrawing moieties which then decreased the electron density around the resonances and shifted to the downfield region. Meanwhile carbon NMR spectrum of 3-MBTU showed the upfield and shielded region at δ_C 20.76 and 23.14 ppm was belongs to methyl moieties. Carbon resonance of the alkyl group was detected at δ_C 26.68-48.30 ppm. While the signal for aromatic ring carbon was appeared in the range of δ_C 125.65-137.78 ppm. Two distinctive resonances can be observed at the most deshielded region which correspond to carbonyl (C=O) and (C=S). Carbon resonance for C=O can be observed at δ_C 168.38 and 168.62 meanwhile carbon resonance for C=S can be observed at δ_C 179.01 and 180.89 ppm. Table 1 showed chemical shift of ^1H and ^{13}C NMR of 3-MBTU. Figure 2 showed the ^1H NMR spectrum of 3-MBTU and Figure 3 showed the ^{13}C NMR spectrum of 3-MBTU.

	Moieties	Chemical shifts δ_H, (ppm)
^{1}H NMR	(m, 18H, $C_{10}H_{18}$)	0.94–1.26
	(s, 6H, 2×CH_3)	2.35, 2.37
	(m, 8H, 2×C_6H_4)	7.37–7.80
	(m, 1H, NH)	10.83
	(m, 1H, NH)	11.19
	(s, 1H, NH)	11.27
	(s, 1H, NH)	11.30
^{13}C NMR	(2×CH_3)	20.76, 23.14
	($C_{10}H_{18}$)	26.68–48.30
	(2×CH ar)	125.65–137.78
	(2×C=O)	168.38, 168.62
	(2×C=S)	179.01, 180.89

Table 1 Chemical shift of ^{1}H and ^{13}C NMR of 3-MBTU

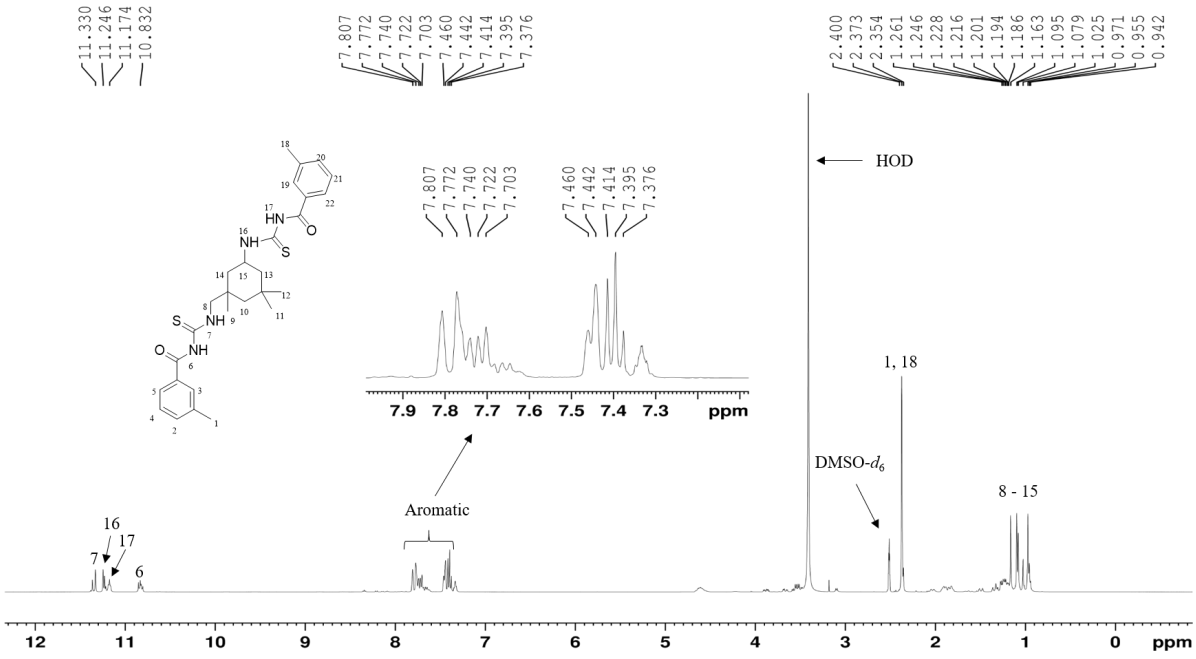

Figure 2 ^{1}H NMR spectrum of 3-MBTU

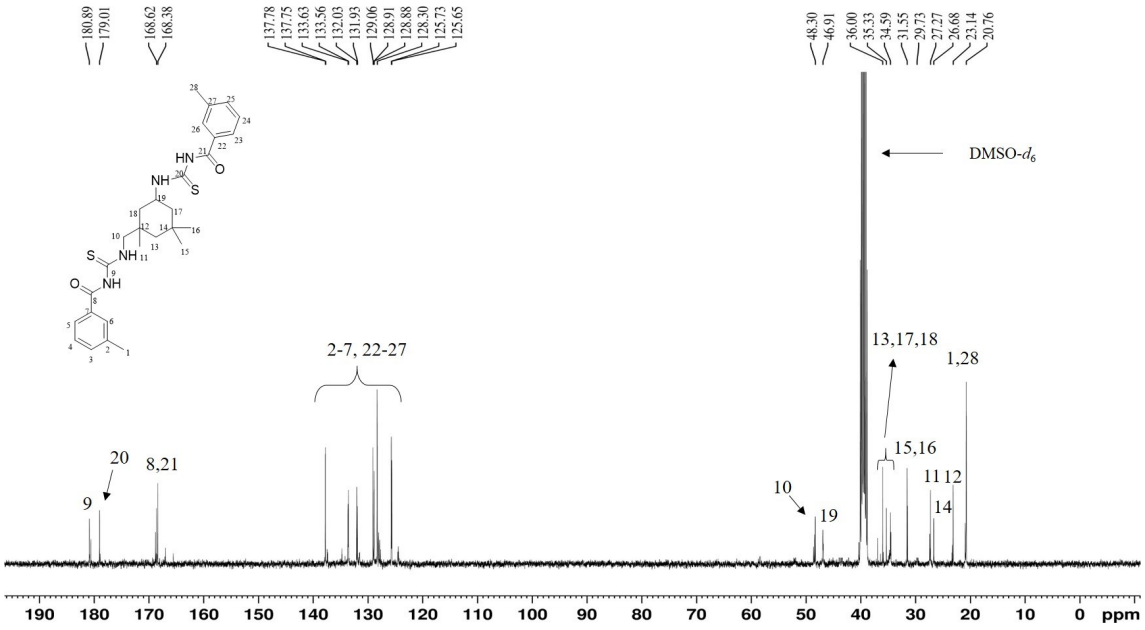

Figure 3 ^{13}C NMR spectrum of 3-MBTU

In the mass spectrum, the molecular ion $[M]^+$ of 3-MBTU was recorded in good agreement with the theoretical value. Molecular ion $[M]^+$ was observed in weak intensity at *m/z* 265 amu. The sample observed in weak intensity due to the unsuitable temperature and pressure causing the molecular ion unstable. The base peak was appeared at *m/z* 119 amu which assigned to the cleavage fragment of methyl benzoyl. Figure 4 showed the mass spectrum of 3-MBTU.

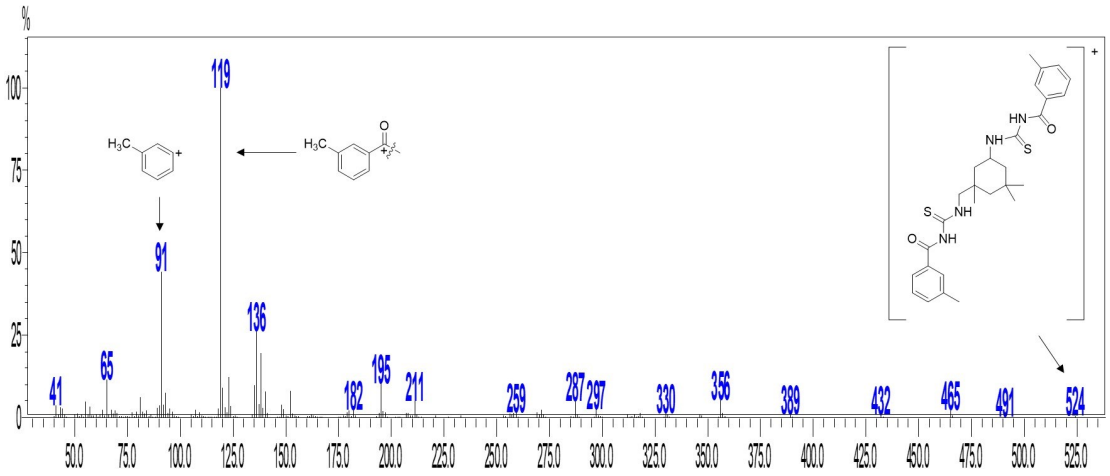

Figure 4 Mass spectrum of 3-MBTU

Evaluation of catalytic activity of 3-MBTU as organocatalyst

The catalytic activity of 3-MBTU was evaluated in Michael addition reaction of *N*-phenymaleimide with isobutyraldehyde. Scheme 1 show general scheme for the Michael addition reaction. The catalytic activity of 3-MBTU was optimized using three parameter which are solvent, catalyst loading and reaction time to exhibit high efficiency of catalytic performance.

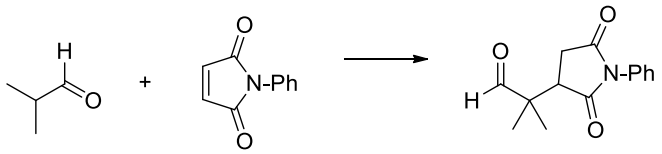

Isobutyraldehyde *N*-Phenylmalemide 2-(2,5-Dioxo-1-phenylpyrrolidin-3-yl)-2-methylpropanal.

Scheme 1 General scheme for Michael addition reaction of *N*-phenylmaleimide and Isobutyraldehyde.

The performance of catalyst is strongly influenced by the solvent used in the catalytic process. Solvent can affect the catalyst reaction with respect to the rate of the reaction, yield and selectivity. The effect of different solvent has been observed using dichloromethane, toluene and methanol. The reaction were carried out for 6 h at room temperature with 20 mol% catalyst loading. The percentage conversion obtained was summarized in Table 2.

Solvent	Conversion of *N*-phenylmaleimide (%)
Dichloromethane	59
Toluene	45
Methanol	12

Table 2 Effect of solvent in Michael addition reaction using 3-MBTU as organocatalyst

Based on Table 2, polar aprotic solvent proceeded the reaction with high percentage of conversion because polar aprotic solvent help to stabilize the highly reactive catalytic intermediate and has high solubility for reagent [12]. Percentage of conversion of *N*-phenylmaleimide using toluene as a solvent was slightly lower compare to dichloromethane. Toluene is non polar solvent that also help to stabilize the highly reactive catalytic intermediate but it has low solubility for reagent. During the preparation for the catalytic reaction, the reactant was less soluble in toluene compare to dichloromethane. Meanwhile using methanol was less efficient due to the formation of hydrogen bond between substrate and solvents. Besides, methanol also would coordinate strongly to the catalyst that prevent further reaction with the substrates. As a result, dichloromethane was selected as a suitable solvent in this reaction.

The reaction condition was further optimized for catalyst loading. The amount of catalyst presents in the system could affect the efficiency of the catalytic activity [8]. Result obtained was summarized in Table 3.

Catalyst Loading (mol%)	Conversion of *N*-phenylmaleimide (%)
10	45
20	59
30	61

Table 3 Effect of catalyst loading in Michael addition reaction using 3-MBTU as organocatalyst

As shown in Table 3, the conversion of *N*-phenylmaleimide was increased from 45% to 59% when increasing the catalyst loading from 10 mol% to 20 mol%, respectively. While further increasing of catalyst loading, insignificant increase was observe. This is due to the catalyst satiration at 20 mol% and further addition of catalyst caused a negligible effect. Thus, 20 mol% of catalyst loading was chosen to test next parameter.

The reaction time was carried out at different interval of time, which are 6,12,24,48 and 72 hours. The result obtained are summarized in Table 4.

Time (hours)	Conversion of *N*-phenylmaleimide (%)
6	59
12	61
24	72
48	72
72	72

Table 4 Effect of reaction time in Michael addition reaction using 3-MBTU as organocatalyst

From table 4, it showed that the reaction was only active up to 24 h with 72% of conversion. After 24 h, the conversion was constant for both catalysts due to the saturation between catalyst and reactant. Therefore, in this reaction, 24 h reaction time was the suitable condition for the use of 3-MBTU as organocatalyst.

In this study, the catalytic activity of 3-MBTU was achieved the conversion up to 72%. The best condition to apply 3-MBTU as organocatalyst in Michael addition reaction of *N*-phenylmaleimide and isobutyraldehyde was 20 mol% of catalyst loading in dichloromethane at 24 h reaction period.

Discussion

In this report, the synthesis of new carbonylthiourea derivatives, which are 3-MBTU was successfully obtained. 3-MBTU was characterized by FTIR, NMR and MS. *Th*e FTIR spectra showed the existence of important stretching bands of ν(N-H), ν(C=O), ν(C-N) and ν(C=S). Proton NMR and Carbon-13 NMR spectra data obtained were in good agreement with the proposed molecular structure of the compounds. The catalytic performances of 3-MBTU was analyzed using GC-FID. The higher percentage conversion of 3-MBTU obtained was 72 % with 20 mol% of catalyst loading in dichloromethane at 24 h reaction period. In short, the results revealed 3-MBTU have been successfully obtained and showed good potential as organocatalysts in Michael addition reaction.

Materials and Methods

Chemicals and Materials

All solvents and chemicals used in this study were purchased from Sigma Aldrich and Merck and have been used directly without further purification.

Instrumentation

The Infra-Red (IR) spectra of the compounds *were recorded using FTIR Perkin Elmer 100 Spectrometer within spectral range of 4000-400 cm^{-1}. The ^{1}H and ^{13}C NMR spectra were recorded using Bruker Avance III 400 spectrometer in deuterated dimethylsulfoxide (DMSO-d_6). The catalytic study of the compounds was supported by Shimadzu GC-FID 2010 instrument in order to identify the percentage conversion of N-phenylmaleimide.*

Synthesis of 3-MBTU

A solution of ammonium thiocyanate (3.24 g, 20.00 mmol) in acetone (30mL) was added dropwise into *m*-tolouyl chloride (1.55 g, 20.00 mmol) solution which dissolve separately in 30 mL acetone. The mixture was stirred at room temperature for 10 minutes. A solution of isophoronediamine (1.73 g, 10.00 mmol) in 30 mL acetone was then added into the reaction mixture. The mixture was stirred and reflux for *ca.* 1 hours. The resulting solution was filtered into a beaker containing ice cubes. The solid product formed was then recrystallized by methanol to give colourless crystals. Yield 57 %.

Application of 3-MBTU as organocatalyst in Michael addition

The preparation for the catalytic study has been based on the work by Bai and co-workers (2010) with minor modification [1]. In this study, the solution of 3-MBTU (0.08 mmol, 0.03 g) in 5 mL of dichloromethane was added with isobutyraldehyde (1.2 mmol, 0.09 g) and *N*-phenylmaleimide (0.4 mmol, 0.07 g). The mixture was stirred at room temperature. After stirring, the mixture was injected into the injection port of GC-FID to resolve the performance of catalytic activities.

References and Notes:

1. Bai, J.-F., Peng, L., Wang, L.-l., Wang, L.-X., & Xu, X.-Y.(2010). Chiral primary amine thiourea promoted highly enantioselective Michael reactions of isobutylaldehyde with maleimides. *Tetrahedron*, *66*(46), 8928-8932.
2. Estévez-Hernández, O., Otazo-Sánchez, E., de Cisneros, J. H. H., Naranjo-Rodríguez, I., & Reguera, E. (2005). A Raman and infrared study of 1-furoyl-3-monosubstituted and 3, 3-disubstituted thioureas. Spectrochimica Acta Part A: Molecular and Biomolecular Spectroscopy, 62(4-5), 964-971.
3. Fang, X., & Wang, C. J. (2015). Recent advances in asymmetric organocatalysis mediated by bifunctional amine–thioureas bearing multiple hydrogen-bonding donors. *Chemical Communications*, *51*(7), 1185-1197.
4. Horitsugi, N., Kojima, K., Yasui, K., Sohtome, Y., & Nagasawa, K. (2014). Asymmetric Michael Reaction of Nitroolefins with β- Dicarbonyl Compounds Catalysed by 1, 3 β- Diamine- Tethered Guanidine- Thiourea Bifunctional Organocatalysts. *Asian Journal of Organic Chemistry*, *3*(4), 445-448.
5. Karipcin, F., Atis, M., Sariboga, B., Celik, H., & Tas, M. (2013). Structural, spectral, optical and antimicrobial properties of synthesized 1-benzoyl-3-furan-2-ylmethyl-thiourea. *Journal of Molecular Structure*, *1048*, 69-77.
6. Khairul, W. M., Tukimin, N., & Rahamathullah, R. (2016). Synthesis, Characterization and Electrical Properties of N-([4-(aminophenylethynyl) toluene]-N'-(cinnamoyl) thiourea (AECT) as Single Molecular Conductive Film. SAINS MALAYSIAN, 45(5), 825-831.
7. Kumari, R. G., Ramakrishnan, V., Carolin, M. L., Kumar, J., Sarua, A., & Kuball, M. (2009). Raman spectral investigation of thiourea complexes. *Spectrochimica Acta Part A: Molecular and Biomolecular Spectroscopy*, *73*(2), 263-267.
8. Radwan, N. R., Hagar, M., Afifi, T. H., Al-wadaani, F., & Okasha, R. M. (2018). Catalytic Activity of Sulfated and Phosphated Catalysts towards the Synthesis of Substituted Coumarin. Catalysts, 8(1), 36.
9. Shaikh, I. R. (2014). Organocatalysis: key trends in green synthetic chemistry, challenges, scope towards heterogenization, and importance from research and industrial point of view. *Journal of Catalysts*, *2014*.
10. Takemoto, Y. (2005). Recognition and activation by ureas and thioureas: stereoselective reactions using ureas and thioureas as hydrogen-bonding donors. Organic & biomolecular chemistry, 3(24), 4299-4306.
11. Vo-Hoang, Y., Gasse, C., Vidal, M., Garbay, C., & Galons, H. (2004). Efficient synthesis of *N*-benzyl-3-aminopyrrolidine-2, 5-dione and *N*-benzyl-3-aminopyrrolidin-2-one. *Tetrahedron letters*, *45*(18), 3603-3605.
12. Wittkopp, A., & Schreiner, P. R. (2003). Metal□Free, Noncovalent Catalysis of Diels–Alder Reactions by Neutral Hydrogen Bond Donors in Organic Solvents and in Water. *Chemistry–A European Journal*, *9*(2), 407-414.
13. Yusof, M. S. M., Khairul, W. M., & Yamin, B. M. (2010). Synthesis and characterisation a series of N-(3, 4-dichlorophenyl)-N′-(2, 3 and 4-methylbenzoyl) thiourea derivatives. Journal of Molecular Structure, 975(1), 280-284.

Acknowledgments: The authors gratefully acknowledged Ministry of Higher Education Malaysia for FRGS *research grant No: 59390 and Universiti Malaysia Terengganu for providing research facilities.*

Effect of deposition temperature of $Cu_2Zn_xFe_{1-x}SnS_4$ thin films grown by thermal evaporation

Authors: H. Oueslati[1,]*, M. Ben Rabeh[1], M. Kanzari[2]

Affiliations:
[1]*Université de Tunis El Manar, Ecole Nationale d'Ingénieurs de Tunis, Laboratoire de Photovoltaïques et Matériaux Semi-conducteurs, BP 37 Le Bélvédère 1002, Tunis, Tunisie.*
[2]*Université de Tunis, Institut préparatoire aux études d'ingénieurs de Tunis, Laboratoire de Photovoltaïques et Matériaux Semi-conducteurs, BP 37 Le Bélvédère 1002, Tunis, Tunisie.*

**Corresponding author:weslatihiba90@gmail.com*

Summary: Variation of substrate temperature affects structural and morphological properties of $Cu_2ZnxFe_{1-x}SnS_4$.

Abstract: In the present work, $Cu_2Zn_xFe_{1-x}SnS_4$ (CZFTS) (x=0; 0.25; 0.5; 0.75; 1) thin films were elaborated by thermal evaporation under vacuum on heated glass substrates at various deposition temperature (25, 100, 150, 200° C). The influence of substrate temperature on compositional, structural and morphological properties were studied. Elemental composition analysis reveals the presence of four metallic elements such as Cu, Fe, Zn and Sn, as well as sulphur in non-stoichiometric proportions. The XRD analysis showed that CZFTS thin films deposited on unheated glass substrate are amorphous. After heating substrates, CZFTS phase appears with a preferred orientation along (112) plane. In addition, XRD results indicated that CFTS (x=0) and CZTS (x=1) materials crystallize respectively in stannite and kesterite structure and a transition phase has been occurred at x=0.5 with reducing Fe [1, 2]. Microtructural parameter evaluation were indicated that CZFTS thin films elaborated at 100°C exhibit the highest crystallite size and the lowest strain. Atmoic force microscopy showed the presence of large grain over the entire surface for all CZFTS thin films. Finally, we conclude that the variation of substrate temperature affects the properties of CZFTS thin films. The suitability of CZFTS films make these appropriate for used as absorbers in tandem solar cells.

Introduction

Presently, researches on thin film solar cells with low cost are developed. Various renowned materials like CdTe, $CuInS_2$ and $Cu_2InGaS2$ have been significantly studied for solar cells application (1-3). CIGS based solar cells have achieved an important photo conversion efficiency (4). But, the scarcity and expensive elements of Tellurium, Indium and Gallium, the toxicity of Cadmium make the production of the photovoltaic devices limited. To solve this problem, it is necessary to explore new alternative materials that are contain abundant, non-toxic and low cost elements. In this context, researchers have focused on the chalcogenide family, like Cu_2ZnSnS_4 (CZTS) and Cu_2FeSnS_4 (CFTS) semiconducting materials composed by less toxic, low cost and easily available elements. These materials are considered among the most candidate used for solar cells application due to suitable band gap between 1.2 and 1.5 eV, large absorption coefficient exceed 10^4 cm^{-1} and a *p* type intrinsic conductivity (5-8). Quaternary CZTS and CFTS crystallizes respectively in kesterite (I-4) and stannite (I-42m) structure (9). It have nearly a similar crystalline structures with different space groups due to the different distributions of Cu^{+1}, Zn^{+2} and Fe^{+2} cations (9). In recent years, CZTS and CFTS achieved a power conversion efficiency of 12.6% and 8.03% respectively, made them a very strong candidatures in the photovoltaic industry (10,11). However, some works are interested for the next generation $Cu_2Zn_xFe_{1-x}SnS_4$ (CZFTS) by changing Fe content and studied the effect on the physico-chemical properties. However, a several methods are reported for the synthesis of multi-ternary CZFTS using pulsed laser (12), solvothermal (13, 14), chemical spray pyrolysis (15) and facile solution (16).
In this work, we investigated the preparation of $Cu_2Zn_xFe_{1-x}SnS_4$ (x=0 ; 0.25; 0.5; 0.75; 1) by thermal evaporation onto heated glass substrates. We studied the effect of temperature deposition on compositional, structural and morphological properties.

Materials and Methods

$Cu_2Zn_xFe_{1-x}SnS_4$ powders by varying x were synthesized by direct melting method of constituent elements (see Figure S1 in supplementary materials). The resulting powders were used for the deposition of $Cu_2Zn_xFe_{1-x}SnS_4$ thin films were on heated glass substrates by vacuum thermal evaporation method, using a molybden crucible. The elemental composition were analyzed by energy dispersive spectroscopy (EDS) and structural properties of

CZFTS thin films were were carried out using X-ray diffraction (XRD). XRD was operated in the 2θ range from 20° to 70° on an X'Pert PRO PANalytical diffractometer in Bragg-Brentano geometry (θ/2θ) with Cu K_α radiation at λ=1.54056 Å. Morphological properties were examined by atomic force microscopy (AFM).

Results and Discussion

Compositional study

The elemental composition of the thin films was determined by EDS analysis for different deposition temperatures ranging from 25°C to 200 °. The atomic percentages on $Cu_2Zn_xFe_{1-x}SnS_4$ (x=0 ; 0.25; 0.5; 0.75; 1) are shown in Table 1. We clearly observe the presence of four metal cations such as Cu, Fe, Zn and Sn as well as sulfur but with proportions that do not correspond to stoichiometry. However, it is noted that the heating of the substrates affects the chemical composition of the CZFTS thin films.

As indicated in the table, all the compositions are Cu and Sn rich, this difference in stoichiometry can generate either secondary phases or intrinsic defects. Knowing that such a composition leads to the formation of the CuS and SnS binary phase and / or the Cu-Sn-S ternary phase. In addition, it's observed that all the compositions are deficient in sulfur, this deficit become higher by increasing the substrates temperature. This effect is explained by the high saturation vapor pressure of sulfur, as a very volatile element. Thus, it is perhaps the reason for the Cu richness in the CZFTS layers during the deposition. This observation were reported in previous work how studied the dependence of substrate temperature on chemical composition of Cu_2FeSnS_4 and Cu_2ZnSnS_4 (17-20).

Noting that if the atomic ratio Cu / (Fe + Zn + Sn)> 1, the compositions are well rich in Cu whereas if the ratio (Fe + Zn) / Sn <1 the compositions are rich in Sn. Therefore, by increasing the substrates temperature, the copper concentration increases while the tin concentration decreases, in the range of $0 \leq x \leq 0.5$ and vice versa for $x \geq 0.5$.

	(a) T_s =25°C						
Theoretical composition	**Chemical composition [%at]**					**Atomic ratio**	
	Cu	**Zn**	**Fe**	**Sn**	**S**	$\frac{Cu}{Fe+Zn+Sn}$	$\frac{Zn+Fe}{Sn}$
Cu_2FeSnS_4	38.3	-	8.18	13.25	40.26	1.79	0.62
$Cu_2Zn_{0.25}Fe_{0.75}SnS_4$	35.65	3.84	5.88	13.85	40.76	1.51	0.7
$Cu_2Zn_{0.5}Fe_{0.5}SnS_4$	34.52	3.19	6.6	15.01	40.23	1.36	0.65
$Cu_2Zn_{0.75}Fe_{0.25}SnS_4$	31.35	10.27	1.37	16.3	40.73	1.12	0.71
Cu_2ZnSnS_4	29.7	13.08	-	17.61	40.57	0.97	0.74

Theoretical composition	(b) Ts=100°C						
	Chemical composition [%at]					Atomic ratio	
	Cu	Zn	Fe	Sn	S	$\frac{Cu}{Fe+Zn+Sn}$	$\frac{Zn+Fe}{Sn}$
Cu_2FeSnS_4	36.01	-	10.05	14.85	39.46	1.44	0.68
$Cu_2Zn_{0.25}Fe_{0.75}SnS_4$	33.54	3.36	8.34	14.9	39.84	1.26	0.78
$Cu_2Zn_{0.5}Fe_{0.5}SnS_4$	32.62	5.88	5.58	15.96	39.91	1.19	0.72
$Cu_2Zn_{0.75}Fe_{0.25}SnS_4$	33.87	8.08	2.55	15.07	39.89	1.32	0.7
Cu_2ZnSnS_4	33.01	11.77	-	15.52	39.71	1.21	0.76

Theoretical composition	(c) T_s=150°C						
	Chemical composition [%at]					Atomic ratio	
	Cu	Zn	Fe	Sn	S	$\frac{Cu}{Fe+Zn+Sn}$	$\frac{Zn+Fe}{Sn}$
Cu_2FeSnS_4	33.64	-	10.53	16.55	38.67	1.24	0.64
$Cu_2Zn_{0.25}Fe_{0.75}SnS_4$	32.48	3.08	8.63	16.2	38.6	1.16	0.72
$Cu_2Zn_{0.5}Fe_{0.5}SnS_4$	37.44	5.75	2.58	14.84	39.4	1.61	0.56
$Cu_2Zn_{0.75}Fe_{0.25}SnS_4$	36.96	8.23	2.17	13.57	39.07	1.54	0.77
Cu_2ZnSnS_4	37.45	10.47	-	12.43	39.63	1.63	0.84

Theoretical composition	(d) T_s=200°C						
	Chemical composition [%at]					Atomic ratio	
	Cu	Zn	Fe	Sn	S	$\frac{Cu}{Fe+Zn+Sn}$	$\frac{Zn+Fe}{Sn}$
Cu_2FeSnS_4	32.25	-	10.85	17.85	38.03	1.12	0.6
$Cu_2Zn_{0.25}Fe_{0.75}SnS_4$	31.44	3.62	8.36	17.2	38.06	1.07	0.7
$Cu_2Zn_{0.5}Fe_{0.5}SnS_4$	37.6	5.25	5.44	12.95	38.75	1.59	0.83
$Cu_2Zn_{0.75}Fe_{0.25}SnS_4$	39.22	8.32	2.52	11.07	38.85	1.79	0.98
Cu_2ZnSnS_4	39.06	11.7	-	10.87	38.37	1.73	1.08

Table 1.

XRD analysis

Figure 1, illustrates the XRD patterns of $Cu_2Zn_xFe_{1-x}SnS_4$ (x = 0; 0.25; 0.5; 0.75; 1) thin films deposited at various substrates temperature from 25°C to 200°C. For the layers deposited on unheated substrates (Ambient temperature≈25 ° C), it is noted that CZFTS films are amorphous with the presence of small weak peaks, attributed to secondary SnS (JCPDS, No. 00-053-0526) and CuS (JCPDS, No. 0.-065-3556) because of a composition rich in copper and tin. On the other hand we found a hump located at 28.61 ° and a peak located at 28.71 ° for respectively x = 0.75 and 1 indicating a low crystallinity of the layers.

After heating the substrates, Figure 1 (b, c, d) we noticed the appearance of diffraction peaks relative to CZFTS phases at 28 °, 32 ° and 47 ° corresponding (112), (200) / (004) and (204) / (220) planes respectively characteristic of the stannite structure (CFTS) and the kesterite structure (CZTS). The peaks are determined for Cu2ZnxF1-xSnS4 based upon JCPDS n° 044-1476, 083-2262, 065-3751, 083-2261 and 026-0575. Indeed, when the deposition temperature increases, the intensity of the diffraction peak enriched and thereafter the amorphous background weakened. Previous work has been investigated an enhanced of crystallinity with increases substrates temperature (17-20).This performance is owing to the fact that the heated substrates generates enough energy to allow the atoms diffusion and occupation of a normal position in the crystal lattice, which has the effect of improving the crystallinity of the layers. However, for x≤0.5, the appearance of secondary phases CuS and SnS decrease with rising the substrates temperature.

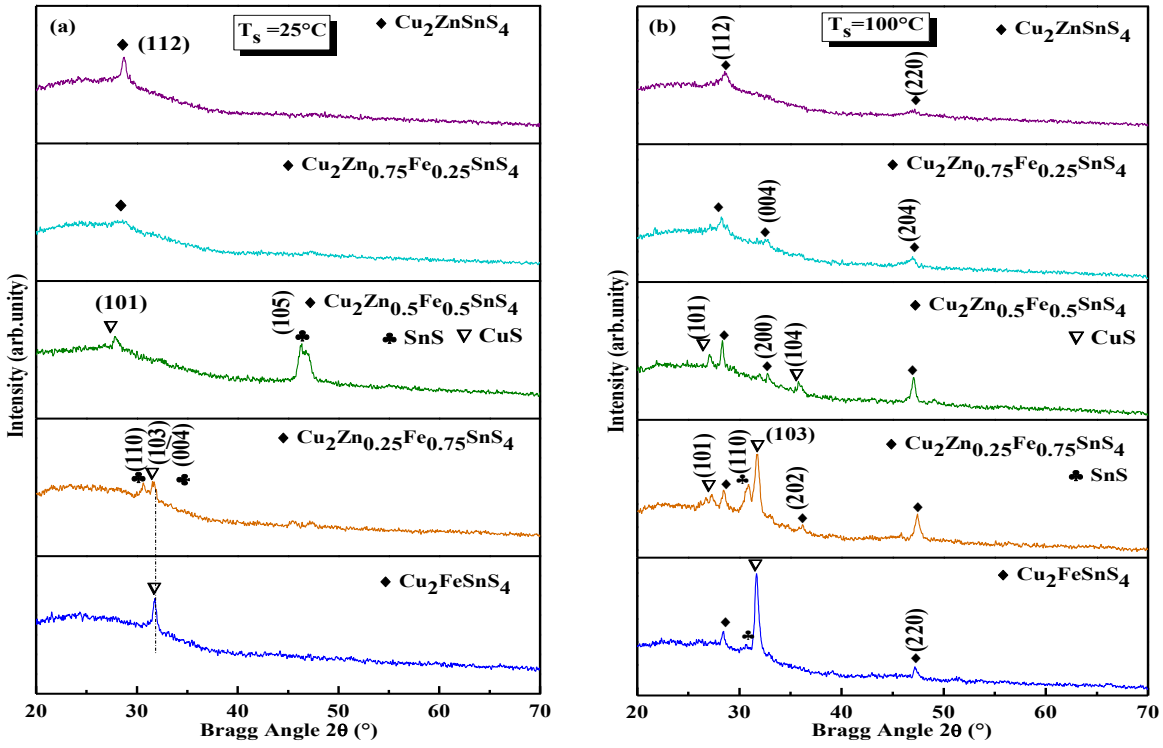

Fig. 1.

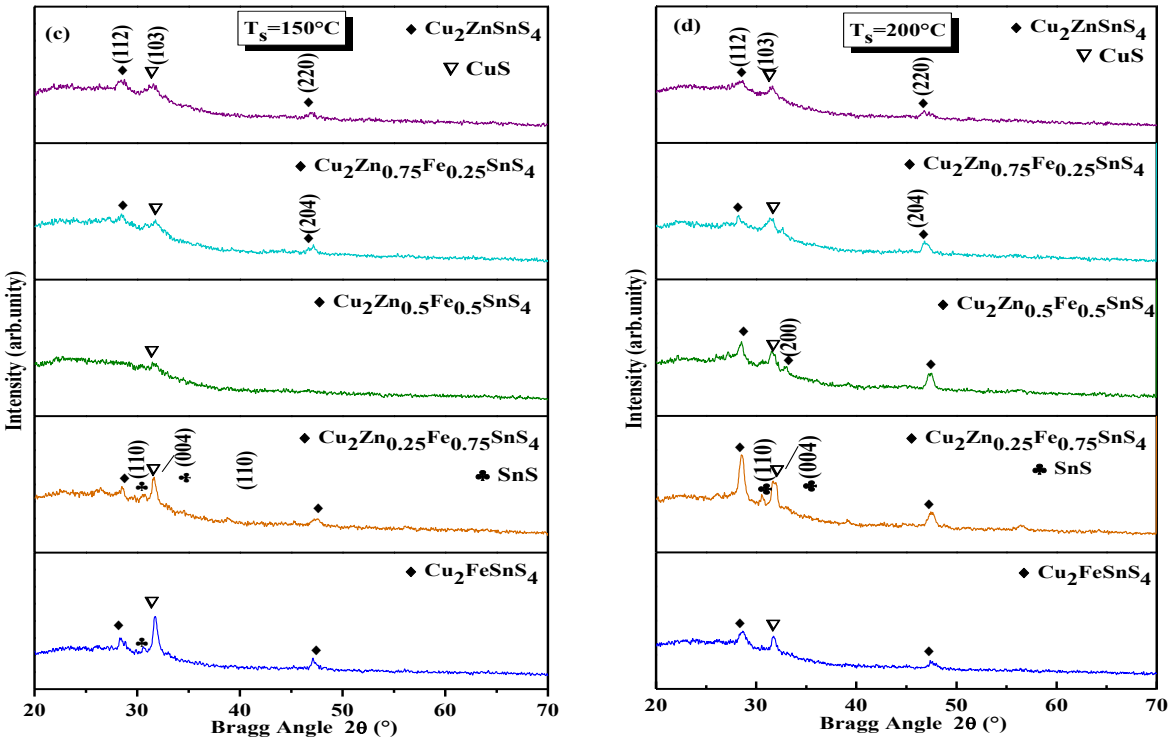

Fig. 1.

Crystallite size of prepared CZFTS thin films was estimated using Debye Scherer's formula (21):

$$D = \frac{0.9\lambda}{\beta cos\theta}$$

Where λ is the wavelength of X-ray diffraction, θ is the diffraction angle and β is the full width at half height (FWHM) of the most intense peak, expressed in Radians. Also, the strain were evaluated from the relation (21):

$$\varepsilon = \frac{\beta cos\theta}{4}$$

It is found that the heating of the substrates substantially affects the crystallites size, as shown in table 2. The crystallites size decreases by increasing the temperature of the substrates inversely for the stress. This allows us to deduce that the sample deposited at temperature 100 ° C has the best crystalline quality. Thus, by varying x, it is noted that the crystallite size upsurges by reducing the Fe content, caused by the phase transition of the stannite structure to the kesterite structure.

D (nm)					
$Cu_2Zn_xFe_{1-x}SnS_4$	**x=0**	**x=0.25**	**x=0.5**	**x=0.75**	**x=1**
T_s=100°C	26	24	22	20	17
T_s=150°C	11	14	15	13	8
T_s=200°C	20	17	-	16	14

ε (×10^{-3})					
$Cu_2Zn_xFe_{1-x}SnS_4$	**x=0**	**x=0.25**	**x=0.5**	**x=0.75**	**x=1**
T_s=100°C	1.31	1.43	1.57	1.74	2
T_s=150°C	1.77	1.98	-	2.2	2.38
T_s=200°C	2.82	2.4	2.28	2.71	4.17

Table 3

Morphological properties

Figure 2 shows the AFM micrographs of CZFTS thin films grown at various deposition temperature, in 3D representation measured on a surface 2 × 2 μm^2.

It is clear from figure 3 that the morphology of films is influenced by the increase of the substrates temperature. Indeed, it is noted that the surfaces are uniform and rough with the presence of spherical grains shapes, which change size by varying the substrates temperature and Fe content. In addition, a few voids between grains were present that is strongly due to poor crystallinity and the presence of secondary phases.

Table 3, regrouped the values of the roughness given by AFM for each substrate temperature by varying the composition x. In this study, we have estimated the root mean square roughness, which is defined as the difference between the average height of the profile and the baseline.

Further, we remarked that the value of roughness of the thin layers has increased with the substrates temperature. It is also noted that the roughness increases by decreasing the Fe content.

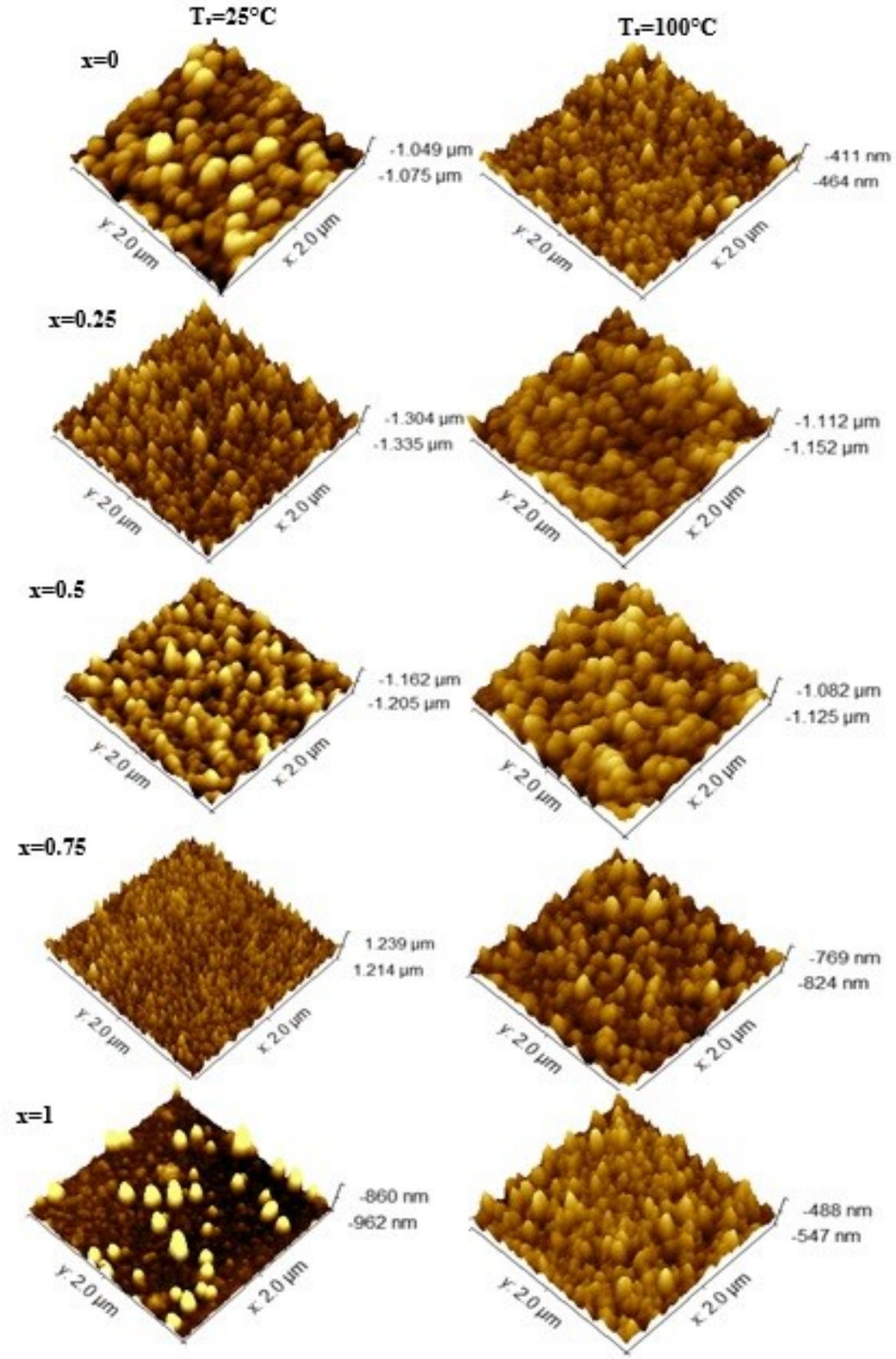
T=25°C
T=100°C
x=0
-1.049 µm
-1.075 µm
-411 nm
-464 nm
x=0.25
-1.304 µm
-1.335 µm
-1.112 µm
-1.152 µm
x=0.5
-1.162 µm
-1.205 µm
-1.082 µm
-1.125 µm
x=0.75
1.239 µm
1.214 µm
-769 nm
-824 nm
x=1
-860 nm
-962 nm
-488 nm
-547 nm
y 2.0 µm
x 2.0 µm

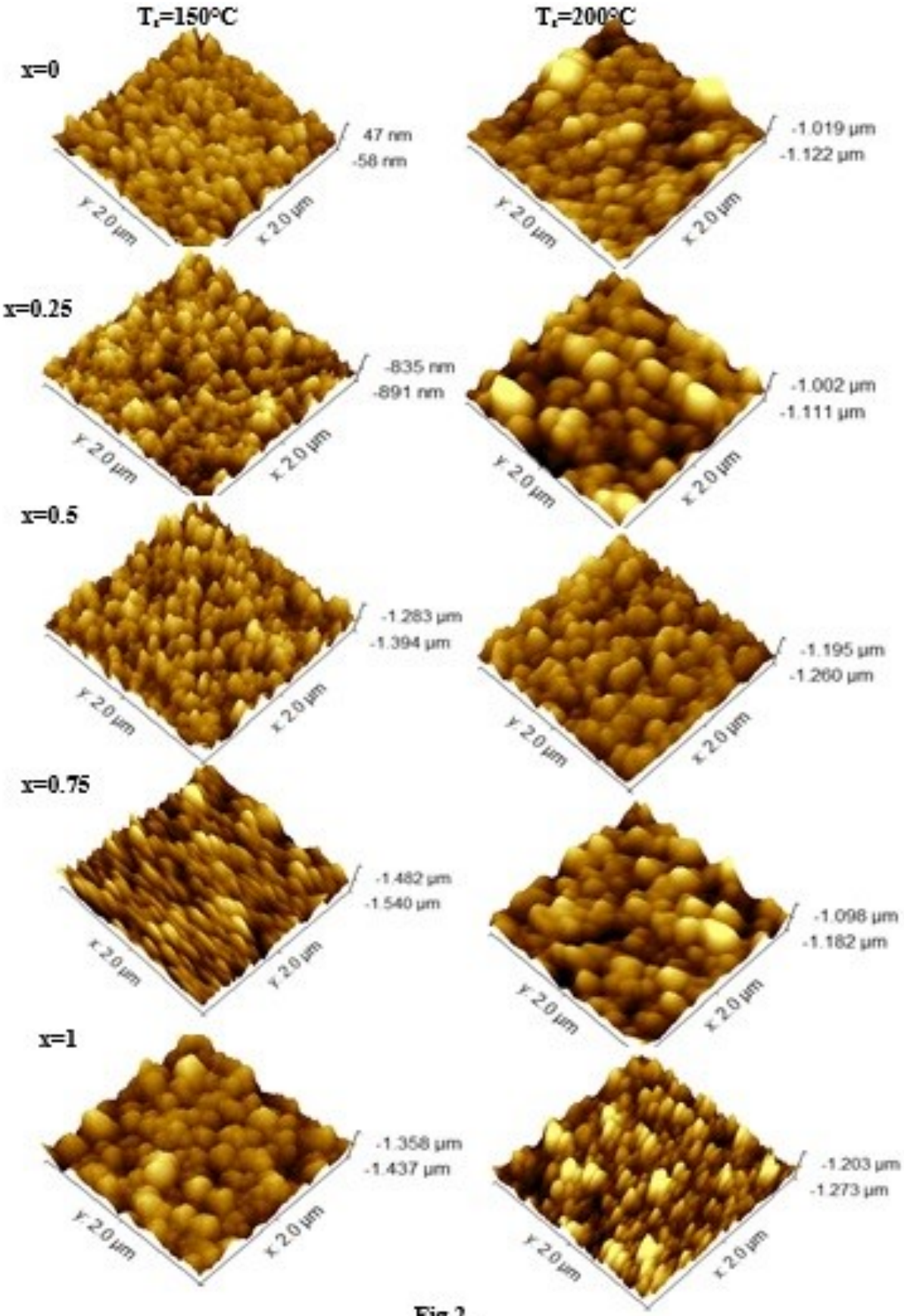
T=150°C
T=200°C
x=0
47 nm
-58 nm
-1.019 µm
-1.122 µm
x=0.25
-835 nm
-891 nm
-1.002 µm
-1.111 µm
x=0.5
-1.283 µm
-1.394 µm
-1.195 µm
-1.260 µm
x=0.75
-1.482 µm
-1.540 µm
-1.098 µm
-1.182 µm
x=1
-1.358 µm
-1.437 µm
-1.203 µm
-1.273 µm
Y 2.0 µm
X 2.0 µm

Fig 2.

RMS (nm)					
$Cu_2Zn_xFe_{1-x}SnS_4$	x=0	x=0.25	x=0.5	x=0.75	x=1
$T_{s\ ambiante}$	3.49	4.59	6.07	6.97	7.13
T_s =100°C	5.58	6.99	7.08	7.87	8.55
T_s=150°C	7.86	8.46	8.89	9.86	11.33
T_s=200°C	10.36	11.22	12.63	13.40	9.63

Table 4.

Conclusion

Multi-ternary CZFTS by varying x were successfully deposited onto heated glass substrates by thermal evaporation. The analysis of t results showed us well that the CZFTS films are affected by the variation of deposition temperature. However, the elaborate CZFTS thin films have poor crystallinity because they have a non-stoichiometric composition that leads to the formation of secondary phases. It can be concluded therefore that the heating of the substrates is insufficient to have thin layers of stoichiometric and well crystallized CZFTS materials. In fact, the films produced by thermal evaporation in vacuum generally have a sulfur deficiency that can only be remedied after annealing under a sulfur atmosphere.

Supplementary Materials

Figure S1. XRD diagrams of $Cu_2ZnxFe1_{-x}SnS_4$ (x=0 ; 0.25; 0.5; 0.75; 1) synthesized powders.

Acknowledgments:
The authors are grateful to Charles Coulomb Laboratory, university of Montpellier, France, for providing EDS and AFM analysis facility, and the Tunisian Ministry of Higher Education and Scientific Research for financial support of this work.

References

1. Seiki Teraji, Jakapan Chantana, Taichi Watanabe, Takashi Minemoto, Development of flexible Cd-free Cu(In,Ga)Se2 solar cell on stainless steel substrate through multi-layer precursor method, *J. Alloys Comp*., 756, 111-116 (2018).
2. Yu. P. Gnatenko, P. M. Bukivskij, A. P. Bukivskii, M. S. Furier, Effect of Dy-doping on photoluminescence properties of CdTe crystals and their defect structure, *Physica B* 546 89-92 (2018).
3. T. Feurer, P. Reinhard, E. Avancini, B. Bissig, J. Löckinger, P. Fuchs, R. Carron, T.P. Weiss, J. Perrenoud, S. Stutterheim, S. Buecheler, A. N. Tiwari, Progress in thin film CIGS photovoltaics – Research and development, manufacturing, and applications, *Prog. Photovolt. Res. Appl.* 25 645–667 (2017).
4. Green, M. A.; Emery, K.; Hishikawa, Y.; Warta, W.; Dunlop, E. D. Solar Cell Efficiency Tables (version 42). *Prog. Photovoltaics*, 21, 827−837 (2013).
5. H. Guan, H. Shen, B. Jiao, X. Wang, Structural and optical properties of Cu_2FeSnS_4 thin film synthesized via a simple chemical method, *Mater. Sci. Semicond. Process.,* 25, 159–162 (2014).
6. S. Chatterjee and A.J. Pal, A solution approach to p-type Cu_2FeSnS_4 thin-films and pn-junction solar cells: Role of electron selective materials on their performance, *Sol. Energy Mate. Sol. Cells,* 160, 233–240 (2017).
7. N. Thota, M. Gurubhaskar, A. C. Kasi Reddy, G. Hema Chandra, B. R. Mehta, Ashutosh Tiwari and Y. P. Venkata Subbaiah, Growth and properties of Cu_2ZnSnS_4 thin films prepared by multiple metallic layer stacks as a function of sulfurization time, *J. Mater Sci: Mater Electron,* 28, 11702–11711(2017).
8. S-Y. Li, C. Hägglund,Y. Ren, Jonathan J.S. Scragg, J. K. Larsen, C. Frisk, K. Rudisch, S. Englund and C. Platzer-Björkman, Optical properties of reactively sputtered Cu_2ZnSnS_4 solar absorbers determined by spectroscopic ellipsometry and spectrophotometry, *Sol. Energy Mater. Sol. Cells,* 149, 170–178 (2016).
9. S. R. Hall, J. T. Szymanski, J. M. Stewart, Kesterite $Cu_2(Zn,Fe)SnS_4$ and Stannite $Cu_2(FeZn)SnS_4$ Structurally Similar but distinct minerals, *Can. Miner.,* 16, 131–137 (1978).
10. W. Wang, M. T. Winkler, O. Gunawan, T.Gokmen, T. K. Todorov, Y. Zhu, D. B. Mitzi, Device characteristics of CZTSSe thin□film solar cells with 12.6% efficiency, *Advanced Energy Materials*, 4, 1-5 (2014).

11. R. R. Prabhakar, N. H.Loc, M. H.Kumar, P. P.Boix, S.Juan, R. A.John, S. K. Batabyal, L. H.Wong, ACS: Applied Materials & Interfaces, Facile Water-based Spray Pyrolysis of Earth-Abundant Cu_2FeSnS_4 Thin Films as an Efficient Counter Electrode in Dye-Sensitized *Solar Cells*, 6, 17661−17667 (2014).
12. G. L. Agawane, S. W. Shin, S. A. Vanalakar, A. V. Moholkar, J. H. Kim, Next generation promising $Cu_2(Zn_xFe_{1-x})SnS_4$ photovoltaic absorber material prepared by pulsed laser deposition technique, *mater. lett.,* 137, 147-149 (2014).
13. Z. Shadrokh, A. Yazdani and H. Eshghi, Solvothermal synthesis of $Cu_2Zn_{1-x}Fe_xSnS_4$ nanoparticles and the influence of annealing conditions on drop-casted thin films, *Semiconductor Science Technology*, 31, 12pp (2016).
14. W. Wang, H. Shen, J. Chen, W. Chen, X. He, Synthesis and properties of $Cu_2(Fe_xZn_{1-x})SnS_4$ nanocrystals by microwave irradiation assisted solvothermal method, *Advanced Powder Technology*, 26, 275-279 (2015).
15. D. B. Khadka and J H. Kim, Structural Transition and Band Gap Tuning of $Cu_2(Zn,Fe)SnS_4$ Chalcogenide for Photovoltaic Application, *The Journal of Physical Chemistry C,* 118, 14227–37 (2014).
16. C. Huang, Y. Chan, F Liu, D. Tang, J. Yang, Y. Lai, J. Li, Y. Liu, Synthesis and characterization of multicomponent $Cu_2(Fe_xZn_{1-x})SnS_4$ nanocrystals with tunable band gap and structure*, J. Mater. Chem. A,* 1, 5402–5407 (2013).
17. M. Adelifard, Preparation and characterization of Cu2FeSnS4quaternarysemiconductor thin films via the spray pyrolysis technique for photovoltaic applications, J. Anal. Appl. Pyrol. (2016), http://dx.doi.org/10.1016/j.jaap.2016.09.022.
18. S. G. Nilange, N. M. Patil, A. A. Yadav, Growth and characterization of spray deposited quaternary Cu2FeSnS4 semiconductor thin films, *Physica B: Physics of Condensed Matter,* (2019) https://doi.org/10.1016/j.physb.2019.02.008.
19. S.A. Khalate, R.S. Kate, J.H. Kim, S.M. Pawar, R.J. Deokate, Effect of deposition temperature on the properties of Cu2ZnSnS4 (CZTS) thin films, *Superlattices and Microstructures* (2017), doi: 10.1016/j.spmi.2017.02.003.
20. B-T. Jheng, K-M. Huang, S.-F. Chen, M-C. Wu, Effects of substrate temperature on the Cu2ZnSnS4 films deposited by radio-frequency sputtering with single target, *Thin Solid Films* (2014), doi:10.1016/j.tsf.2014.05.053.
21. B.D. Cullity, *Elements of X-ray Diffraction*, 2nd edn., (Addition-Weasley, London, 1978).

Figure and table caption

Fig. 1. XRD patterns of $Cu_2Zn_xFe_{1-x}SnS_4$ (x=0, 0.25, 0.5, 0.75 and 1) thin films grown at various deposition temperature T_s (a) 25°C, (b) 100°C, (c) 150°C and (d) 200°C.
Fig. 2. AFM topography of $Cu_2Zn_xFe_{1-x}SnS_4$ (x=0 ; 0.25; 0.5; 0.75 ; 1) thin films grown at various deposition temperatures.
Table 1. EDS results of elemental concentration for $Cu_2Zn_xFe_{1-x}SnS_4$ (x=0 ; 0.25 ; 0.5 ; 0.75 ; 1) thin films grown at various deposition temperature T_s (a) 25°C, (b) 100°C, (c) 150°C and (d) 200°C.
Table 2. Crystallite size for as-deposited $Cu_2Zn_xFe_{1-x}SnS_4$ (x=0 ; 0.25 ; 0.5 ; 0.75 ; 1) thin films.
Table 3. Strain for as-deposited $Cu_2Zn_xFe_{1-x}SnS_4$ (x=0 ; 0.25 ; 0.5 ; 0.75 ; 1) thin films.
Table 4. Roughness for as-deposited $Cu_2Zn_xFe_{1-x}SnS_4$ (x=0 ; 0.25 ; 0.5 ; 0.75 ; 1) thin films.

Effect of additions on thermal stability of hydroxyapatite

Authors: F. Z. Mezahi[1*], F. Zouizi[1], A. Harabi[2]

Affiliations:
[1] *Physics department, University of M'Sila, M'Sila. Algeria*
[2] *Physics department. University of Constantine, Constantine. Algeria*

*Corresponding author: *fatimazohra.mezahi@univ-msila.dz*

One Sentence Summary: The addition of 5% wt. diopside, doloma and silica to hydroxyapatite, when heated at 1300°C, influences effectively the thermal stability and the density of hydroxyapatite.

Abstract: Several works have been carried out on structural modifications and mechanical properties of Hydroxyapatite (HA: $Ca_{10}(PO_4)_6(OH)_2$) in the presence of oxides or metallic dispersions used as reinforcing agents. So, this work is devoted study the thermal stability of pure hydroxyapatite and doped hydroxyapatite (HA + 5% wt. diopside, HA + 5% wt. doloma and HA + 5% wt. silica) when they heated at 1300°C.
The results show that the density of pure treated hydroxyapatite was near to theoretical density. It was observed that a weak decrease was occurred in density value when the doloma was added. Or, the addition of silica and diopside has a remarkable effect on the density of hydroxyapatite.

After heat treatment at 1300°C, the XRD results show that the composition of pure hydroxyapatite has not changed. However, the addition of the doloma led to the partial decomposition of HA into b-tricalcium phosphate (b-TCP) as minor phase. While the addition of the diopside and silica leads to the formation of silicate hydroxyapatite "the silicocarnotite" as major phase. The FTIR results confirmed the XRD results. The IR characteristic bands of (b-TCP) and the silicocarnotite were well distingued.

Introduction

Hydroxyapatite (HA: Ca10(PO4)6(OH)2) (HA) is one of the most attractive materials for human hard tissue implants because of its close physical and chemical properties to mineral part of bone and teeth (1). For full utilization of bioactive HA-based implants, improvements in their mechanical properties are well recommended. Several works have consequently been carried out on structural modifications and mechanical properties of HA in the presence of oxides or metallic dispersions used as reinforcing agents (2-4). The densification, grain and pore size could potentially alter the mechanical properties of HA (5). So, the aim of this work is to study the effect of doping elements (5% wt. doloma (DM) or diopside (DP) or silica (SI)) on density and thermal stability of HA.

Results

Subhead 1: Preparation of HA

HA was prepared by calcination of cortical bovine bone at 800°C for 1 h.

Subhead 2: Experimental conditions of sintering

The pure HA and doped HA (*HA* + 5% wt. DM (or DP or SI) powders wet milled for 4 h, dried, compacted at 75 MPa and sintered at 1300°C for 2 h.

Subhead 3: Density results

The density values of pure and doped HA, after heat treatment at 1300°C, decreased mostly for HA doped by diopside and silica (Table 1).

Table 1: Density results

	HA	*HA*+ 5% DM	HA + 5% DP	HA + 5% SI
Density value (g/ cm^3)	3,06	3,01	2,85	2,67

Subhead 4: SEM results

SEM micrographs confirm the well densification of HA and (HA+ 5% DM) samples. Or, in (HA + 5% DP or SI) samples, they reveal the presence of large pores. SEM micrographs are in good agreement with density values (Fig.1)

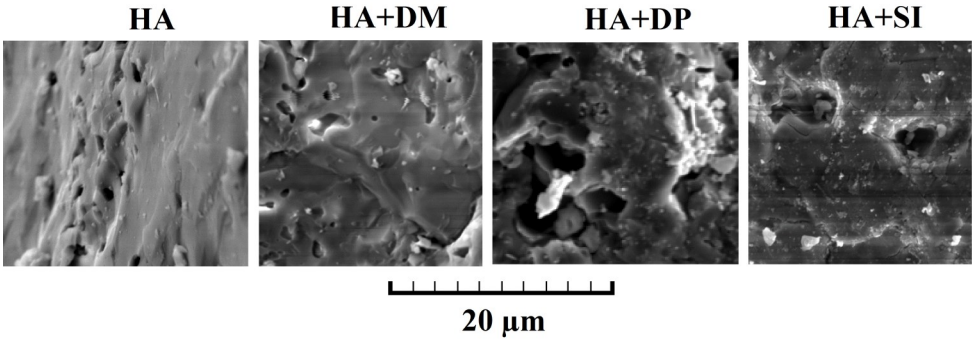

Figure 1: SEM micrographs of pure HA and doped HA samples, treated at 1300°C.

Subhead 5: XRD results

For *HA* + 5% DM, the partial decomposition of HA into b-tricalcium phosphate (b-TCP) was occurred. For (HA + 5% DP or SI), the formation of "silicocarnotite" ($Ca_5(PO_4)_2(SiO_4)$) was remarked (Fig.2).

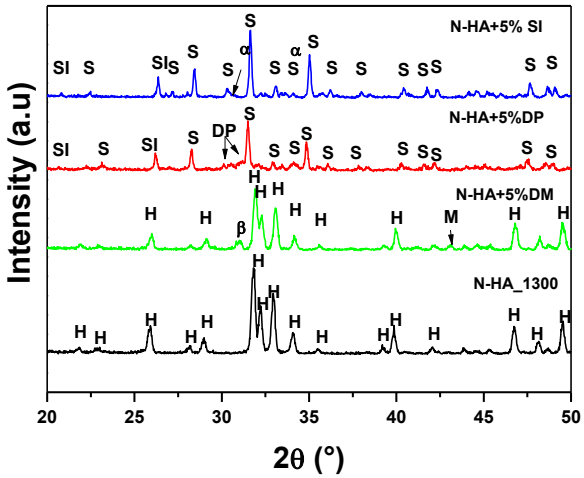

Figure 2: XRD of pure HA and doped HA samples, treated at 1300°C.
H: HA, **β** :(β-TCP), **M**: MgO, **S**: silicocarnotite, **a:** a-TCP.

Subhead 6: FTIR results

FTIR analysis confirm the XRD results; IR characteristic bands of (b-TCP) and the silicocarnotite were well distinguished (Fig.3).

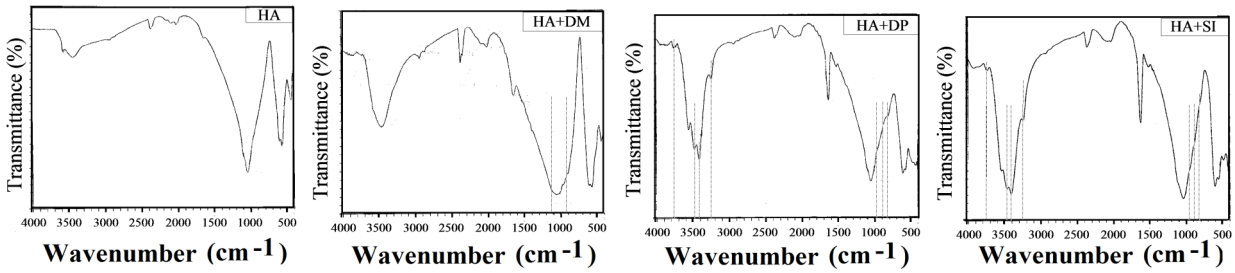

Figure 3: FTIR results of pure HA and doped HA samples, treated at 1300°C.

Discussion

According to XRD results, the addition of all doping elements has altered the HA stability. The addition of doloma (CaO+ MgO) has led to minor decomposition of HA to (b-TCP) which justify the weak decrease of density of HA+ 5% DM samples in comparison of that of pure HA. However, the addition of diopside ($CaMgSi_2O_6$) or silica has led to important decomposition of HA to (b-TCP) and CaO which justify the significant decrease of density of (HA+ 5% DP or SI) samples which were characterized by the presence of large pores. b-TCP was reacted with the added elements, precisely with SiO_2, in order to form a new phase (silicocarnotite). Noted that, the silicocarnotite formation was accompanied with a-TCP formation. R. N. Borşa has demonstrate that silicocarnotite can be formed from the mixture of $Ca_3(PO_4)_2$ or $Ca_2P_2O_7$, SiO_2 or $CaSiO_3$ and $CaCO_3$ as source of Ca (6). The FTIR has confirmed the XRD results by apparition of all bands characteristic of groups presents in appeared phases in XRD patterns.

Materials and Methods

Phase compositions were identified by X-ray diffraction (XRD) (PANalytical XPert PRO) with a CuK_α radiation (λ = 0.154 nm, filter: Ni, voltage = 40 kV and current = 30 mA). The microstructure of samples surfaces was observed using a scanning electron microscope (SEM) (TESCAN VEGA MODEL: TS 5130 MM). The samples have been gold (Au _20 wt% Pd) coated to allow surface conduction, before their observation. Fourier transformed infra-red spectroscopy (FTIR) (Shimadzu FT / IR – 460: 4000-400 cm^{-1}) was used to highlight the structural analysis.

References:

1. L. L. Hench, Bioceramics: From Concept to Clinic, *J. Am. Ceram. Soc.,* **74**, 1487–1510 (1991).
2. Y. Nayak, R. Rana, S. Pratihar, S. Bhattacharyya, Low-Temperature Processing of Dense Hydroxyapatite–Zirconia Composites, *Int. J. Appl. Ceram. Technol.,* **5 [1]**, 29–36 (2008).
3. J. Huaxia and P. M. Marquis, Sintering Behaviour of Hydroxyapatite With 20wt% of Al2O3, *J. Mater. Sci.*, **28**, 1941–1945 (1993).
4. Y. M. Kong, S. Kim, H. E. Kim, Reinforcement of Hydroxyapatite Bioceramic by Addition of ZrO_2 Coated with Al_2O_3, *J. Am. Ceram. Soc*., **82 [11]**, 2963–2968 (1999).
5. G. Goller, F. N. Oktar, Sintering Effects on Mechanical Properties of Biologically Derived Dentine Hydroxyapatite, *Mater. Lett.*, **56**, 142–147 (2002).
6. R. N. Borşa, Doctorat thesis : Elaboration de poudres et de dépôts de phosphates de calcium silicatés à usage de Biomatériaux, Toulouse (2008).

Study by Molecular Docking of the Inhibition of Linoleic Acid by Lipoxygenase

Autors: R. Djemil[a,*], S. Nigri[b], N. Lachi[a], M. Cheriet[c], H. Rahmoni[c], D.E. Khatmi[d]
Affiliations:
Department of Material Sciences
[a]*Laboratory of Computational Chemistry and Nanomaterials (LCCN),*
[b] *Laboratory of Industrial Analysis and Materials Engineering (LAIGM),*
[c]*Laboratory of Applied Chemistry (LCA)*
[d]*Institute of Molecular Sciences ISM2 Marseille. France*
University 8 May 1945 Guelma

*****Corresponding author: *messdjem@gmail.com*

Abstract: In this work, we studied the inhibition of lipoxygenase (LOX), the enzyme that catalyzes the oxidation reaction of linoleic acid (LA) by Molecular Docking. This process of inhibition of LOX has been realized by natural antioxidants such as tocopherols and polyphenols.
The results obtained showed that tocopherols have higher affinities than linoleic acid and present better inhibitory activity than polyphenols. Indeed, α-tocopherol forms the most stable protein-ligand complex. This stability is assured by the formation of two H bonds. The first is formed between the H of the amine group of GLY412 and O of the hydroxyl group of the ligand. The second between O of carbonyl group of the acid function of GLU99. The GLU99 and GLY412 residues that participated in the formation of the LOX-AL complex were blocked by the presence of tocopherols.
Keywords: *Molecular Docking, LOX, Inhibition, Antioxidants.*

Introduction:
The interactions between protein-protein and protein-ligand are at the basis of biological mechanisms. Understand its operating modes and define which are residues involved, are therefore essential to explain the mechanisms that affect the affinity between two molecules. Similarly, the discovery of new molecules that activate or inhibit the biological activity of a protein can only be done by predicting their affinity respectively. It is in this goal that molecular modeling techniques, grouped under the name "docking" molecular were developed [1,2].
Molecular Docking presents one of the most used theoretical approaches. It aims to predict possible modes of interactions of the structure of a ligand-protein complex. Which is considerably easier to implement, cheaper and faster than using experimental methods (RX, RMN …etc.). [3].
Lipoxygenases (LOXs) are very common enzymes in both the animal and plant kingdoms. LOXs are responsible for the aroma of many plant products such as olive oil. They are involved in the catalysis of polyunsaturated fatty acids according to a complex mechanism known as the LOX pathway. [4, 5]

Computational method:
In this study, we used the Surflex program implemented in SYBYL-X version 2.1.1.[6]. The structure of linoleic acid is extracted from the PUBCHEM database. Then it is optimized by the gasteiger huckel method with the steepest descent algorithm and the tripos force field. Lipoxygenase (lox), making subject of our study, has been downloaded from the Protein Data Bank (PDB). Before docking the metal bonds and water molecules are removed, then the protein is optimized using the MMFF94 force field.

Results and discussion:
The inhibition of LOX by various molecules has been the subject of this work whose main purpose is a better comprehension of this phenomenon. In this work, we focused on the study of natural inhibitors such as tocopherols. and polyphenols. [7-10].

Molecular Docking of LOX -tocopherols complexes (α-, β-, δ- and γ-tocopherols) provided the modes of interaction present two hydrogen bonds: The first one is established between H of amine group of GLY412 and O of hydroxyl group of the ligand. The second is formed between O of the carbonyl group of the acid function of GLU99 and H of the hydroxyl group of the ligand with variable binding lengths. The residues GLU99 and GLY412 that participated in the formation of the LOX-linoleic acid complex were blocked by the presence of tocopherols

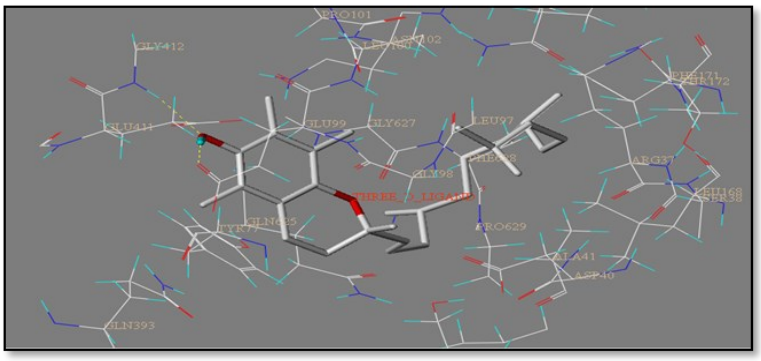

Figure : Interaction mode of LOX- α-tocophérol.

Affinities of ligands:

This procedure is based on docking of linoleic acid and all inhibitors to be able to classify them in descending order of affinity. The results of Docking are presented in the table below.

Table : Classifying of Docking Results.

Classifying	Structure	Total score
1	α-tocopherol	10.4385
2	β-tocopherol	9.8174
3	δ-tocopherol	9.6029
4	γ-tocopherol	9.0898
5	alpha-tocopheryl acetate.	9.0581
6	linoleic acid	8.3530
7	hydrohytyrosol	7.3395
8	2-Phenyl-4-chromanol	7.3023
9	(-)-epigallocatechin gallate	4.2713

Docking results show that tocopherols have higher affinities than linoleic acid. These latter present a better inhibitory activity than polyphenols. The α-Tocopherol forms the most stable protein-ligand complex. It therefore presents a better inhibitory effect. (-) - epigallocatechin gallate present the lowest affinity for LOX among the range of inhibitors studied and therefore it forms the least stable complex.

Conclusion:

This work focused on molecular modeling by Docking using SYBYL software. Its essential purpose is to study theoretically the inhibition of the lipoxygenase enzyme which catalyzes the reaction of the oxidation of linoleic acid by natural antioxidants such as tocopherols and polyphenols. The results show that tocopherols have higher affinities than linoleic acid. These tocopherols have a better inhibitory activity than polyphenols. The α-Tocopherol forms the most stable protein-ligand complex. This stability is ensured by the formation of two interactions of the hydrogen bonding type between the ligand and the GLY412 and GLU99 residues. These latter who participated in the formation of the LOX-linoleic acid complex were blocked by the presence of tocopherols.

References:

1. Levinthal. C., Wodak . S.J., Kahn. P., Dadivanian. A.K. *Proceedings of the National Academy of Sciences of the United States*.72, 1330–34 (1975)
2. Kuntz. I.D., Blaney. J.M., Oatley. S.J., Langridge. R., Ferrin. T.E. *Journal of Molecular Biology*. 161. 269–88 (1982).
3. Arjani A.T. E. and Mekelleche S.D., *J. Theo.Comp.Chem*. 16, 1750001-1 (2017),.
4. Gargouri. M., Ben Akacha.N., Kotti. F., Ben Rejeb. I. *Biotechnologie, Agronomie, Société et Environnement.* 12, 185-202 (2008)
5. Braidot. E., Micolini. S., Risso. A., Macri. F., Vianello. A. *Plant Science*. 164, 9-16. (2003).
6. Jain, A.N. *J. Computer-Aided Molecular Design*. 21, 281-306(2007).
7. Ito. N., Fukushima S., Hagiwara A., M. Shibata, T. *Journal of the National Cancer Institute* 70, 343-352(1983).
8. Chen C., Pearson A.M., Gray J.I., *Food of Chemistry*. 43, 177-183 (1992).
9. Dionisi. F., Prodollit. J., Tagliaferri. E. *Journal of the American Oil Chemists' Society*. 72, 1505-1511(1995).
10. Japon-Lujan R., Janeiro P., Luque de Castro M.D. *Journal of Agricultural and Food Chemistry*. 56. 7231–7235 (2008).,

Corrosion inhibition of copper in 1M HNO_3 solution by oleic acid: weight loss, electrochemical methods and quantum chemical calculations

Autors: Soraya Nigri[a]*, Rayenne. Djemil[b], Boulanouar. Messaoudi[c], Rabah. Oumeddour[a]

Affiliations:
[a]*Laboratory of Industrial analysis and Materials Engineering. Department of material sciences*
[b]*Laboratory of computational chemistry and nanostructures, University May 8, 1945, Po. Box 401, Guelma, 24000, Algeria.*
[c]*Laboratory of Applied Thermodynamics and Molecular Modeling, Department of Chemistry, University of Tlemcen, PB 119, Tlemcen, 13000, Algeria*

**Corresponding author: nigri_s@yahoo.fr; nigri.soraya@univ-guelma.dz*

Abstract: The inhibition of the corrosion of copper in 1 M HNO_3 solution by oleic acid was investigated by weight loss measurement, potentiodynamic polarization and scanning electron microscope (SEM) studies. The experimental results have showed that this compound revealed a good corrosion inhibition and the inhibition efficiency is increased with the inhibitor concentration to reach 98%. The results obtained revealed that the adsorption of the inhibitor molecule onto metal surface is found to obey Langmuir adsorption isotherm. The temperature effect on the corrosion behavior of copper in 1 M HNO_3 without and with inhibitor at different concentration was studied in the temperature range from 303 to 333 K and the kinetic parameters activation such as Ea, ΔHa and ΔSa were evaluated.Tafel plot analysis revealed that oleic acid acts as a mixed type inhibitor. SEM analysis substantiated the formation of protective layer over the copper surface. Computational studies have been used to find the most stable adsorption sites for oleic acid on cooper surface. The obtained experimental results were in good agreement with the theoretical results.

Introduction

The protection of metals by organic corrosion inhibitors is based mainly on the adsorption of these compounds on a metal surface and the formation of protective layers. Adsorption can occur via electrostatic interaction (physisorption), or it can involve charge sharing between the surface and corrosion inhibitor (chemisorption), or combination of both interaction types can take place (1). The chemical structure is an important factor in the choice of corrosion inhibitors or in the development of new ones. The adsorption of the organic inhibitors mainly depends on some physicochemical properties of the molecule to the possible steric effects and electronic density of donor atoms; adsorption is suppose also to depend on the possible interaction of p-orbitals of the inhibitor with d-orbitals of the surface atoms (3). However, most of the available inhibitors do not fulfill completely the requirements imposed by the environmental protection standards. Nowadays**,** natural products from plant are nontoxic and biodegradable have been reported in several studies as green effective inhibitors of metal corrosion in different aggressive environments (4,5). The aim of this study is to explore the use of oleic acid in the ambition of using vegetable oils or biomass extracts rich on this fatty acid as green corrosion inhibitors in future. The corrosion inhibition efficiency has been experimentally evaluated for copper surface in HNO_3 solution using weight loss and potentiodynamic polarization techniques as well as the thermodynamic parameters for the adsorption process and activation parameters for the copper dissolution reactions are calculated and discussed. Computational studies have been used to find the most stable adsorption sites for oleic acid on cooper surface.

Materials and Methods

The copper specimens of 99% purity used for this study was provided in rectangular form of 1×2 cm^2 surface. Weight loss measurements were recorded in a thermostated water bath in 1 M HNO_3 solution with and without addition of different concentrations of inhibitor for various intervals of time at 30–60 °C.

Potentiodynamic polarization curves were recorded by use of a 273A EG&G PAR potentiostat combined with "Power suite software", the scan rate was 50 mV/s. The potential ranged from – 450 to + 450 mV/Ag/AgCl. Electrochemical measurements were performed with a conventional three-electrode electrochemical cell (with thermostat) consisting of platinum electrode as auxiliary electrode, a silver/silver chloride electrode (Ag/AgCl) as reference, and Cu metal as

Results and Discussion

The inhibitor was tested for four different concentrations for 3h. The corrosion rate markedly decreased and inhibition efficiency increased with increasing the concentration of the inhibitor. At the inhibitor concentration of 0.6 $^{0}/_{00}$ V/V, the maximum EI% obtained was 98%, which shows that AO possesses important corrosion inhibitor properties for copper in HNO_3.

To clarify the nature of adsorption and the surface behavior of inhibitor molecules, various adsorption isotherms were tested for the evaluation of different adsorption isotherms. The fit for Langmuir isotherm offers an excellent model with R^2 of 0.998.

Polarization measurements were carried out in order to gain knowledge regarding the kinetics of the cathodic and anodic reactions and to know how inhibitory effect acted. The polarization curves obtained for copper in the absence and presence of oleic acid at optimum concentration are shown in Figure 1.

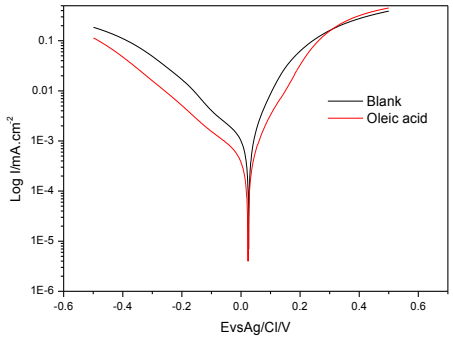

Figure 1. Potentiodynamic polarization curves for copper in1 M HNO_3 without and with oleic acid

Inspection of the Tafel curves reveals that corrosion current densities are significantly reduced in the presence of inhibitors. It is also observed that the addition of tested inhibitor retards both cathodic and anodic reactions; however, the cathodic reactions are comparatively more affected than the anodic ones suggesting that the investigated inhibitors are mixed type inhibitors and predominantly act as cathodic inhibitors. The obtained results from Tafel polarization showed a good agreement with the Weight loss measurements ones.

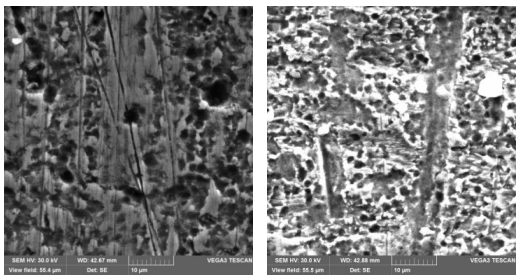

Figure 2: SEM micrograph of the metal specimens in absence and the presence of the oleic acid

The resulting of the high resolution SEM micrograph shows that the surface was strongly damaged in the absence of inhibitor due to rapid corrosion attack. However, a relatively smoother and less corroded morphology of metal surface can be observed in the micrographs in the presence of oleic acid (figure 2).
Quantum chemical approach, using the density functional theory (DFT), was used in order to get a better understanding of the relationship between the tested inhibitor inhibition efficiency and molecular structure. The calculated quantum chemical parameters include: the energies of highest occupied molecular orbital (E_{HOMO}) and lowest unoccupied molecular orbital E_{LUMO}). The local reactivity has been analyzed through Fukui and local softness indices, to compare possible sites for nucleophilic and electrophilic attacks. The optimized structure, E_{HOMO} and E_{LUMO}, of oleic acid is shown in figure 3. For OA, using MK analysis, C17 site is either a nucleophilic or electrophilic centre, and may share the same opportunity with C16 to be a nucleophilic center, but when talking about electrophilic centers, C20 site is more electrophilic than C17, to receive the nucleophilic attack.

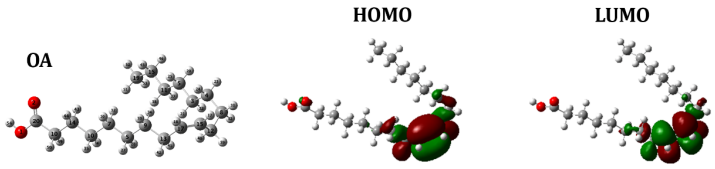

Figure 3. The optimized structure, HOMO and LUMO distribution for OA
[Atom legend: white = H; Gray = C; red = O].

Conclusion

The inhibition effect of oleic acid on the corrosion behavior of cooper in a 1 M HNO_3 solution, was studied by weight loss, electrochemical methods and quantum chemical calculations. The potentiodynamic polarization curves indicate that these inhibitors act as a mixed type inhibitor, with more polarized cathodic than anodic curves. The adsorption of OA on the metal surface followed Langmuir adsorption isotherm. The calculations of the tested inhibitors reactivity indices are an accurate tool for interpreting the electron transfer mechanism between inhibitors' molecules and the cooper. The obtained experimental results were in good agreement with the theoretical results.

References

1. G. Gece, B. Semra, *Corros. Sci.* **52**, 3435-3443 (2010).
2. S. Ramesh Kumar, I. Danaee, M. Rashvand Avei, M. Vijayan, *J. Mol. Liq.* (**212**), 168–186 (2015)
3. M.G. Fontana, K.W. Staehle, *Advances in Corrosion Science and Technology*, vol. 1. New York, Plenum Press; (1970)
4. K. Boumhara, M. Tabyaoui, C. Jama, F. Bentiss, *J. Ind. Eng. Chem*. **29,** 146-155 (2015).
5. K.K. Anupama, K. Ramya, Abraham Joseph, *J. Mol. Liq.* **216**, 146–155 (2016).

Comparative Study of the adsorption of CuPc on surfaces hydrogenated Si (111)-H by atomic and chemical methods using LEED, XPS, XPD and UPS techniques

Autors: I. Arbi*, A. Akremi, C. Chefi

Affiliations:
Université de Carthage, Laboratoire de Physique des Matériaux, Unité de Service Commun Spectromètre de Surfaces, Faculté des Sciences de Bizerte,Jarzouna, 7021 Bizerte, Tunisia
**Corresponding author: inesarbi84@gmail.com*

Summary:
The study of the different methods before and after deposit molecules CuPc on the surfaces Si(111) reveals that :
Chemical method complete passivation of the surface, a good self-assembly molecules CuPc with horizontal configuration.
Atomic method has both saturation and destruction character: Presence of surface defects and the stacking of CuPc molecules with configuration initial vertical according to the structure of phase α.

Abstract:
The aim of this study is to present the differences between two hydrogenation methods: the ex-situ chemical hydrogenation method and the in-situ atomic hydrogenation method. As the two hydrogenation procedures are different, the adsorption of the CuPc molecules on such surfaces is generally affected. In the sections that follow, the main differences in the resultswill be analysed and discussed. The substrate parameters, the surface morphology, the hydrogenation procedure and the self-assembly of the CuPc molecules on these surfaces will be the key parameters of these differences.

Keywords: Copper phthalocyanine, Hydrogen passivated silicon surface, Molecule adsorption, XPD, XPS, LEED, UPS.

Introduction

In order to study the mechanisms of molecular interaction on surfaces, appropriate study strategies must be put in place. The choice of the surface on which the molecule will be adsorbed is also important. It is essential that the surfaces used allow the molecule-molecule interactions not to be completely masked by the interactions between the substrate and the molecule. It is for this reason that metal surfaces have often been used because the interactions between the surface and the molecule are generally weak.

Results

The results by LEED

The LEED results show that the both types of hydrogenation lead to the same 1×1 reconstruction. However, the in-situ atomic method induces more morphological defects.
The study of the adsorption CuPc molecules on the ex-situ chemically hydrogenated Si (111) surface shows an ordered adsorption for low doses (1ML to 3ML). The persistence of the 1×1 diffraction pattern up to 3ML shows that the growth mode is Volmer Weber.

The results by XPS

The decomposition of the peaks of core levels relative to the CuPc molecule (C1s, Cu2p, N1s) by CASA-XPS program presents the same number of (Gaussian) components for each of the peaks relative to the two types of silicon substrates hydrogenated by chemical and atomic methods.
The results obtained by XPD reveal in the case of the chemically prepared surface, the interaction of the molecules for a dose of 1ML is of the molecule-substrate type.
Whereas, the atomically hydrogenated surface method shows the interaction of the molecules for a dose of 1ML is of the molecule-molecule type.

The results by XPD

XPD analysis during the growth of the CuPc molecules shows a flat arrangement of the CuPc molecules on the chemically hydrogenated silicon surface,whereas the configuration is vertical "standing" in the case of atomic hydrogenation.

The results by UPS

The UPS results reveals that the work function undergoes a decrease during the growth of the CuPc molecules on the differently prepared silicon surfaces. It reaches a value of 3.9 eV at
20 ML of CuPc for the chemically hydrogenated substrate and 3.56 eV at 20 ML of CuPc for the atomically hydrogenated substrate. We also evaluated the ID interface dipole magnitude for both types of hydrogenated silicon substrates. In the case of chemical hydrogenation, ID is 0.35 eV whereas in the case of atomic hydrogenation, it is 0.44 eV [3].
A band binding of 0.5 eV relative to the molecular orbitals is deduced and attributed to the rearrangement of the molecules during adsorption.

Figures and Tables:

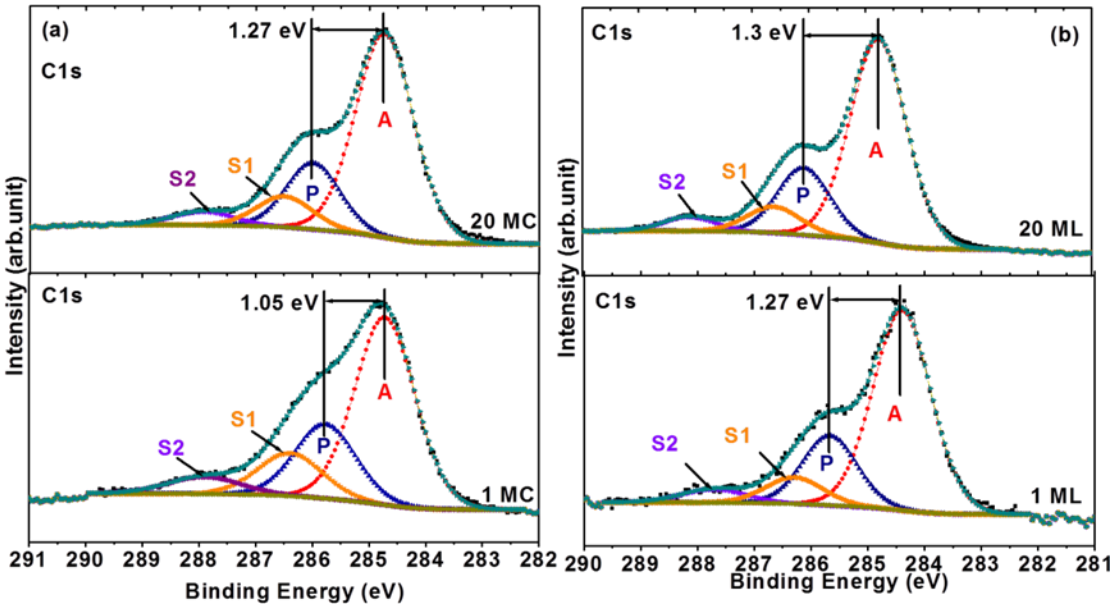

Fig.1- Decomposition of the XPS peaks of the C1s core level recorded at 1 ML and at 20 ML of CuPc on the hydrogenated surface by (a) chemical method, (b) atomic method.

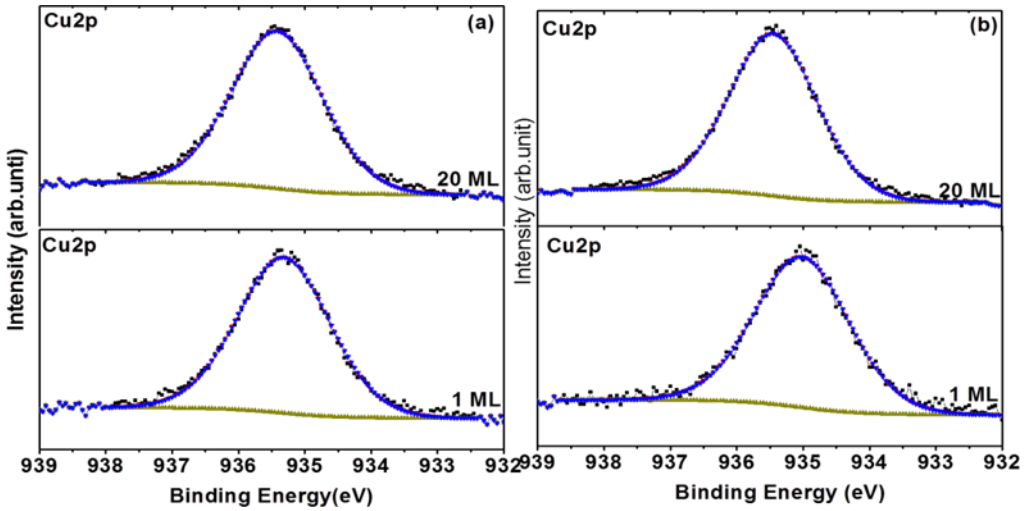

Fig.2- Decomposition of the XPS peaks of the Cu2p3 / 2 core level recorded at 1 ML and 20 ML of CuPc on the hydrogenated surface by: (a) chemical method, (b) atomic method.

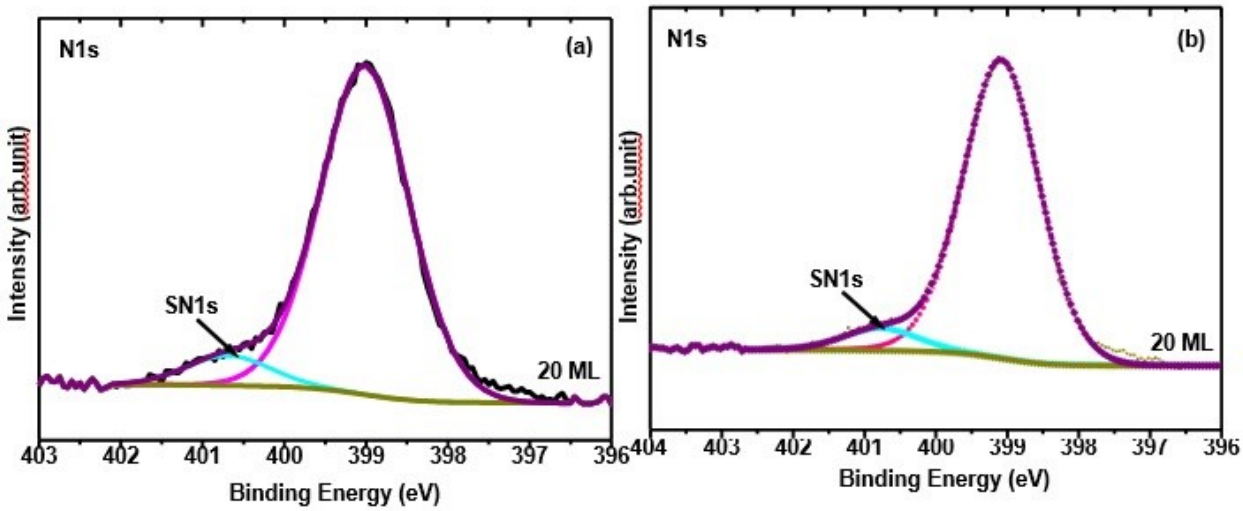

Fig.3- Decomposition of the XPS peaks of the core level N1s recorded at 20 ML of CuPc on the hydrogenated surface by: (a) chemical method, (b) atomic method.

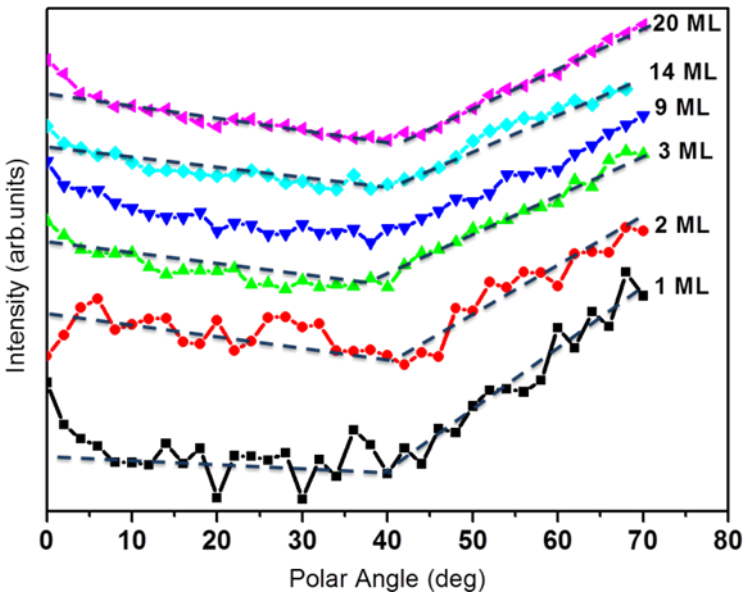

Fig.4- Polar angle intensity scans from the Cu 2p3/2 peak for CuPc / Si (111) –H

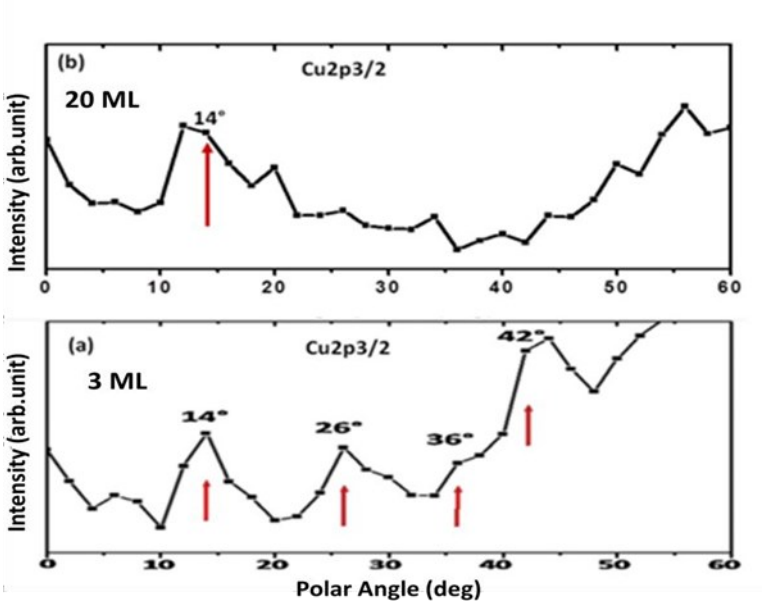

Fig.5- XPD spectra for Cu2p3 / 2 obtained at (a) 3ML [3] and (b) 20 ML on the Si (111) 1 × 1-H atomically hydrogenated surface.

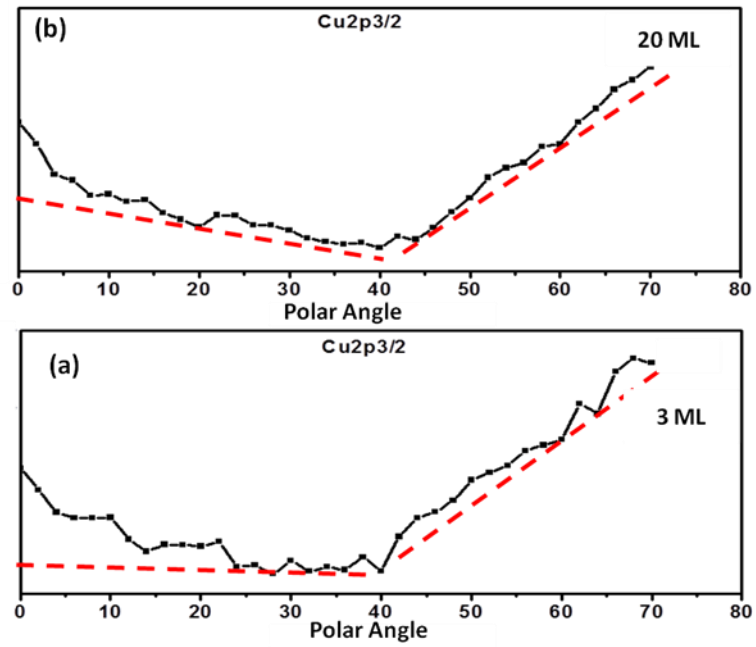

Fig.6- XPD spectra for Cu2p3 / 2 obtained at (a) 3ML and (b) 20 ML of CuPc on the chemical hydrogenated Si (111) 1 × 1 -H surface.

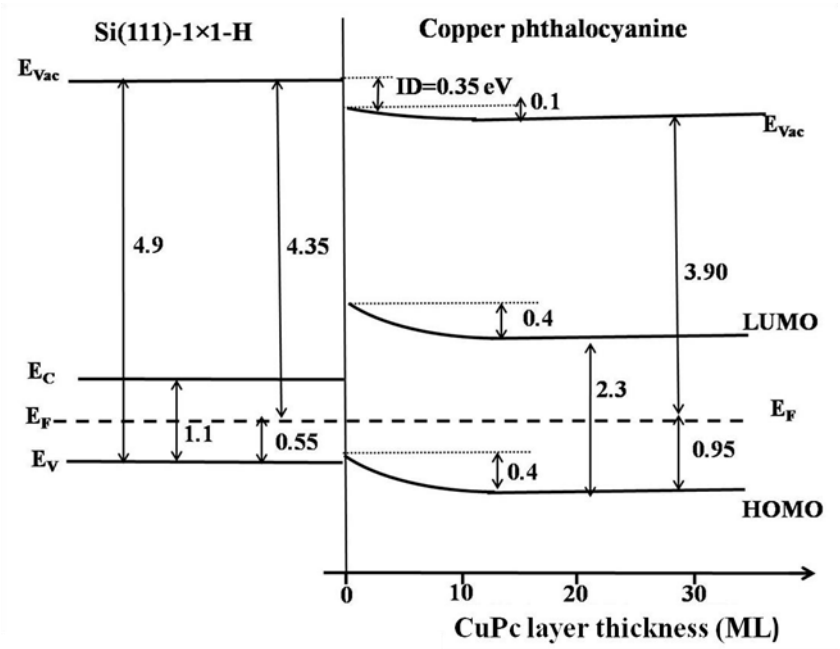

Fig.7- Energy diagram of the CuPc / Si (111) 1 × 1-H interface: chemically hydrogenated substrate.

T (°C)	1600	1750	1950
dose (L) η	0,012	0,043	0,12
100	3,2	11,6	32,4
200	2,1	7,7	21,6
400	4,2	15,4	43,2
600	6,3	23,1	64,8
800	8,6	30,9	86,4
1000	32	116	324

Fig.8 Atomic hydrogen flux values (in 1014 atoms) calculated as a function of the temperature of the W filament and the dose of molecular hydrogen sent to the filament in the geometry of the experiment.

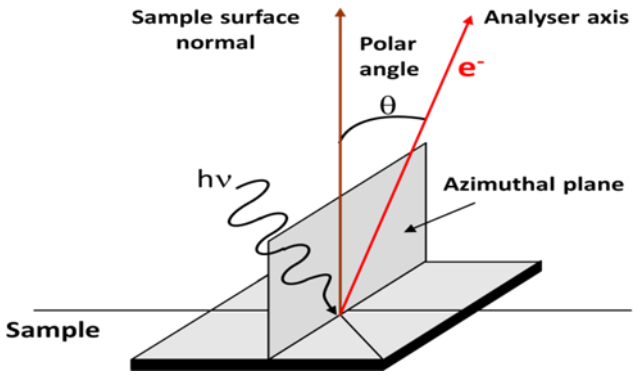

Fig. S1. Schematics of the experimental geometry for XPD measurements

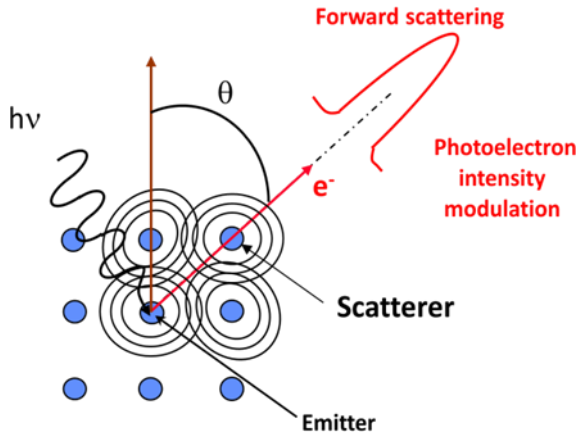

Fig. S2. Principle of recording an XPD spectrum.

Equations:

Atomic hydrogen flux values

$$\Phi = 0{,}9\ 1014\ \eta\ dose\ (L)$$

η is the coefficient of proportionality [13], involving the probability of dissociation of H2 in contact with hot tungsten.

The ratio of peaks of surfaces calculated by CASAXPS:

$$(A + S1)/(p + S2)\ or\ A/P$$

The work function:

$$\varphi = hv - (EF - Ecutoff)$$

φ ***: The work function.***

hv: The energy of incident photons (21.2 eV).
Ecutoff: The high-energycut-off of the UPS spectra.

The ionization energy:

$$IE = hv - (EV - Ecutoff)$$

IE: The ionization energy.

EV: the top of the valence band for inorganic semiconductors.

The interface dipole:

$$ID = \Delta\varphi - Vb$$

$\Delta\varphi$***: The total work function. Vb: The total band bending.***

Discussion

After deposit molecules of CuPc, The decomposition of C1s reveals an energy shift between each main peak and its satellite by a value of approximately 1.9 eV (Fig.1). This result is in good agreement with that found between the highest occupied molecular state (HOMO) and the low unoccupied molecular state (LUMO) **[4].**

The result obtained by chemical method is similar to that obtained by Sumona Sinha et al **[5]** in the study of adsorption of CuPc molecules on the Copper substrate.

The satellite peaks obtained by the decomposition of Cu2p core level peak clearly visible in Fig.2, are comparable to those found by D. G. de Oteyza et al **[6]** during the adsorption of CuPc molecules on the Au substrate (100).
The studies of the peaks associated with the atoms (NM) and (Np) are separated from 0.3 eV. It is a very low value compared to our energy resolution and is also accompanied by two Sp and SM satellites **[7]**.

The results for N1s are in good agreement with other studies **[8, 9]** carried out on CuPc. This results show that the N1s spectrum has two N1 and N2 bands centered at 398.9 eV and 400.6 eV and which are associated with the presence of binding C-N.

Deposition method of molecules CuPc: The organic material, CuPc (purity 97%), purified by two cycles of sublimation was deposited in situ from a Knudsen cell (heated to about 270°C) or the substrate is maintained at room temperature. The flow (about 0.1 monolayer (ML) per minute) was determined using a thickness monitor of quartz crystal water cooled (STM-100 by Sycon) equipped with an OSC-100A Sycon oscillator.

References and Notes:

1. S. Watanabe, Surf. Sci. 415 (1998) 385.

2. Y. Caudano, P.A. T hiry, Y.J. Chabal, Surface Science 502-503 (2002) 91-95.

3. I. Arbi, B. Ben Hamada, A. Souissi, S. Menzli, C. Ben Azzouz, A. Laribi, A. Akremi,

4. C. chefi, Applied Surface Science 305 (2014) 396–401.

5. A. Ruocco, F. Evangelista, M.P. Donzello, G. Stefani, Phys. Rev. B 67 (2003) 155408. [5]

6. Sumona Sinha, M. Mukherjee, Applied Surface Science 353 (2015)540–547.

7. D. G. de Oteyza, A. El-Sayed, J. M. Garcia-Lastra, E. Goiri,1 T. N. Krauss, A. Turak, E. Barrena, H. Dosch, J. Zegenhagen,8 A. Rubio,4 Y. Wakayama, J. E. Ortega, journal of chemical physics 133 (2010) 214703.

8. Francisc Haidu, Thèse de(Technische Universität Chemnitz) “Tailoring the Electronic and Optical Properties of Molecular Thin Films by Reducing and Oxidising Agents”, 2014.

9. T. Ujvári, A. Kolitsch, A. Tóth, M. Mohai and I. Bertóti, Diamond and Related Materials 11 (2002) 1149–1152.

10. G. Beamson, D. Briggs, High Resolution XPS of Organic Polymers The Scienta ESCA300 Database, Wiley, Chichester, (1992).

11. S. Menzli, B. Ben Hamada, I. Arbi, A. Souissi, A. Laribi, A. Akremi, C. Chefi, Applied Surface Science 369 (2016) 43–49.

12. J. N. Smith and W. L. Fite, J. Chem. Phys. 37 (1962) 898.

Acknowledgments:

We are very grateful to our colleagues of surface research unity at Faculty of Sciences of Bizerte for their useful discussions and their invaluable support.

Investigation of the effects of PVP stabilizer ratio on the structural and optical properties of dip-coated silver nanoparticles/zinc oxide nanocomposites thin films

Autors: L. Ouarez[a], A. Chelouche[a*], D. Djouadi[a], S. Ouhenia[b], A. H. Souici[b], A. Touam[c,d]

Affiliations:
[a]*Laboratoire de Génie de l'Environnement, Faculté de Technologie, Université de Bejaia, 06000 Bejaia, Algeria*
[b]*Laboratoire de Physico-Chimie des Matériaux et Catalyse, Faculté des Sciences Exactes, Université de Bejaia 06000 Bejaia, Algéria*
[c]*Laboratoire des Semi-conducteurs, Université Badji Mokhtar-Annaba, BP 12, Annaba 23000, Algeria*
[d]*Unité de Recherche en Optique et Photonique, UROP – CDTA, Université Ferhat Abbas, Sétif 1, 19000 Sétif, Algeria*
*Corresponding author: *azeddinechelouche@gmail.com*

One Sentence Summary: The PVP stabilizer ratio affects both size of Ag nanoparticles and crystal quality, c-axis orientation, optical transmittance and photoluminescence properties of Ag/ZnO nanocomposites thin films.

Abstract: In this work, ZnO-Ag nanocomposites thin films have been deposited on glass substrates using Dip-Coating technique. ZnO thin films and Ag nanoparticles have been prepared by sol-gel and Polyol process, respectively. The effects of PVP stabilizer ratio (0.1-0.4 M) on the structural and optical properties of ZnO-Ag nanocomposites thin films have been studied using various characterization techniques. X-ray diffraction analysis results indicate that all samples exhibit the hexagonal Wurtzite structure with a high c-axis preferential orientation in addition to the presence of a weak peak related to the cubic Ag phase. The intensity of the (002) diffraction peak increases with increasing PVP ratio. The UV–visible absorption spectra of Ag colloidal nanoparticles have demonstrated that the increase of the PVP ratio leads to the red shift of the absorption peaks from 423 nm to 436 nm. The optical transmittance analyses have revealed the increase of the transparency of the ZnO-Ag thin films with increasing PVP amounts. Room temperature photoluminescence (PL) of ZnO-Ag films have demonstrated that all nanocmposites present a sharp and high UV emission at 389 nm and a very weak and large visible one. The intensity of the UV emission is enhanced with increasing PVP concentration.

Introduction

Zinc oxide (ZnO)-noble metal nanocomposites (NCs) have been widely studied due to their promising applicability in divers fields such as plasmonic (1, 2), photo-catalysis (3, 4) and gas sensors (5). They present exceptional properties and functionalities which cannot be achieved by using noble metals nanoparticle or juste ZnO semiconductor. ZnO is very interesting owing to its wide band gap ~ 3.37 eV, large exciton binding energy (60 meV), high activity, low cost, high stability, nontoxicity, and chemical inertness (6). However, Ag nanoparticles (NPs) exhibit interesting plasmonic properties when exited with specific wavelength. Their absorption and scattering can be tailored by controlling their size and shape (7). Recently extensive research is conducted in order to improve the properties of Ag-ZnO nanocomposites for specific applications by using many techniques and strategies (1, 5). For example, Venugopa et al. (8) studied the structural, morphological, and optical properties of transparent conductive ZnO/Ag/ZnO multilayer films prepared using Ultrasonic spray pyrolysis and thermal evaporation technique. Sun et al. (4) investigated the photocatalytic of Ag/ZnO nanocomposite synthesized via a facile sol-gel method. Singh et al. (2) studied the effect of annealing temperature on the formation of silver (Ag) nanoparticles in a ZnO matrix synthesized by RF magnetron sputtering.
In this paper, we presented some preliminary results of our study regarding structural, optical and photoluminescence properties of multilayer ZnO-Ag NPs deposited on glass substrate.

Experimental procedure

The ZnO thin films were prepared by the sol-gel dip-coating route reported elsewhere (9, 10). Zinc acetate dehydrate ($Zn(CH_3COO, 2H_2O)$ (Sigma Aldrich) was dissolved in a mixture of absolute ethanol and monoethanolamine (MEA, C_2H_7NO) (Sigma Aldrich) to obtain a 0.75 M solution. The molar ratio of MEA to Zn was kept at 1.0. The resulting mixture was stirred at 50°C for 1 hour then was left to age at room temperature for one week.
Silver nanoparticles were prepared following the procedure reported by Chen et al. (11) . Silver nitrate $AgNO_3$ was dissolved in absolute ethanol to get 0.1M solution and stabilized with different PVP (Poly(N-vinylpyrrolidone)) concentrations, 0.1 M, 0.2 M, 0.3 M and 0.4 M. The obtained mixture was stirred at 30 °C and then 10 mL of ethanol solution of PVP was added drop by drop to the silver solution. When all the amount of PVP was added, the reaction mixture was continued with heating at 60 °C for another 45 min and aged for one week.

The glass substrates were cleaned ultrasonically in ethanol and acetone for 15 min and rinsed with deionized water and finally dried at 100°C for 30 min. A KSV dip-coater apparatus with a withdrawal speed of 1.5 cm/min was employed for the deposition of the Ag-ZnO nanocomposites thin films by using simple two-steps technique. One layer of ZnO was deposited on glass substrate and dried at 350 °C for 15min, followed by deposition of four layers of Ag NPs each one was dried at 150 °C for 15 min. This process was repeated five times. Finally, the films were annealed at 500 °C for 1h.
All samples were characterized using X-ray diffraction (XRD). XRD patterns were collected on a Rigaku Mini flex-II diffractometer using the Cu-Kα radiation (λkα1 = 1.5406 Å) and a scan step of 0.02° (2θ). The optical transmittance spectra were recorded by a Safas UVmc^2 UV-Vis-NIR spectrophotometer. The photoluminescence properties were measured at room temperature using a SHIMADZU RF-6000 spectrofluorophotometer.

Results and discussion

Absorption of colloidal Ag nanoparticles

Fig. 1 shows the UV-Vis spectra of four $AgNO_3$ with different PVP amount reduced in the ethanol media. All the samples exhibit a sharp and strong absorption band at 423-436nm, which is the characteristic absorption band of Ag nanoparticles (12). The absorption maximum is red shifted when the PVP ratio is increased indicating the increase of the average size of the Ag nanoparticles.

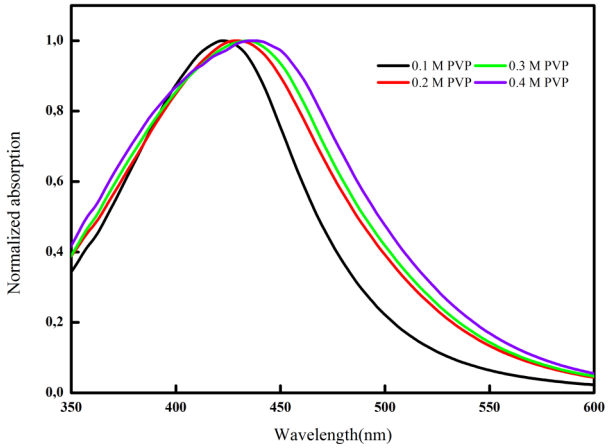

Fig. 3: Normalized absorption spectra of Ag nanoparticles synthesized at different PVP concentrations.

Structural characterization.

Fig. 2 shows XRD patterns of ZnO-Ag nanocomposites thin films at various concentrations of PVP. The results shows that all the obtained ZnO-Ag films have a preferential (002) peak (34.5°) of the ZnO hexagonal wurtzite crystalline phase in addition to (111) diffraction peak at (38.2°) corresponding to cubic Ag structure. As the PVP concentration increased from 0.1M to 0.4M, the intensity of the ZnO (002) diffraction peak increased as better shown in the insert of Fig. 2 indicating the improvement of the crystal quality.

The crystallite size D can be calculated from the FWHM of the ZnO (002) using the Debye-Scherer formula (13):

$$D = \frac{0{,}9\ \lambda}{\beta \cos\theta}$$

Where λ is the wavelength of the X-ray radiation, β is the FWHM in radians, and θ is the Bragg diffraction angle. The average diameter of ZnO crystallites increase from 25.1 nm to a maximum value of 28.8 nm when PVP concentration is increased from 0.1 to 0.4M.

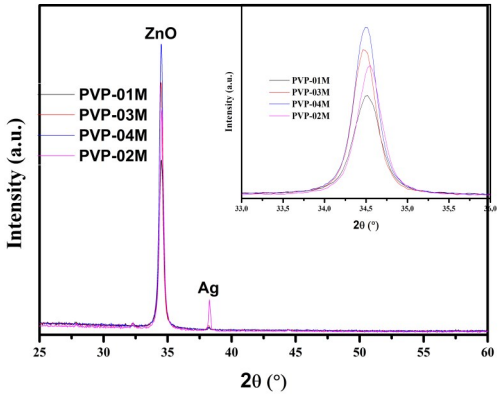

Fig. 2. X-ray diffraction pattern of ZnO-Ag nancomposites thin films at various PVP concentrations. The inset shows evolution of the (002) peak.

Optical Transmittance

Fig. 3 shows the optical transmission spectra of the ZnO-Ag nanocomposites thin films at different PVP concentrations. The films exhibit a high average transmittance in the visible wavelengths. The greater value of transmittance is about 90.6 % at 650nm corresponding to 0.3M of PVP. Beyond this concentration, the transmittance decrease slightly to 88 %.

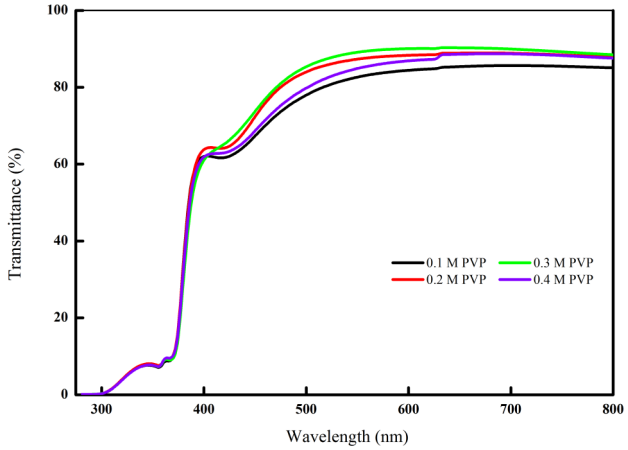

Fig. 3. Optical transmittance spectra of ZnO-Ag nanocomposites thin-films deposited at various PVP concentrations.

Photoluminescence

The room temperature PL spectra obtained at an excitation wavelength of 350 nm of Ag-ZnO nanocomposites thin films are shown in Fig. 4. PL emission spectra of all the samples consist on a UV luminescence band centered at 389 nm, a violet shoulder and a very weak visible emission. As can be seen, the intensity of the UV emission which is due to the near-band-edge (NBE) emission (14) increases with increasing PVP ratio. This result may be related to the improvement of the crystal quality as shown in XRD section. However the defect related visible emission increases when PVP ratio is increased from 0.1 M to 0.2 M and then decrease for higher concentrations. The same behavior is observed for the violet emission. This latter emission is due to the electronic transition from the bottom of the conduction band to the zinc interstitials (Zn_i) level (15).

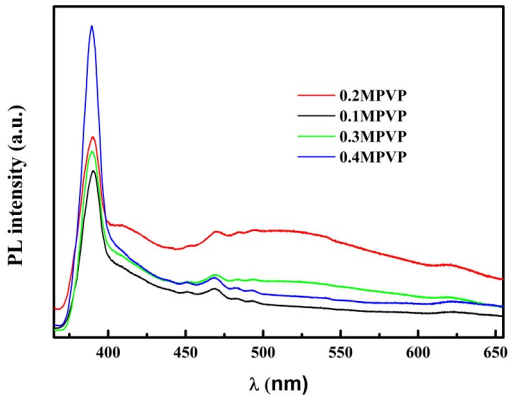

Fig. 4. Room temperature photoluminescence spectra of ZnO-Ag nanocomposites thin films deposited at various PVP concentrations.

Conclusion

ZnO-Ag nanocomposites thin films were deposited onto glass substrates using dip-coating process. The sol gel process has been used to prepare ZnO film and the plyol protocol was employed to prepare Ag nanoparticles at different concentrations of PVP. The Optical absorption spectra in the UV-visible range demonstrated an absorption peak characteristic of the Ag nanoparticles which is red shifted when the concentration of PVP is increased. XRD analysis indicated that all the films are crystallized in a ZnO hexagonal wurtzite structure and are highly c-axis oriented in addition to the presence of a cubic Ag phase. The increase in PVP ratio leads to the improvement of crystal quality and the increase in the average crystallite. UV–Vis–NIR transmittance spectra indicated that the transparency the samples increase with increasing PVP content. Room temperature PL results put into evidence that the emission of all the films is dominated by a UV emissions at 389 nm which is found to increase with increasing PVP concentration.

References

1. S. Koppala, Y. Xia, L. Zhang, J. Peng, Z. Chen, L. Xu. Hierarchical ZnO/Ag nanocomposites for plasmon-enhanced visible-light photocatalytic performance. *Ceram. Inter.* doi: https://doi.org/10.1016/j.ceramint.2019.04.252 (2019).
2. S. Singh, R. Singhal. Thermal-induced SPR tuning of Ag-ZnO nanocomposite thin film for plasmonic applications. *Appl. Surf. Sci*., **439**, 919-926 (2018).
3. S. A. Ansari, M. M. Khan, M.O. Ansari, J. Lee, M. H. Cho. Biogenic synthesis, photocatalytic, and photoelectrochemical performance of Ag–ZnO nanocomposite. *J. Phys. Chem. C*. **117(51),**27023-27030 (2013).
4. L. Sun, R. Shao, L.Q. Tang, Z. D. Chen. Synthesis of Ag/ZnO Nanocomposite with Excellent Photocatalytic Performance via a Facile Sol-Gel Method. *Adv. Mater. Res.**875-877***, 251-256 (2014).
5. S. K. Sharma, G.S. Ghodake, D. Y. Kim, D-Y. Kim, O. Thakur. Synthesis and characterization of hybrid Ag-ZnO nanocomposite for the application of sensor selectivity. *Curr. Appl. Phys.***18(4)**,377-383 (2018).
6. Ü. Özgür, Y. I. Alivov, C. Liu, A. Teke, M. Reshchikov, S. Doğan, et al. A comprehensive review of ZnO materials and devices. *J. Appl. Phys.***98(4)**, 11(2005).
7. S. Agnihotri, S. Mukherji, S. Mukherji. Size-controlled silver nanoparticles synthesized over the range 5–100 nm using the same protocol and their antibacterial efficacy. *RSC Advances*.;**4(8),**3974-83 (2014).
8. N. Venugopal, A. Mitra. Plasmonics properties of ZnO/Ag/ZnO multilayer thin films. *Adv. Mater. Res.* **585** , 214-218 (2012).
9. A. Chelouche, T. Touam, M. Tazerout, F. Boudjouan, D. Djouadi, A. Doghmane. Low cerium doping investigation on structural and photoluminescence properties of sol-gel ZnO thin films. *J. Lumin.*.;**181**, 448-454(2017).
10. A. Chelouche, T. Touam, F. Boudjouan, D. Djouadi, R. Mahiou, A. Bouloufa, G. Chadeyron, Z. Hadjoub. Na doping effects on the structural, conduction type and optical properties of sol–gel ZnO thin films. *J. Mater. Sci.: Mater. Electron*.**28(2)**,1546-1554 (2017)

11. D. Chen, X. Qiao, X. Qiu, J. Chen. Synthesis and electrical properties of uniform silver nanoparticles for electronic applications. *J. Mater. Sci*. **44(4)**,1076-1081 (2009).
12. M. H. Habibi, R. Sheibani. Preparation and characterization of nanocomposite ZnO–Ag thin film containing nano-sized Ag particles: influence of preheating, annealing temperature and silver content on characteristics. *J. sol-gel Sci. technol*.**54(2),**195-202 (2010).
13. J. I. Langford, A. Wilson. Scherrer after sixty years: a survey and some new results in the determination of crystallite size. *J. Appl. Crystallo.***11(2)**,102-13 (1978).
14. M. M. H. Farooqi, R. K. Srivastava. Enhanced UV–vis photoconductivity and photoluminescence by doping of samarium in ZnO nanostructures synthesized by solid state reaction method. *Optik;***127(8)**, 3991-3998 (2016).
15. K. D. A. Kumar, S. Valanarasu, A. Kathalingam, V. Ganesh, M. Shkir, S. AlFaify. Effect of solvents on sol–gel spin-coated nanostructured Al-doped ZnO thin films: a film for key optoelectronic applications. *Appl. Phys. A*.**123(12)**, 801 (2017).

Photoresponsivity Enhancement of Thin-Film Photodiodes Decorated with Au Nanoparticles

Authors: Mohamed Sbeta[1,2] and Abdullah Yildiz[1,*]

Affiliations:

[1]Department of Energy Systems Engineering, Faculty of Engineering and Natural Sciences, Ankara YıldırımBeyazıt University, Ankara,Turkey

[2]Center for Solar Energy Research and Studies, Tripoli, Libya

*Corresponding author: yildizab@gmail.com

One Sentence Summary: Photoresponsivity of ZnO *p-n* heterojunction photodiodes is significantly improved after decoration of their surface with Au NPs.

Abstract: Thin-film photodiodes based on sol-gel processed ZnO thin films decorated by Au nanoparticles (Au NPs) exhibit remarkable improvements in photoelectric properties. After decoration of their surface with Au NPs, the dark current of the fabricated *p-n* heterojunction photodiodes obviously decreases and rectification ratio increases. Moreover, an excellent photoresponsivity of 0.2 A/W beyond that of the value (0.06 A/W) of photodiodes obtained without NPs is observed. Our results verify that the decoration of NPs in not only photodiodes but also other optoelectronic devices such as solar cells and sensors can be considered with enhanced functionality.

Introduction

ZnO is a well-known wide bandgap (~3.27 eV) [1] semiconductor material received widespread attention for the fabrication of deep-ultraviolet (UV) photodetectors [2]. Schottky and *p-n* junction photodiodes (PDs) based on ZnO have been previously reported [3-5]. On the other hand, a disadvantage of Schottky PDs is that they exhibit relatively high reverse leakage current compared *p-n* junction counterpart. The *p-n* heterojunction PDs are promising for various optoelectronic applications. A possible method for fabricating ZnO *p-n* heterojunction devices is to establish a junction between ZnO and a *p*-type semiconductor in which Si is generally preferred.

To boost PD performance, there are many ways. However, surface plasmon resonance (SPR) is a method superior over others in many aspects [6]. Decoration of metal nanoparticles (NPs) such as Ag, Au, and Al on ZnO can enhance ability of absorption and scattering of incident light onto the surface leading an improved the near-band-edge emission. Once frequency of the incident light matches with resonance frequency of surface plasmons, electromagnetic field near metal surface is improved which causes higher photoresponsivity in PDs. Plasmon resonance depends on size, shape and distribution of NPs.

In this study, we report on ZnO:Ga/p-Si *p-n* heterojunction PDs fabricated by using the sol-gel spin coating method. After decoration of their surface with Au NPs, a performance enhancement of the devices is observed under UV light illumination.

Results

Figure 1 depicts the schematic illustration of the investigated devices. Fig. 2 shows the *I-V* curve of the devices with and without Au NPs under dark and light condition exhibiting excellent rectifying characteristics. The dark current of the device is estimated to be 30 and 64 nA for the device with and without Au NPs, respectively. Rectification ratio is 12500 and 8800 at ±3V for the device with and without Au NPs, respectively. It is obvious that the photocurrent of the device with Au NPs is remarkably enhanced compared to the photocurrent of device without Au NPs.

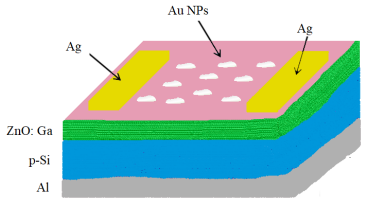

Fig. 1. A schematic diagram of *p-n* heterojunction device structure with Au NPs.

Discussion

The fabricated devices are consisting of n-ZnO:Ga/p-Si *p-n* heterojunction PDs with and without Au NPs deposited on ZnO surface. Since it is relatively thin (~80 nm), the ZnO:Ga layer is expected to be fully depleted under reverse bias. The photogenerated carriers in the layer mainly contribute to the photocurrent. Therefore, we focus on this layer. The results above demonstrate that the incorporation of Au NPs onto this layer boosts the performance parameters of the device.

It is evident that a considerable enhancement in the photocurrent is obtained in the device with Au NPs compared to the device without Au NPs, which should be associated with surface plasmon resonance. Au NPs tune the optical and electrical properties of the device. After incorporation of Au NPs, the enhancement in the incident light absorption, scattering, carrier transport, and electrical conductivity can be expected [6]. Finally, the enhancement in one or more results in an increased photoresponsivity of PDs. The device without Au NPs demonstrates photoresponsivity of 0.06A/W at a low reverse bias voltage (-3V) while the device with Au NPs exhibits an excellent photoresponsivity of 0.2 A/W at the same bias voltage.

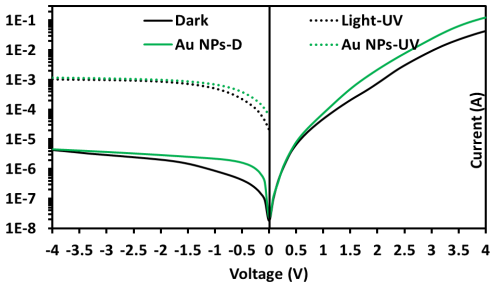

Fig. 2. *I-V* characteristics of the devices in dark and under UV illumination conditions.

Materials and Methods

The ZnO:Ga/*p*-Si heterojunction PDs is formed by the deposition of sol-gel derived ZnO:Ga thin film on *p*-Si substrate and solution processed Au NPs are spin coated on the top of ZnO:Ga before metallization. The deposition details and information about characterizations are given in somewhere else [3].

References and Notes:

1. T Serin, A Yildiz, Ş Uzun, E Çam, N Serin, Electrical conduction properties of In-doped ZnO thin films Physica Scripta **84,** 065703 (2011).
2. Feng Yang et al.,The high-speed ultraviolet photodetector of ZnO nanowire Schottky barrier based on the triboelectric-nanogenerator-powered surface-ionic-gate, Nano Energy **60,** 680 (2019).
3. M. Sbeta and A. Yildiz, Optical response enhancement of GZO/p-S heterostructures via metal nanoparticles, *Materials Research Express* **6,** 085018 (2019).
4. N. E. Koksal, M. Sbeta, A. Yildiz , GZO/Si photodiodes exhibiting high photo-current to dark-current ratio, IEEE Transactions on Electron Devices, **66,** 2238 (2019).
5. A. Yildiz, S. Uzun, N. Serin, T. Serin, Influence of grain boundaries on the figure of merit of undoped, Al, In, and Sn doped ZnO thin films for photovoltaic applications, Scripta Materialia **113,** 23 (2016).
6. Yoon Hee Jang et al., Plasmonic Solar Cells: From Rational Design to Mechanism Overview Chem. Rev. **116,** 14982 (2016).

Acknowledgments: This work is supported by BAP of the Ankara Yıldırım Beyazıt University (under Project Number 5037).

Fabrication of Compact Carbon Electrode for Carbon-based Perovskite Solar Cells

Authors: Cesur Altinkaya[1]*, Abdullah Atilgan[1], Kouroush Salimi[2], Abdullah Yildiz[1]

Affiliations:

[1]Department of Energy Systems Engineering, Faculty of Engineering and Natural Sciences, Ankara Yıldırım Beyazıt University, Ankara, Turkey.

[2]Department of Chemical Engineering, Faculty of Engineering and Natural Sciences, Ankara Yıldırım Beyazıt University, Ankara, Turkey

*Corresponding author: cesuraltnky@gmail.com

One Sentence Summary: A novel low-temperature and low-cost carbon electrode was fabricated in this study.

Abstract: Organic-inorganic perovskite solar cells have attracted great attention from the research community due to the significant increase in their power conversion efficiencies exceeding 23% over the last decade. Despite such high efficiencies, long-term stability, high cost and up-scaling still remained unsolved problems. Organic hole transport layers (Spiro-OMeTAD etc.) and Au counter electrodes which are commonly used in the field limits the stability and commercialization of PSCs. Recently, hole-transporter free carbon based PSCs showed the most promising potential for commercialization with the advantages of low-cost, high stability and easy fabrication. Herein, we aim to produce a novel type of carbon electrode with high stability and electrical conductivity by simplifying the fabrication procedure of carbon paste. A simple preparation method of carbon paste including the only ultra- and probe- sonication methods were used and low-temperature processed carbon counter electrode was produced. SEM measurements and four probe analysis demonstrated that produced carbon electrode has compact nature with low sheet resistance /high electrical conductivity. Additionally, device production steps were conducted under fully ambient environment to avoid the harsh fabrication conditions used in traditional PSCs. Finally, we produced low cost and easy to fabricate PSCs with a novel kind of carbon electrode.

Introduction

Since as early as 2009, hybrid organic-inorganic metal halide perovskite solar cells (PSCs) have attracted considerable attention of many researchers due to their high extinction coefficient, excellent ambipolar charge carrier mobility, high absorption coefficients, small exciton binding energies, long carrier diffusion lengths and optimal/tunable bandgaps (1-3). Traditional PSCs are generally in the structure of Glass/FTO/Compact Layer (CL)/Electron Transport Layer (ETL)/ Perovskite/Hole Transport Layer (HTL)/Counter Electrode (CE) as will be shown in the following section. To date, Spiro-OMeTAD and Au/Ag are the most commonly used materials as HTL and CE, respectively (*4*). The high power conversion efficiencies exceeding 23% were achieved by employing these materials. However, the stability and degradation issues remain unsolved until now. Spiro-OMeTAD has a low conductivity arising from poor hole mobility. That is why it is required to doped with additives such as Lithium salts (Li-TFSI) and 4-tertbutyl pyridine (tBP) to increase the mobility and conductivity. However, the use of additives causes the degradation of perovskite layer due to following reasons: 1) perovskite is highly water sensitive and Li-TFSI absorbed moisture in the air, and then leads to degradation of perovskite layer; 2) during the storage of device, tBP evaporates slowly and therefore Li salts aggregation with penetration of moisture occurs that induces to directly degradation of perovskite. Also, Spiro-OMeTAD becomes penetrable at elevated temperatures causing to the diffusion of metal electrodes across the HTL, and both Ag and Au chemically etches perovskite and causes drastically the loss of device performance. On the other hand, even though there have been intensive efforts to investigate novel HTLs apart from Spiro-OMeTAD, any promising alternatives exhibiting good stability outputs to commercialize PSCs have not yet been found. Moreover, the high cost of both Spiro-OMeTAD and Au, as well as high energy consumption for deposition of CEs are other critical obstacles to commercialize traditional PSCs (*5-8*). In this regard, some methods have been proposed including hybridization of perovskite and/or halide derivatives

(i.e., $CsMAFAPbI_3$, $MAPb(I_xCl_yBr_z)_3$, etc. ; FA: Formamidinium), interface engineering, employing inorganic HTLs (i.e., CuSCN) and etc. However, PSCs with high stability has not yet been realized (*9-11*).

To tackle these issues, carbon-based hole-transporter-free PSCs (hereafter, referred as C-PSCs) have emerged as promising candidates due to their high stability and moderate efficiency (exceeding 15%) to compete with industrially used Si-based solar cells in terms of stability and low-cost. C-PSCs can function efficiently thanks to the ambipolar feature of perovskite which can operate as both light harvester and hole transporter. Furthermore, it was revealed that carbon derivatives can be used as CE thanks to their suitable Fermi level (~ -5 eV), high conductivity/hole mobility, robustness, chemically/thermally stable nature and inherit hydrophobicity. Therefore, carbon electrodes can easily extract holes from perovskite and protect the perovskite layer from the moisture that leads to stable devices at both room and elevated temperatures. Additionally, facile and low-cost preparation (i.e., solution processing) and deposition (i.e., printing, drop casting, spin-coating) methods are other key advantages of carbon-based electrodes over the noble metals. Therefore, C-PSCs have attracted tremendous attention (*12-15*).

In this study, we report a low temperature and low-cost preparation method of carbon counter electrode with high stability and electrical conductivity for C-PSCs applications.

Results

SEM images

Figure 1 shows SEM images of carbon films coated on FTO substrates by drop casting method and annealed at 100 °C. In Fig. 1a, graphite flakes in the film are clearly seen. Furthermore, Also, carbon nanotubes (CNTs) are demonstrated in Fig. 1b. Here, the aim of using graphite flakes is to provide electrical conductivity which means that holes produced in perovskite absorber layer upon light excitation in the device mainly transferred from graphite flakes. Moreover, CNTs enable a direct pathway for hole extraction from perovskite to contacts and thus improve the conductivity. As of carbon black, they fill the voids that can be occurred at the interface between perovskite and carbon CE due to big-size graphite flakes. Thereby, continuous contact between perovskite and CE can be ensured and device performance is improved (*16*). Cross-sectional SEM images are shown in Fig 1c and d. As seen here, it is explicitly demonstrated that carbon film has a very compact nature which facilitates the hole transfer through the film. In the literature, reported carbon electrodes showed a porous nature with abundant voids. To the best of our knowledge, fabricated carbon paste demonstrated a highly compact structure compared to counterparts in the literature (*17-19*). Moreover, the thickness of the film was found around 20 µm which is well suitable for efficient hole transport distance (*16*).

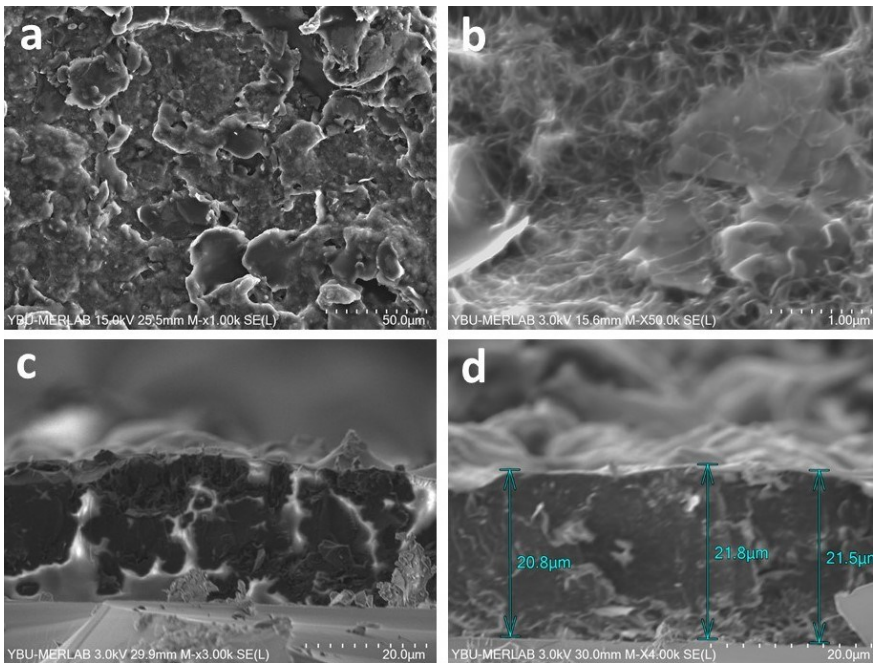

Fig.1. SEM images of carbon films coated on FTO substrates: (a), (b) surface images and (c), (d) cross-sectional images of films

Sheet Resistance

The sheet resistance of carbon films coated on FTO/Glass was measured by employing a Four Probe analyzer and were evaluated according to R_s=V/I×4.5324 equation (*20*). The average sheet resistance was found as 25 Ω/□ for carbon films. This sheet resistance value proves the high electrical conductivity of our carbon films.

J-V Results

The fabricated devices have the structure of FTO/c-TiO_2/mp-TiO_2/Perovskite/Carbon as demonstrated in Fig. 2a. $CsFAPbI_3$ was chosen as a perovskite absorber layer and fabricated under ambient conditions (RH: 70 %) as reported elsewhere (21). Fig. 2b shows the J-V characteristic of the champion device The open-circuit voltage (V_{OC}), short circuit current density (J_{SC}), fill factor (FF), and power conversion efficiency (PCE) of the devices are listed in the inset of the figure. The champion device exhibited a J_{SC} of 6.85 mA/cm^2, V_{OC} of 0.56 V, FF of 37 % and PCE of 1.4 %. Although the PCE found in the study is quite low compared to recent efficiencies in the literature, it can be concluded that our new kind of low-temperature carbon electrode operates well in C-PSCs. On the other hand, optimization of device structure and individual layers is still ongoing issues for our study.

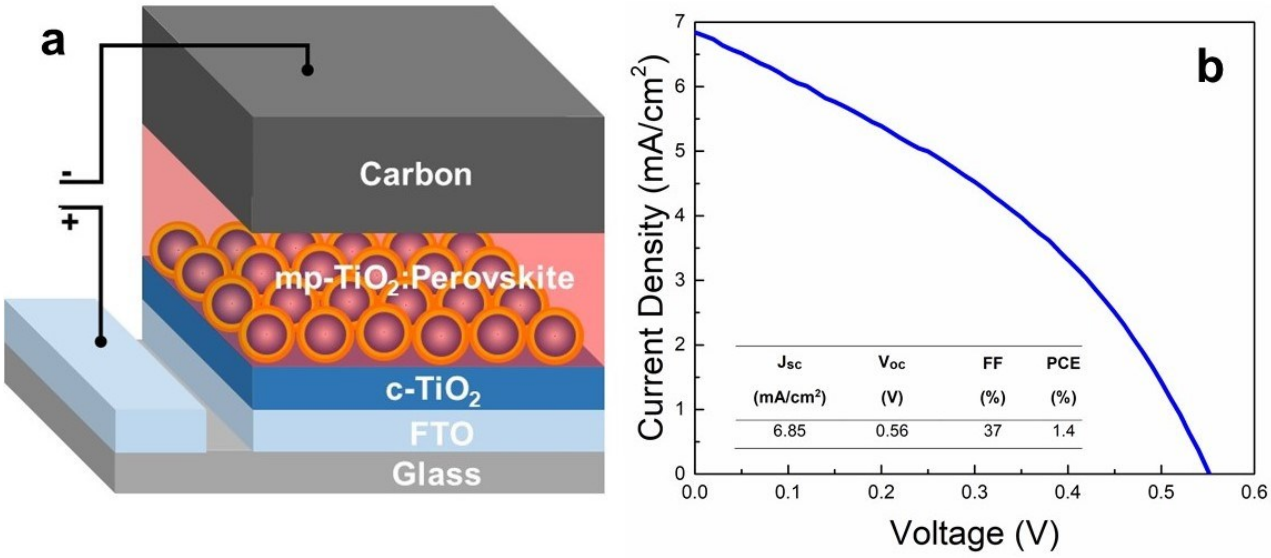

Figure 2: (a) The schematic diagram of fabricated devices, (b) photocurrent density versus voltage (*J-V*) curve of the champion device.

Discussion

In summary, we demonstrated a facile, low-temperature preparation method for carbon electrode with high electrical conductivity for C-PSCs. Despite the low efficiencies exhibited by our C-PSCs, operation of devices shows that this novel carbon electrode can be used in C-PSCs especially to produce flexible devices and thus may pave the way for the commercialization of PSCs.

Materials and Methods

Materials

All reagents and solvents were used without further purification. PbI_2 (99,99%), FAI (99,99%), DMSO (≥99.9%), DMF (99,5%), 2-Propanol (99,5%) were purchased from Sigma Aldrich. CsI (99.0%) and Chlorobenzene (98%) were acquired from TCI. Graphite, carbon black and carbon nanotubes were bought from Nanografi Co.

Preparation of Carbon Paste

Different amount of graphite, carbon black and carbon nanotubes were mixed in chlorobenzene. The mixture of carbon derivatives was ultra- and probe-sonicated for 30 min, respectively. The sonication procedure can be repeated until obtaining a fully viscous paste. It is worthy to note that, the carbon paste should be heated to 80 °C on a hot plate with magnetic stirring before deposition to ease the drop-casting process.

Device Fabrication

FTO substrates were etched by using Zn powder and 2M HCl, then ultrasonically cleaned by deionized water, ethanol and acetone for 10 min, respectively. The compact and mesoporous TiO_2 layers were deposited on cleaned FTO substrates as reported in our previous study except that TiO_2 paste was diluted in EtOH to optimize the layer thickness (*22*). A perovskite absorber layer was deposited on mp-TiO_2 under ambient conditions (RH-70%) as reported elsewhere (*21*). Before the deposition of the carbon electrode, the substrates were heated at 80 °C on a hot plate and as-prepared carbon paste was drop casted on them as being 25 µL per cm^2. Subsequently, the devices were heated at 100 ° C for 20 min to dry the carbon electrode.

Characterization

The sheet resistance of carbon films was provided by a LucasLab-302 four-point probe analyzer. The morphology of carbon films was analyzed by a field-emission scanning electron microscope (SEM) (Hitachi SU500 FE-SEM). Photocurrent density-voltage (J-V) characteristics of the devices were measured with a Keithley 2400 source meter under the air mass 1.5 (AM 1.5) illumination (Abet LS 150, Abet Technologies, Inc., USA). The power of the simulated light was calibrated to 100 $mWcm^{-2}$ by a SRC-2020 solar reference cell. The active area of devices was 0.20 cm^2.

References and Notes:

1. Kojima A, Teshima K, Shirai Y, Miyasaka T. Organometal halide perovskites as visible-light sensitizers for photovoltaic cells. Journal of the American Chemical Society. 2009;131(17):6050-1.
2. Saliba M, Correa□Baena JP, Grätzel M, Hagfeldt A, Abate A. Perovskite solar cells: From the atomic level to film quality and device performance. Angewandte Chemie International Edition. 2018;57(10):2554-69.
3. Zhang Y, Liu M, Eperon GE, Leijtens TC, McMeekin D, Saliba M, et al. Charge selective contacts, mobile ions and anomalous hysteresis in organic–inorganic perovskite solar cells. Materials Horizons. 2015;2(3):315-22.
4. Pedesseau L, Sapori D, Traore B, Robles R, Fang HH, Loi MA, et al. Advances and Promises of Layered Halide Hybrid Perovskite Semiconductors. Acs Nano. 2016;10(11):9776-86.
5. Zhou T, Lai H, Liu T, Lu D, Wan X, Zhang X, et al. Highly Efficient and Stable Solar Cells Based on Crystalline Oriented 2D/3D Hybrid Perovskite. Advanced Materials. 2019:1901242.
6. Wei Z, Yan K, Chen H, Yi Y, Zhang T, Long X, et al. Cost-efficient clamping solar cells using candle soot for hole extraction from ambipolar perovskites. Energy & Environmental Science. 2014;7(10):3326-33.
7. Yan K, Wei Z, Li J, Chen H, Yi Y, Zheng X, et al. High-performance graphene-based hole conductor-free perovskite solar cells: Schottky junction enhanced hole extraction and electron blocking. Small. 2015;11(19):2269-74.
8. Rong YG, Hou XM, Hu Y, Mei AY, Liu LF, Wang P, et al. Synergy of ammonium chloride and moisture on perovskite crystallization for efficient printable mesoscopic solar cells. Nat Commun. 2017;8.
9. Grancini G, Nazeeruddin MK. Dimensional tailoring of hybrid perovskites for photovoltaics. Nat Rev Mater. 2018:1.
10. Marinova N, Valero S, Delgado JL. Organic and perovskite solar cells: Working principles, materials and interfaces. J Colloid Interface Sci. 2017;488:373-89.
11. Gualdrón-Reyes AF, Yoon SJ, Mora-Seró I. Recent Insights for Achieving Mixed Halide Perovskites without Halide Segregation. Current Opinion in Electrochemistry. 2018.
12. Domanski K, Correa-Baena JP, Mine N, Nazeeruddin MK, Abate A, Saliba M, et al. Not All That Glitters Is Gold: Metal-Migration-Induced Degradation in Perovskite Solar Cells. Acs Nano. 2016;10(6):6306-14.
13. Chan C-Y, Wang Y, Wu G-W, Diau EW-G. Solvent-extraction crystal growth for highly efficient carbon-based mesoscopic perovskite solar cells free of hole conductors. Journal of Materials Chemistry A. 2016;4(10):3872-8.

14. Liu T, Liu L, Hu M, Yang Y, Zhang L, Mei A, et al. Critical parameters in TiO2/ZrO2/Carbon-based mesoscopic perovskite solar cell. Journal of Power Sources. 2015;293:533-8.
15. Mei A, Li X, Liu L, Ku Z, Liu T, Rong Y, et al. A hole-conductor–free, fully printable mesoscopic perovskite solar cell with high stability. Science. 2014;345(6194):295-8.
16. Wei Z, Chen H, Yan K, Zheng X, Yang S. Hysteresis-free multi-walled carbon nanotube-based perovskite solar cells with a high fill factor. Journal of Materials Chemistry A. 2015;3(48):24226-31.
17. Peiris TAN, Baranwal AK, Kanda H, Fukumoto S, Kanaya S, Cojocaru L, et al. Enhancement of the hole conducting effect of NiO by a N-2 blow drying method in printable perovskite solar cells with low-temperature carbon as the counter electrode. Nanoscale. 2017;9(17):5475-82.
18. Li F, Xu Y, Chen W, Xie S, Li J. Nanotube enhanced carbon grids as top electrodes for fully printable mesoscopic semitransparent perovskite solar cells. Journal of Materials Chemistry A. 2017;5(21):10374-9.
19. Liu Z, Sun B, Liu X, Han J, Ye H, Tu Y, et al. 15% efficient carbon based planar-heterojunction perovskite solar cells using a TiO 2/SnO 2 bilayer as the electron transport layer. Journal of Materials Chemistry A. 2018;6 (17):7409-19.
20. Sbeta M, Atilgan A, Atli A, Yildiz A. Influence of the spin acceleration time on the properties of ZnO: Ga thin films deposited by sol–gel method. Journal of Sol-Gel Science and Technology. 2018;86(2):513-20.
21. Xu X, Ma C, Xie Y-M, Cheng Y, Tian Y, Li M, et al. Air-processed mixed-cation Cs 0.15 FA 0.85 PbI 3 planar perovskite solar cells derived from a PbI 2–CsI–FAI intermediate complex. Journal of Materials Chemistry A. 2018;6(17):7731-40.
22. Atli A, Atilgan A, Yildiz A. Multi-layered TiO2 photoanodes from different precursors of nanocrystals for dye-sensitized solar cells. Solar Energy. 2018;173:752-8.

Acknowledgments: This work is financially supported by the Scientific and Technical Research Council of Turkey (TUBITAK, Grant No. 119M076) and Ankara Yıldırım Beyazıt University Scientific Research Projects with a grant number of 4737 and 5486.

Modelling and Simulation of the Carbon Nanotubes FETs.

Authors: F. Kebaili[1*], O. El Mansouri[1], S. Bouchekouf[2]

Affiliations:
[1] *Electronic department, Faculty of Technology, University of M'Sila, M'Sila. Algeria*

[2] *Electronic department. University of Constantine1, Constantine. Algeria*
[1,2,3] *Lab: Modélisation Des Dispositifs A Energie Renouvelable et Nanométrique, Faculty of engineer Science , Mentouri University ,Constantine1. Algeria*

*Corresponding author: *farida.kebailii@univ-msila.dz*

One Sentence Summary: a physical model for Carbon Nanotube FET has been elaborated to determine the charge density, calculate subsequently the resistance of the Carbon nanotubes, and the drain current of CNTFET . The results are discussed and presented.

Abstract: The development or improvement of new channels of field effect transistor can't be considered without the support of physical modeling that allows the predetermination of characteristics and structural optimization. Therefore we were interested in the sum of our study to the modeling of field effect transistor especially CNTFETs.
In this work, we present the different steps of implementation of the equations of our model based on solving one dimensional and two dimensional using Fermi Dirac approximation, to determine the charge density and thus the resistance of the carbon nanotubes, and we deduce the drain current of CNTFET.
A simulation of a coaxially Gated CNTFET is Carried out based on the expressions of the equations provided previously. The results obtained are presented, interpreted and compared by those obtained by Monte Carlo simulation.

Introduction

Carbon nanotubes (CNT) are remarkable synthetic materials with fascinating properties (1,2), such as high mechanical strength, high surface area(3), excellent electronic and chemical properties, and thermal stability. CNTs are nanometer diameter cylinders consisting of single or multiple grapheme sheets wrapped up to form a single wall (SWNT) or multiwall(MWNT) carbon nanotube(4,5), respectively. Carbon nanotube(CNT) appears as a promising candidate to shrink field effect transistors(FET) to the nanometer scale(6-,8). Extensive experimental works have been performed recently to develop the appropriate technology and to explore the characteristics of Carbon nanotube field effect transistor (CNTFET)(9).

In this study, an accurate physical model is presented for calculating the resistance of carbon nanotube, and then we deduce the drain current of CNTFET. The results and discussions are presented.

Transport modeling

Subhead 1: linear density of charge
Using Fermi Dirac statistics we found the density of charge

$$\rho_{CNT} \cong \frac{2q}{h} m v_F \qquad (1)$$

v_F the maximum speed of the carriers.

Subhead 2: Resistance of the CNT

So the resistance of the nanotube per unit length is

$$R_{CNT} = \frac{h}{2q^2}\frac{1}{\tau v_F} = \frac{\pi\hbar\vartheta_{col}}{4q^2 v_F} \quad , \tau = \frac{1}{\vartheta} \tag{2}$$

Subhead 3: current

The total current is

$$I = \frac{2qMk_BT}{h}\sum_{i=1}^{\infty}\left[ln\left(1+exp\frac{\mu_S - E_i + V_{CNT}}{k_BT}\right) - ln\left(1+exp\frac{\mu_D - E_i + V_{CNT}}{k_BT}\right)\right] \tag{3}$$

The relationship between the difference of potential and the load capacity of gate oxide:

$$V_{CNT} = V_{GS} - \frac{Q_{CNT}}{C_{OX}} \tag{4}$$

where

C_{OX} : the Gate capacitance (9)

$$C_{OX} = \frac{2\pi\varepsilon_0\varepsilon_r L}{ln[2(t_{ins}+r)/r]} \tag{5}$$

Q_{CNT} : the charge in the nanotube, wich depends on the carrier density

$$Q_{CNT} = q\rho_{CNT}L \tag{6}$$

L : the gate length

ρ_{CNT} : total density of charge in the nanotube given by the equation (1)

Results and Discussion

(Fig. III.1) shows the carachteristic I_D as a function of $V_{DS,}$ parametrized by V_{GS} . We observe two regions, the first one is explained by the fact that the increase in V_{DS} implies the increases of barrier potential for drain side by electron states +k. The contribution of the current created by electron –k decreases, there by generating an increase in the total current while V_{GS} is constant. the second one, said saturation, when the voltage V_{DS} is greater than $V_{D\,sat}$.

The saturation regime is observed, for example, $V_{GS} = 0.3V \text{ and } V_{DS} > 0.15V$ on the one hand and for $V_{GS} = 0.9V \text{ and } V_{DS} > 0.5V,$ on the other hand. First we discuss the saturation for low V_{GS} , where we can consider that the drain current is constant, then we explain the increase of the current I_D with V_{DS} observed for V_{GS} more important.

When the voltage V_{DS} is large enough (greater than V_{DSsat}), the electrons in the drain must then cross a barrier too high to pass. An increase in V_{DS} does not change this. The current remains constant assuming that V_{CNT} constant.

For a given increases of V_{DS} , the Fermi level of the drain μ_D decreases more than the bottom of the $i^{iéme}$ sub band. The potential barrier to the electrons from the drain is larger; the current generated by the electron states +k decreases again. The total current, which is the difference between the current generated by the electron state +k and that generated by the electron states -k, therefore increases with V_{DS} . Of course, this phenomenon is present for low V_{GS} but it is less marked.

(Fig. III.2) shows that the current increases with the increase of V_{gs} . more V_{gs} increases, the energy level of all sub band is decreased. There is then more carriers in the conduction band and hence the current increases.

V_{DS} is zero: the contribution to the total current of electrons from the source on the hand, and that of the electrons from the drain of the other part are identical.

V_{DS} is positive: both contributions are unbalanced, the electron from the drain is decreased, the difference of the contributions(the total current) is then positive.

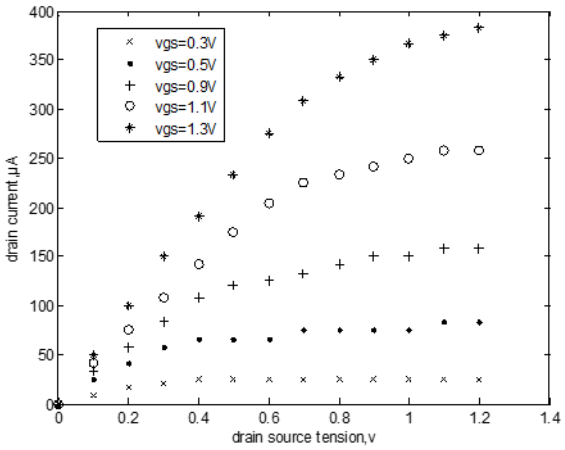

Figure. III.1 :variation of the drain current with V_{DS} according to different value of V_{GS}

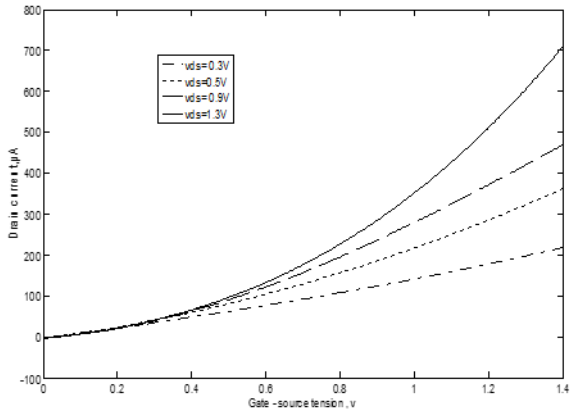

Figure .III.2 : variation of the drain current with V_{GS} according to different value of V_{DS}

(Fig. III. 3), shows the carachteristic $I_D(V_{DS})$ of a transistor based on carbon nanotube with cylindrical grid obtained by the Monte Carlo method [14]. we can say that there is an overall good agreement between the results of our model and those obtained by Monte Carlo simulation.

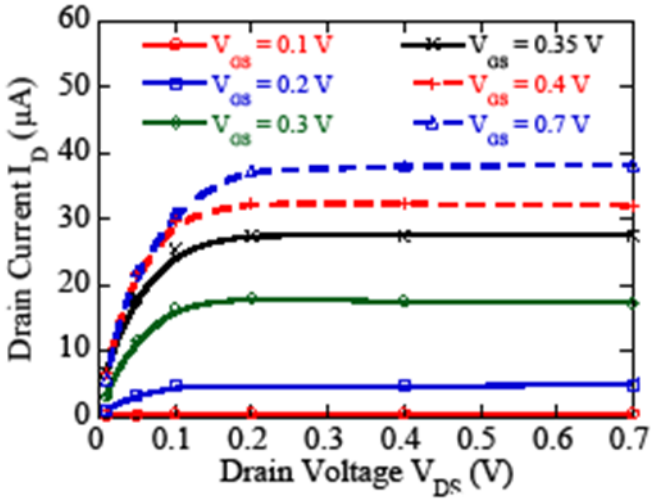

Figure. III.3: variation of the drain current with V_{DS} according to different value of V_{GS}, by Monte Carlo method (9)

References:

1. Jie. Deng , Wong HSP., A compact SPICE model for carbon-nanotube field-effect transistors including no idealities and its application—Part II: full device model and circuit performance benchmarking, in Electron Devices, IEEE Journal , vol. 54-12, 3195 – 3205(2007).
2. W.Hoenlein, F. Kreupl, GS. Duesberg, AP. Graham, M. Liebau , R. Seidel , E. Unger., Carbon nanotubes for microelectronics: status and future prospects, Materials Science and Engineering, vol.23–8, 663–669(2008), .
3. K. Niranjan, S. Srivastava, J. Singh, T. Mukesh. , Comparative study: MOSFET and CNTFET and the effect of length modulation, International Journal of Recent Technology and Engineering (IJRTE) ISSN: 2277-3878, vol. 1- 4, 74-78(2012).
4. S. Naagesh Bhat., Design and modeling of different SRAM'S based on CNTFET 32NM technology, International Journal of VLSI design & Communication Systems (VLSICS), vol. 3- 15, 69-83(2012).
5. R.Marani, A.G. Perri ., A compact, semi empirical model of carbon nanotube field effect transistors oriented to simulation software , Current Nanoscience 7, 245-235(2011).
6. RT. Weitz , U. Zchieschang, AF Aliaga, D. Kalblein , M. Burghard, K. Kern , H. Klauk., Highly Reliable Carbon Nanotube Transistors with Paterned Gates and Molecular Gate Dielectric , Nano Letters, vol. 9 – 4, 1335-1340(2009).
7. P. Keshavarzian, M. Mohammad Mirza., Highly Reliable Carbon Nanotube Transistors with Paterned Gates and Molecular Gate Dielectric , International Journal of Soft Computing and Engineering (IJSCE) .ISSN: 2231-2307, vol. 2- 2, 296-300(2012).
8. R.Sahoo, R.R.Mishra., *Simulation of carbonnanotube field effect transistors* , International Journal of Electronic Engineering Reaserch, vol.1-2, 117-125(2009).
9. H.Cazin, S.G.Retailleau, A.Bournel, P.Dollfus, J.P.Bourgoin :''Monte Carlo Study of Coaxially Gated CNTFET's : Capacitive Effects and Dynamic Performance'', App.Phys.Lett.87 (2008).

ORGANIZING COMPANY

ENNA

The European Nanoscience and Nanotechnology Association (ENNA) is the leading professional body for people working in the field of materials, chemistry, biotechnology and physics. ENNA is a non-profit scientific organization founded in 2013 by a group of scientists to promote the creation of knowledge and innovation in an interdisciplinary field like nanoscience and nanotechnology. ENNA include an international community of scientists who seek for the benefit of society, taking into account the expectations of future generations. We encourage the development of young talents and aim to become the largest association of nanoscientists in Europe. The ENNA members are scientists, technologists, teachers, students and individuals who have broad interests in the nanoscience field. ENNA organizes international scientific conferences and provides specialized courses in the field of nanoscience. The ENNA meetings attract internationally recognized researchers who deliver high-quality scientific presentations. As a non-profit organization, ENNA is also involved in various national and European networking projects. All countries and/or regions of materials scientists whose aims are to promote nanoscience and nanotechnology may become a member of the association.

BENEFITS OF MEMBERSHIP

Membership can provide opportunities for networking and professional development. Association members enjoy a wide range of benefits, summarised below.

- Job and event posts in the ENNA website
- Mentoring and training scheme for members seeking professional qualifications
- Free email notifications of news and content updates relevant to your interests
- Priority access and discounted rates for conferences and events
- Access to regular events and meetings hosted by the association

Discounted rates on ENNA student membership - for undergraduates and postgraduates

To join ENNA or to ask any questions please email: **info@europenanoscience.org** or call us on **+359895792567**

Peer-reviewed manuscripts

INTERNATIONAL CONFERENCE ON CHEMICAL PHYSICS AND MATERIALS SCIENCE

8-10 July 2019, Istanbul, Turkey

Contact:
Saim Emin
European Nanoscience and
Nanotechnology Association
Str. G.S. Rakovski 111, Sofia 1000, Bulgaria
www.europenanoscience.org
E-mail: info@europenanoscience.org
Tel: +359 895 792 567

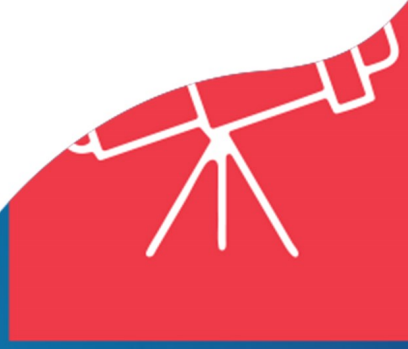

International Conference
on Chemical Physics
and Materials Science

Editors:
Saim Emin
Abdullah Yildiz
Polina Mladenova